

# Objective Measurement of Motion in the Orbit

Michael Abràmoff

Copyright © 2001 by M.D. Abràmovff.

All rights reserved.

Published by Abràmovff Transatlantic Publishing, New York, New York

Printed in the United States of America  
Printing/binding by Signature Book Printing

ISBN 0-9713598-0-6  
Library of Congress Control Number: 2001118500

# Objective Measurement of Motion in the Orbit

OBJECTIEVE METING VAN DE BEWEGING IN DE OOGKAS  
(MET EEN SAMENVATTING IN HET NEDERLANDS)

PROEFSCHRIFT

TER VERKRIJGING VAN DE GRAAD VAN DOCTOR AAN DE UNIVERSITEIT UTRECHT OP  
GEZAG VAN DE RECTOR MAGNIFICUS,  
PROF. DR. W.H. GISPEN, INGEVOLGE HET BESLUIT VAN HET COLLEGE VOOR  
PROMOTIES IN HET OPENBAAR TE VERDEDIGEN OP

DONDERDAG 20 SEPTEMBER 2001 DES OCHTENDS TE 10:30 UUR

DOOR

MICHAEL DAVID ABRÀMOFF

GEBOREN OP 7 MAART 1963 TE ROTTERDAM

Promotores: **Prof. dr. J.S. Stilma**  
Universitair Medisch Centrum Utrecht

**Prof. dr. ir. M.A. Viergever**  
Universitair Medisch Centrum Utrecht

Co-promotor: **Dr. M.Ph. Mourits**  
Universitair Medisch Centrum Utrecht



The research described in this thesis was carried out at the Image Sciences Institute and the F.C. Donders Institute, University Medical Center Utrecht (Utrecht, the Netherlands), under auspices of Imago, the Graduate School for Biomedical Image Science.

Grateful acknowledgment is made of financial support for the research by the following institutions (in chronological order): the *Department of Radiology, Radiotherapy and Nuclear Medicine*, University Medical Center Utrecht, the *Girard de Miolet van Coehoorn Stichting*, Utrecht, the *Department of Ophthalmology*, University Medical Center Utrecht, the *Dr. F.P. Fischer Stichting*, Utrecht (grant XIII-10), and the *Department of Ophthalmology* of the *Vrije Universiteit* Medical Centre, Amsterdam.

Grateful acknowledgment is made of financial support for the publication of this thesis by Philips Medical Systems NV, Tramedico BV, Alcon BV, 3M Nederland BV, Allergan BV, Pharmacia BV, Medical Workshop BV, Lameris BV, Eyecheck BV, Transatlantic Diagnostics BV, and several anonymous sponsors.

*Men's eyes were made to look, and let them gaze;*  
W. Shakespeare. Romeo and Juliet, Act III, scene I, 59. The Oxford Shakespeare, 1914

For Dewi, Yair and Nathan



# Contents

Foreword	9
1	Introduction 11
2	Functional anatomy studies of the orbit 23
3	Fast cine MRI of the orbit 33
4	Objective quantification of the motion of soft tissues in the orbit 43
5	Computation and visualization of three-dimensional soft tissue motion in the orbit 61
6	MRI Dynamic Color Mapping: a new quantitative technique for imaging soft tissue motion in the orbit 79
7	Patients with persistent pain after enucleation studied by MRI Dynamic Color Mapping and histopathology 89
8	Rectus extraocular muscle paths before and after decompression surgery for Graves' orbitopathy: relationship to motility disturbances 99
9	General discussion 119
Bibliography	127
Samenvatting	136
Acknowledgment	139
Curriculum vitae	141
Publications	142



# Foreword

The present work started with a diagnostic challenge several years ago. At that time, I was a resident and had begun my training in ophthalmology several months earlier. On my side of the ward a young woman had been admitted with severe, malignant Graves' orbitopathy. She had previously undergone orbital decompression surgery twice to prevent blindness from optic neuropathy. Although her clinical picture had improved as a result of surgery, she suffered from a depressed mood due to her extreme chronic diplopia, which was aggravated by concurrent myasthenia gravis. Even though several attempts were made to correct her diplopia surgically, it remained resistant to therapy. Computed tomography and magnetic resonance imaging showed increased extraocular muscle diameters, but no other abnormalities. A non-invasive method seemed called for to measure the motion of the tissue in her orbit, since an invasive procedure carried a too large risk of inducing more scar tissue and increasing ocular misalignment.

By then, I was working in ophthalmology exclusively and was starting to feel estranged from computer science. I had experienced the opposite feeling several years earlier, when I had been working in information technology, and had missed medicine at that time. In the hope of finally having found a subject where I could combine two fields, imaging science and ophthalmology (not necessarily in that order), I took up the challenge. M.Ph. Mourits, MD, PhD, then my supervisor, concurred with me that it might be interesting. When he asked me whether it would take a long time to develop such a method, I replied that given my considerable experience as an IT consultant, I expected to have it working within a few months.

Naturally, it took a little bit longer. Now, after more than six years, I am ready, and this thesis is the result.



# 1

## Introduction

The introduction briefly describes the orbit for readers unfamiliar with ophthalmology: outlining what the orbit is, what it does and what the most important consequences of orbital diseases may be. Next, the introduction explains how motion can be imaged, measured, and visualized for readers unfamiliar with image processing. Finally, it contends why it is important that motion in the orbit is measured objectively.

### 1. THE ORBIT

The orbit is the bony socket of the eye [1]. It forms part of the skull and protects and surrounds the eyeball (or *globe*) and its supporting tissues. The tissues in the orbit function as a flexible seat for the globe so that it can be rotated by the extraocular muscles and be kept in a stable position precluding luxation (dislocation) [53]. The orbit contains the six muscles that rotate the globe in order to gaze [156]. These are called extraocular muscles by ophthalmologists since they are outside the eye. The orbit contains the optic nerve that is the pathway from the retina to the visual cortex and vice-versa, and also the neurovascular tissues that innervate and nurture the eye and its surrounding structures [10;55]. Between these structures lies a fatty tissue, which has been found to contain an intricate network of connective tissue [94].

### 2. GAZING

In order to gaze, the extraocular muscles rotate the eyes. The space in the orbit is fixed and limited by the bony walls of the orbit. This implies that all other structures in the orbit need to move and deform when the eye is gazed [156]. For example, during upgaze the globe rotates upward, the optic nerve at the back of the globe rotates downward and the fatty tissue is deformed and pushed or pulled sideways [96]. I write ‘pushed or pulled’ on purpose, since it is actually not known whether the fatty tissue is pushed by the optic nerve that is moving down, or pulled by the fibromuscular attachments to the muscle [141]. The rotation of the eyelids over the eyeball is semi-dependent on gaze position. Connective tissues such as the



Figure 1. Disfiguring effect of Graves' orbitopathy. 1a. (left): before Graves'. 1b (right): 9 months later, with active orbitopathy. The patient suffers from proptosis, slight exophoria (outward turning) of the right eye, eyelid retraction and upper eyelid thickening. This leads to von Graefe's sign (startled appearance). Reproduced with permission.

Whitnall and Lockwood ligaments subtly interact with the extraocular muscles [64]. The motion and deformation of the orbital fat and the optic nerve are related in a non-linear manner to the movement of the muscles and the globe. Thus, even a simple monocular upgaze is the result of the complex interaction of more than ten orbital structures.

The point is that during gaze all tissues in the orbit move and deform interdependently. The description of changes in spatial relationships of orbital tissues as a function of gaze is called *functional anatomy of the orbit* [113].

### 3. ORBITAL DISEASES

The two main functions of the tissues in the orbit are to enable the eye to gaze and at the same time keep the globe in a stable position. In diseases of the orbit, one or both of these functions may become impaired. If gaze is impaired, diplopia (double vision) and other ocular motility disturbances can result. If the stable position is impaired, proptosis may result, a condition in which the globes protrude. The globe can also retract, a condition called enophthalmos that will not be discussed further. Only in rare cases of extreme proptosis do the globes actually luxate [40].

The study and treatment of diseases of the tissues in the orbit is called orbitology [128;129].

The most common orbital disorder in adults is Graves' orbitopathy, a disease related to hyper- or hypothyroidism, in which the orbital tissues become inflamed [73;128]. The incidence is approximately 0.4% in the general population, and the female to male ratio is approximately 7-10:1. It can cause swelling and fibrosis of the extraocular muscles and the intraorbital fat [83;136;137]. This can lead to problems with gaze and diplopia on one hand, and proptosis on the other hand [48;57;157]. See Figure 1 for the disastrous consequences this may have on the face.

Disfiguring proptosis can be treated effectively by decompression surgery [118;129;137]. Decompression surgery itself may postoperatively give rise to ocular motility disturbances for yet unknown reasons [49;56;70;87;88;105;110;121;122;130;132;151]. Apart from Graves' orbitopathy, other space-occupying lesions may also be found in the orbit. Most of these usually also impair either one or both functions of the orbital tissues and may thus give rise to diplopia, proptosis or both.

Unrelated to orbital diseases *per se*, the anophthalmic socket can also be thought of as a disorder of the orbit. The anophthalmic socket is the result of enucleation, a procedure in which the globe is removed from the orbit for a variety of ocular disorders, such as malignant tumor, trauma, or infection. After enucleation, an implant is placed in the orbit to improve cosmesis and the motility of the prosthesis (the "glass eye") [10;36;142]. In some instances, persistent intractable pain may arise in the anophthalmic orbit, sometimes years after enucleation. This is pain which is thought to be rare and for which, so far, no cause has been found [67;133].

The surgery and management of the above disorders of the orbit may eventually benefit if the motion can be measured objectively, either by elucidating their biomechanical mechanisms, assisting in their diagnosis, or both.

It is relatively easy to measure the motion of the eye as a function of gaze, since the eyes are easily observed visually [163] and their motion is readily accessible for inspection. The study of the motion of the eyes is called *orthoptie* (orthoptics) in The Netherlands and, typically, *strabology* in the United States and elsewhere [156]. The motion can be measured more objectively using coils implanted in the sclera [155]. However, the motion of the orbital tissues behind the globe is effectively hidden from view by the orbit, the eye and the eyelids, so that it is very difficult to measure *in vivo*. Attempting to measure motion objectively by introducing instruments or other devices into the orbit is not yet an option. The risk of damaging the optic nerve and consequently causing blindness is simply too large. Additionally, such instruments may influence the very motion they are supposed to measure.

In this thesis, I propose an alternative, namely, to measure the motion first by imaging it and then by using image analysis techniques to measure the motion objectively.

#### 4. IMAGING TISSUE MOTION

A suitable medical imaging device constructs an image, or a series of images, from some regionally varying physical property or properties of the tissues. An image is an ordered set (usually, but not necessarily, on a regular grid) of vectors, where each of the vectors represent the magnitude of one or more of the measured physical properties. The term modality is used to discriminate different imaging techniques as to the physical property they image. Computed tomography (CT) is a modality in which the image is constructed from radio-opacities of tissues, magnetic resonance imaging (MRI) is a modality in which the image is constructed from the durations of time the nuclear spins in tissues need to realign themselves, etc.

Every modality has its own advantages and disadvantages, which influence its usefulness to image tissue motion and the choice of the method to quantify the motion. The most attractive modalities to image tissue motion are CT, MRI and ultrasound. CT has high resolution and excellent bone detection, but is limited by its high radiation load and lower intra tissue contrast. Ultrasound is flexible, since the patient does not need to be inside a scanner, but limited not only by the requirement for skilled operators, but also because ultrasound cannot penetrate the deeper regions of the orbit at acceptable ultrasound levels in the retina. MRI has the advantage of high soft tissue contrast, large imaging depth (depending on the type of coil) and the absence of radiation load; however, image acquisition is usually slower than CT scanning, commonly on the order of minutes. Subjects need to fixate during this period and are not allowed to blink [31;41].

To overcome such disadvantages and to be able to use MRI effectively for imaging tissue motion in a clinical setting, a new fast cinematic (see below) MRI protocol was developed for this study, which allows the acquisition of high resolution images or volumes within 6 to 16 seconds [6;146]. This protocol is described extensively in Chapter 3.

Though MRI and CT can image real-time motion (called dynamic MRI respectively CT) in the heart, they are at present too slow to image real-time motion in the comparatively small orbit at acceptable resolution [41]. This implies that motion imaging usually requires some sort of *cine* (from *cinematic*) acquisition. In this type of acquisition, the tissues are allowed to move over the full range of motion with small increments. After every increment (stop), a new image is acquired (shoot). The result is a sequence of images, which together describe the motion of the tissues. The motion is then made visible by rapid replay of the stop-shoot sequence as a movie.

The difference between dynamic and cine acquisition is relative, not absolute, since in the limit where the time increments are very small, cine acquisition is the same as dynamic acquisition. The term *cine* derives from *cinematic*; the stop-shoot technique is comparable to cartoon animation. Orbital cine imaging techniques as used by various researchers are covered in detail in Chapter 2. The next section gives a brief overview of some of the results obtained by orbital cine imaging.

## 5. MOTION IMAGING STUDIES OF THE ORBIT

The study of the functional anatomy of the orbit has developed into an active area of research [41] around 1989, when MR imaging techniques became widely available [103]. Chapter 2 is a review of the state of the art of this field in 1997. It covers the new information that had by then become available on the role of connective tissue in determining rectus muscle paths [113;116], oblique muscle paths [42], the role of connective tissue ligaments in eyelid motion [69], the deformation of orbital fat [96], and the optic nerve path [141]. Ocular muscle disturbances had been imaged [13;27;85;135;146], including the strabismus associated with Graves' orbitopathy [14], high myopia [95] and orbital floor fractures [150]. The motion in the anophthalmic socket had also been studied [65].

It is important to understand that cine imaging by itself can image, but not measure motion. Visual inspection, however informative, is subjective, and has limitations with respect to intra- and inter-observer variability, absolute measurements and correlation with disease parameters. Motion imaging techniques will become more useful if objective measurements of motion can be made. For example, if an ocular muscle disturbance is characterized by a decrease in abduction of  $y$  degrees and objective motion measurement shows a decrease of motion of  $x$  millimeters per degree of gaze,  $x$  and  $y$  can be correlated with each other. The next section will describe approaches to measure motion of tissues objectively.

## 6. MEASURING TISSUE MOTION

Before discussing how tissue motion can be measured from images, it is important to define it. Image motion can be defined as a vector field that describes a mapping from the image at one moment in time to the image at another moment in time. The mapping it defines, and by extension the motion field itself, can be classified as being of the rigid, affine, projective, elastic or fluid type [154]. These types are consecutively less constrained.

Global, rigid motion constrains the mapping to be a combination of global translations and rotations only. Affine motion additionally allows a deforming mapping, constraining the deformation so that parallel lines map onto parallel lines (thus, shearing and scaling are allowed). Projective motion constrains the deformation so that straight lines map onto straight lines. Finally, elastic motion constrains the deformation to preserve continuity, so that lines map onto curved lines. In fluid motion, the continuity constraint is also removed, so that lines can map onto any point(s). Each motion type can itself be classified as being global or local (piecewise), where local means that the above types apply to regions of the image instead of the whole image. In this thesis, the term "tissue motion" is used to denote local elastic motion.

Imaging science offers a number of approaches to measure motion objectively from image time sequences [71;152]. Many approaches to determine motion were originally based on theoretical research of the neurophysiology of vision [77;91].

The first medical applications of image motion analysis were in cardiology, in order to determine ventricular wall motion [62]. Image analysis methods to determine motion can be classified into two general categories: retrospective and prospective. Retrospective methods quantify motion from image or volume sequences, without special constraints on acquisition. Examples are feature matching, correlation and gradient optical flow methods. Prospective methods quantify motion using special acquisition techniques, for example landmark tracking and cine Phase Contrast MRI (PC-MRI).

- ◇ Feature or token matching methods define motion as the shift that yields the best fit of image features at different times [28;106;149]. Different feature detectors have been used to localize boundaries, corners or features that are more complex. After a feature has been localized, the motion is estimated as the best match of the feature in the next image in the sequence by maximizing a similarity measure such as the normalized cross-correlation or minimizing a distance measure, such as the sum of squared difference. A disadvantage of feature matching applied to tissue motion is that tissue boundaries but not the tissues themselves can be tracked. In the orbit many tissue features are present in a small space, which compounds this problem and gives rise to the correspondence problem of ambiguous potential matches.
- ◇ Region matching methods define motion as the shift that yields the best fit between image regions at different times [24;97]. The best match of a region is found using the same methods as in feature matching methods. Region matching is computationally more expensive than feature matching. In addition, region matching will usually obtain a motion field similar to that found using feature-matching methods, since region cross-correlation is often the highest around image features.
- ◇ Landmark tracking involves implanted or induced landmarks. Surgically implanted radio-opaque landmarks can be imaged by CT, and the motion of the landmarks can then be used to measure motion [80]. Implanting landmarks in the orbit is not attractive, since this would entail a serious risk to the optic nerve and may influence the very motion it is meant to measure. Induced landmark methods, known as MR-tagging, involve changing the gradient over tissues in a regular way during image acquisition [164]. The grid formed by these tags is sparse in comparison to the size of the orbit with currently available tagging methods. Therefore, only a few tags cover the orbit and only rough estimates of motion are possible.
- ◇ Cine Phase Contrast (PC) MRI [15;123] employs the phase changes of the MR signal due to tissue motion. It is well suited to determine relatively regular and large motion fields. It is less suited to determine non-translational motion, especially the combination of translation, rotational and shear motion fields that occur in the orbit.

- ◆ Differential or gradient optical flow methods use changes of intensity or of intensity phase that are the result of motion [19;20;78]. In principle, spatial characteristics of the image, such as features, are disregarded. Complex motion interactions can be measured at a smaller scale than is possible with MR-tagging. A disadvantage of optical flow methods is that certain constraints (typically regularity assumptions) need to be placed on the motion for accurate estimation.

The present work elaborates on optical flow methods. The next section introduces optical flow and its potential to measure tissue motion.

## 7. OPTICAL FLOW COMPUTATION OF MOTION

In theoretical neurophysiology, optical (or optic) flow<sup>1</sup> processing is the term for the physiological process by which stereopsis and motion are derived from the different images that impinge on the retina of both eyes, respectively from the changing image that impinges on the retina of a single eye [79;89]. The term was first proposed by Gibson in 1950 [66]. In animals, estimation of optical flow occurs both in the retina and in the cortex (in hominoids predominantly in medial temporal and medial superior temporal cortex). Physiologically, estimation of optical flow is usually thought to be the equivalent of the computation of spatial and temporal derivatives of image intensity or phase [89;107].

In image processing literature, optical flow processing is defined as the computation of the optical flow field. Central to optical flow computation is the notion that the intensity of image regions remains approximately constant during motion. This notion is called the Optical Flow Constraint Equation [20;78] and can be expressed mathematically as:

$$\nabla I(\mathbf{x}, t) \cdot \mathbf{v} + I_t(\mathbf{x}, t) = 0 \quad (1)$$

with  $I(\mathbf{x}, t)$  the image intensity at location  $\mathbf{x}$  and time  $t$ ,  $\mathbf{v}$  the optical flow field [66],  $\nabla I(\mathbf{x}, t)$  the spatial intensity gradient (the first order derivative), and  $I_t(\mathbf{x}, t)$  the partial derivative of  $I(\mathbf{x}, t)$  with respect to time.

This equation is under-determined (note that it has two unknowns, the x- and y-components of the vector  $\mathbf{v}$  in the two-dimensional case), so that  $\mathbf{v}$  cannot be determined. Therefore, most optical flow methods employ a two-stage system to solve the resulting system. This may represent an analogy to the mammalian visual system [39;79]. In the first stage, possibly analogous to processing in the retina and early visual cortex [58;86], the spatio-temporal patterns in the image sequence are decomposed into components or primitives on the basis of the optical flow constraint equation [20]. The methods then differ in the way they place additional constraints on the optical flow field in a second stage [19;76;78;101;138;149;153], which may be analogous to post-retinal or cortical processing [54]. The standard OFCE takes into account only a single scale at which  $\mathbf{v}$  is computed; the estimate

---

<sup>1</sup> The term *optical* flow as opposed to *optic* flow is used because it is the more common (www.google.com: 13100 hits for “optical flow” versus 4400 hits for “optic flow” on July 4, 2001).

for  $\mathbf{v}$  can be much improved by generalizing the OFCE using a scale-space approach [120].

Optical flow methods have been extensively evaluated using natural image sequences acquired by optical means, i.e. with image intensities constructed from the reflections of light from a motion scene [19]. Natural image sequences on one, and sequences obtained by CT, ultrasound or MR (called *medical* image sequences in the present work) on the other hand, are usually treated as equivalent. This explains the use of optical flow computation methods to estimate the motion field from radiological image sequences [11;18;47;51;62;104;120;165]. To my knowledge however, the validity of this equivalence has not been well studied. It is important to stress that the intensities in medical motion image sequences are acquired by a very different physical mechanism than in natural light reflection images. For example, in T1 MR imaging, the image intensities reflect the average time needed for the spins of the nuclei in a small three-dimensional tissue region (known as voxel) to return to equilibrium after a radiofrequency pulse. Subtle problems may be introduced if the difference between the images acquired with different modalities is not acknowledged, such as the anisotropic phase effect of the orientation of the tissue relative to the gradient of the MR field. This is caused by RF coil inhomogeneity and susceptibility artifacts. Additionally, medical image intensities are discrete *samples* out of a continuous 3D space, so that partial volume effects and other effects of the sampling method also influence the image. The issue is elaborated in Chapters 4 and 5.

Most optical flow methods are limited to two dimensions. This is logical since the images on our retinas are two-dimensional. Nevertheless, tissue motion is three-dimensional, so it may therefore be preferable to estimate the optical flow in three dimensions also [72;144]. For the present work, a fast cine MRI protocol has been developed to acquire sequences of three-dimensional volumes with acceptable fixation times (15.6s). The motion in these volume sequences can be measured with a newly developed three-dimensional gradient optical flow algorithm. The objective measurement of three-dimensional orbital tissue motion is studied in Chapter 5.

## 8. VISUALIZATION OF MOTION

Objective measurement of motion by optical flow results in optical flow fields. Particularly if 3-D optical flow is measured, the computations result in huge numbers of motion vectors, in the orbit on the order of 150K vectors per measurement. In order to understand the relation of the motion of tissues to each other, the fields have to be visualized, preferably in combination with the underlying anatomical tissues. In other words, both form and function are to be visualized in an image, preferably multimodal.

There is extensive literature on the visualization of the two- and three-dimensional motion of fluids and gases. The first to visualize two- and three-

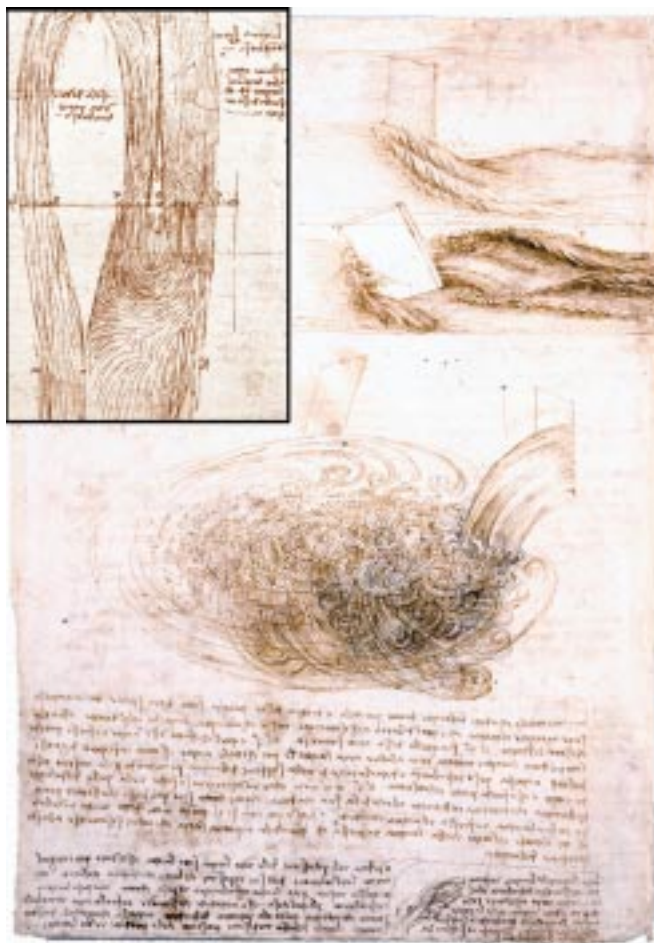


Figure 2. *Water Formations* (RL12660 verso, ca. 1507-1509) by L. da Vinci. (Center) Three-dimensional visualization of the vortices in a through, and (top) water rushing past a board in a stream. (inset) visualization of the two-dimensional flow in a riverbed: the first hedgehog plot! The Royal Collection © 2001, Her Majesty Queen Elizabeth II. Reprinted with permission.

dimensional fluid motion was Leonardo da Vinci, who, around 1500, used wood shavings floating in water to sketch the two-dimensional flow of water in a river bed and the three-dimensional vortices created by water falling from a square spout into a round trough. See Figure 2.

Since then, many approaches to visualize the dynamic behavior of fluids and gases have been developed [109;162].

Two-dimensional flow fields can be displayed using either glyphs or textures. *Glyphs* are small graphical icons [19] displayed on a sparse grid. If the glyphs are

arrows, the visualization is known as a hedgehog plot. Glyphs are effective if the local direction of the flow is more important than global aspects such as the presence of shear or vortices. Complex flow is difficult to visualize, because the grid is sparse and one glyph may occlude another, if the flow magnitude is not normalized. Also, either the average flow over a large region can be displayed, or the specific flow at only a limited number of locations. *Textures*, such as streamlines (as in Figures 2a and 2b), spotnoise and line integral convolution [25;161] visualize the trajectory of the flow in the form of a texture convoluted by the direction of the flow. The grid is denser so that global aspects are more effectively displayed, but individual flow vectors are lost. For two-dimensional techniques, additional flow properties can be displayed in the form of color. The visualization of flow fields using a combination of textures and colored glyphs is studied in Chapter 4.

The visualization of three-dimensional flow is more difficult, since it involves the projection of the three-dimensional motion vectors from a three-dimensional space onto a two-dimensional plane. A large amount of condensation is required for this dimension reduction, especially if the underlying anatomical data also need to be displayed.

Approaches that have been published include glyphs, streamlines in the form of three-dimensional line integral convolution [109], streamballs [23] and particles [37;160]. Since glyphs easily overlap and hide each other, they are most useful to study the flow near boundary surfaces [109]. Banks [17] used monochromatic glyphs in the form of artificial fur and volume rendered these combined with the underlying static image to show the advection of hot air around a sphere. For this technique to be effective, the flow near the surface needs to be regular, or the fur will easily become disoriented. Streamlines, streamballs and particles require regular flow fields for the visualization to be effective. These last methods are less suitable if the nature of the flow field has not yet been established [109].

Research on the visualization of non-rigid, elastic motion is almost non-existent. This is understandable, since two, apparently mutually exclusive, goals need to be met. Because elastic motion (e.g. in the orbit) is complex, one wants to see dense motion fields. However, dense motion fields cause occlusion of details that are more distant and lack depth hints. This precludes the appreciation of the relationship of the motion of different tissues to each other and to the underlying anatomy.

In art however, visualizing the elastic motion of animate and non-animate objects has been a legitimate subject since the 1880's. In fact, the Futurists saw it as the only valid subject of painting, embracing it in 1915 as the ultimate art form in their *Riconstruzione Futurista dell' Universo* [16]. The painting (Figure 3) by Umberto Boccione, one of the Futurists, exemplifies his attempt to visualize three-dimensional motion using colored glyphs that form textures.



Figure 3. *The City Rises* (1910). Painting by Umberto Boccione, Museum of Modern Art, New York. Mrs. Simon Guggenheim Fund. Oil on canvas, 6' 6½"×9' 10½." Photograph © 2001, The Museum of Modern Art, New York. Reprinted with permission.

Chapter 5 introduces a new method, the rendering of scintillations of the visualization of non-rigid, elastic, three-dimensional motion that elaborates on the work as discussed above and techniques of the type used in this painting. The effectiveness of scintillations was studied for visualizing the motion of the connective tissue around the optic nerve.

## 9. DESCRIPTION OF THE THESIS

The research questions, as sketched in the Foreword, were whether a non-invasive technique for the objective measurement of orbital tissue motion can be developed, and if so, whether such a technique might be clinically useful in orbital disorders, including the diplopia that may occur after orbital decompression surgery.

Reflection leads to the following imaging science questions:

- ◆ how can the motion in the orbit be imaged using MR in a way that is acceptable both to the patient, i.e., as fast and comfortably as possible, and to the motion analysis algorithms, i.e., as precisely as possible (Chapter 3).

- ◆ can the two- and three-dimensional motion of tissues in the orbit be measured objectively from cine MR images (Chapters 4 and 5),
- ◆ what is the reliability of these measurements and are they adequate for clinical purposes (Chapters 4 and 5),
- ◆ which two-dimensional optical flow algorithm is the most suitable for this task (Chapter 4),
- ◆ can the most suitable optical flow measurement be extended to three dimensions (Chapter 5), and
- ◆ can two- and three-dimensional tissue motion be effectively visualized combined with the underlying anatomy using a combination of glyphs and texture rendering (Chapters 4 and 5)?

and the following ophthalmologic questions:

- ◆ what was the state of the art of the functional anatomy of the orbit in 1997 - when this study was started,
- ◆ can two- and three-dimensional tissue motion be measured in healthy subjects (Chapter 6),
- ◆ is motion measurement clinically useful to localize specific types of orbital tumors (Chapter 6),
- ◆ is motion measurement clinically useful for studying the mechanism of persistent intractable pain after enucleation (Chapter 7),
- ◆ what is the effect of decompression surgery for Graves' orbitopathy on tissue motion and muscle paths (Chapter 8), and
- ◆ what is the mechanism of ocular motility disturbances caused by decompression surgery (Chapter 8)?

The General Discussion at the end of this thesis summarizes the findings and puts them in perspective.

All patients and subjects were treated in accordance with the tenets of the Declaration of Helsinki. The research protocol for all studies and the informed consent form used in the studies in Chapters 3-8 were approved by the Institutional Review Board of the *University Medical Center Utrecht* (97/113). All patients gave prior written informed consent after the nature of the study had been explained.

# 2

## Functional anatomy studies of the orbit

Presented in part at the *Seventh International Skull Base Society Meeting*, Rotterdam, the Netherlands, January 1999.

### 1. INTRODUCTION

*Functional anatomy of the orbit* is the branch of science that describes the changes in spatial relationships between orbital tissues as a function of gaze [41;113]. For a description of the static anatomy I refer to the appropriate texts [53;55;55;64;93]. New imaging techniques, including *cinematic*, *dynamic* and *functional* MRI have become available recently [103]. They allow visualization of the macroscopic functional anatomy of the orbit *in vivo* in a manner previously impossible. The purpose of this chapter is to give an overview of the insights these new techniques have allowed. The various imaging methods will be introduced first, followed by a review of the results and implications thereof for the normal functional anatomy. Finally, the implications of pathologic changes in functional anatomy will be discussed.

### 2. IMAGING TECHNIQUES

*In-vivo*, functional anatomy can be studied in humans with non-invasive, imaging, modeling and invasive methods. The advantages of the first two over invasive methods are that they are more acceptable to patients, carry less risk to visual function and do not interfere with orbital motion. Non-invasive methods include *orthoptic* examination and monocular duction measurements [119;156]. These methods are able to show abnormal rotation of an eye. However, it is difficult to interpret such results in terms of etiology because changes in different orbital structures may result in the same type of restriction. Modeling methods deserve mention because they have been helpful in the interpretation of imaging studies and may open new avenues for research [117]. Only imaging methods will be discussed in the remainder of this chapter.

Author	Year <sup>1)</sup>	n	Machine	Coil	TE ms	TR ms	Scan Time <sup>2)</sup>	Voxel mmxmmxmm	Fixation <sup>3)</sup>	n pos <sup>4)</sup>	Registration <sup>5)</sup>	Quantification <sup>6)</sup>	Objective
Abramoff	1997	15	Phil 1.5T	head	6.9	12	0:06	3x1.5x1.5	m	11t-10s	a	ao	Enucleation: tissue velocities
Abramoff	1998	18	Phil 1.5T	head	6.9	12	0:06	3x1.5x1.5	m	11t-10s	a	ah	optic nerve: motion path
Bailey	1993	36	? (FISP)	?	?	?	0:15	?	m	6t-6s	-	-	pilot
Bailey	1996	25	Siemens?	?	?	?	0:15	?	m	-	-	-	Graves: muscle shape
Bloom	1991	2	0.4T	head	?	?	?	5x?x?	?	3t- 3t	-	mc	Duane: rectus path
Bloom	1993	9	GE 1.5T	neck	?	?	1:40	?	m	5 t	-	-	Rectus palsy: ↓ diameter
Cadera	1992	1	GE 1.5T	?	?	?	1:40	3x2x2	m	3 t	-	-	Duane: rectus cocontraction
Cadera	1994	07	Signa 0.5T	neck	?	?	2:08	? x?	-	d	-	-	dynamic MRI feasibility
Clark	1997	13	Signa 1.5T	surface	15	550	3:38	2.5-3x0.39x0.52	m	3x3 c	m	mc	pulley: position
Clark	1998	17	GE 1.5T	surface	15-30	300-817		2.5-3x0.39x0.52	m	3s	-	ms	SO palsy: rectus path
Demer	1994	14	Signa 1.5T	surface	15	550	3:38	2.5-3x0.39x0.52	m	3s-3t	-	ms	Rectus palsy: ↓ diameter
Demer	1995	35	GE 1.5T	surface	15-30	300-817		2.5-3x0.39x0.39	m	8 c	-	ms	SO palsy: MR path
Demer	1996	2	GE 1.5T	surface	15-30	300-817		2.5-3x0.39x0.52	m	3x3 c	-	ms	rectus path / pulleys
Goldberg	1992	3	GE 1.5T	surface	25	300	2:38	3x0.16x0.16	m	3 s	-	-	upper eyelid: kinematics
Goldberg	1994	5	GE 1.5T	surface	25	300	2:38	3x0.16x0.16	m	3 s	-	me	lower eyelid: kinematics
Jaeger	1997	6	Siem 1.5T	head	2.2	4.5	0:00:02	5x2.5x1.95	-	d	-	-	dynamic MRI feasibility
Jewell	1995	33	Siem 1.5T	head	7	17	0:15	4x?x?	m	3s-3t	-	-	pilot
Krzizok	1997	37	Siem 1.5T	head	15	140-200	0:50	3x1.3x0.8	m	3s-3t	-	mp	High myopia: rectus path
Lasudry	1990	4	GE 1.5T	surface	25	300	2:18	3x0.31x0.31	m	4 s	-	mt	intraconal fat: volume shift
Mehta	1994	2	GE 1.5T	surface	15-30	300-817		2.5-3x0.39x0.52	m	3x3 c	-	ms	SO myokymia: ↓ diameter
Miller	1989	4	0.5T	surface	1.5	100	?	3x1.2x1.2	m	3x3 c	-	ms	rectus path
Miller	1993	5	0.5T	surface	1.5	100	3:38	3x1.2x1.2	m	3x3 c	-	ms	rectus path
Scheiber	1997	20	Brük 2.0T	head	17	600	0:20	3x1.0x1.3	o	15 t	-	-	pilot optic fiber fixation
Shin	1996	4	GE 1.5T	surface	1.5	100	3:38	3x1.2x1.2	m	3x3 c	-	-	Complicated strabismus
Smiddy	1989	1	?	head	?	?	?	?	m	2 t	-	-	optic nerve: path
Totsuka	1996	19	1.5T	surface	19	180	0:37	4x1.5x1.5	m	7 s	-	-	orbital fracture: IR path

Table 1. Overview of published cinematic MRI studies up to 1997. 1) Number of patients 2) Fixation time in min:sec:ms per gaze position. 3) Patient fixation method: - = none, m = marks on inside of scanner bore, o = fixation lights using optic fibers or similar. 4) Number of fixation positions: t = in horizontal plane, s = in vertical plane, c = cardinal positions, d = dynamic study. 5) Registration of sequences: - = none, m = manual, a = automated. 6) Quantification: - = none, m = manually: mc = centroid of muscle surface boundary, ms = muscle cross-section, mp = muscle path position, mt = 2D tissue surface, automated: ao = automatic optical flow, ah = heuristic segmentation. Phil = Philips Medical Systems, Best, the Netherlands. Siem = Siemens Medical Systems, Erlangen, Germany, GE = General Electric, Chicago, IL. IR = inferior rectus path, SO = superior oblique muscle, MR = medial rectus path

Methods that have been used in functional anatomy research include:

- ◆ Cinematic CT. In the past important results have been obtained with this method [139]. Because of the radiation load and other reasons this has been abandoned in favor of:
- ◆ Cinematic or *Cine* MRI. In this method, multipositional MRI scans are acquired in a shoot-stop manner with the patient gazing at different (2-12) marks inside the scanner bore. Eye convergence is usually avoided by occluding one eye [43]. The scan sequence can be played back rapidly resulting in an animation of the functional anatomy. To date only 2D cine MRI studies, usually along coronal, sagittal or transversal planes, have been published.
- ◆ Dynamic MRI. In this method, MRI scans are acquired continuously during gaze. This technique is commonly used in experimental cardiac imaging. Jaeger and colleagues [84] have published the first Dynamic MRI study of the orbit. Their published images are mediocre at best and suffer from motion artifacts [41]. Because agonist and antagonist muscles are simultaneously active during both saccades and fixation, no large advantage of dynamic over cine MRI is to be expected as long as image quality remains much lower.

Table 1 is an overview of the state of the art in this field in 1997. Various authors have tried to improve cine MRI image acquisition: Cadera and coworkers [26] have introduced a form of continuous cine MRI with the subject following a fixation stimulus and scans triggered by stimulus reversal. So far, they have not published any results using this technique. Scheiber and colleagues [131] described an ingenious but elaborate setup using fiber optic cables to avoid ocular convergence of the subject during fixation.

Cine MRI and CT can also be extended using image processing techniques:

- ◆ Manual registration to correct for subject motion during acquisition [43;113]
- ◆ Automatic registration [145]
- ◆ Image enhancement such as noise removal to improve image quality [43]
- ◆ Area and centroid (the weighted center of gravity of a structure) computation to compute muscle cross-sections and centroids [43;113]
- ◆ Curve and shape estimators to determine changes of shape of the optic nerve and other structures [2]
- ◆ Motion estimation to compute tissue velocities automatically, the subject of the present work.

### 3. NORMAL FUNCTIONAL ANATOMY OF THE ORBIT

This section covers the normal functional anatomy of the orbit as studied using cine MRI.

### A) *Globe*

In a sagittal cine MRI study, Lasudry and coworkers [96] concluded that the globe translates over 1.0-1.5mm in sagittal rotation from maximum upgaze to maximum downgaze opposite to the direction of gaze, and on lid closure, 1.9mm superoposteriorly. Clark and colleagues [31] found that the anteroposterior displacement for up to 30° rotation remains less than 0.4mm.

### B) *Rectus muscles*

In an extensive study of four subjects using quantitative cine MRI in the coronal plane, Miller and Demer [114] were the first to publish the rectus muscle pulley concept. They found that the rectus muscles do not show sideslip over large gaze changes but keep their position with respect to the orbit. They also measured the increase of muscle cross-section on contraction: mean increase in cross-section for the lateral rectus muscle is 35% with a maximum of 32.3mm<sup>2</sup>, for the medial rectus muscle 30% with a maximum of 30.3mm<sup>2</sup> and for the inferior rectus 46% with a maximum of 33.6mm<sup>2</sup>. The point of maximal cross-section shifts posteriorly on contraction.

Demer, Miller and coworkers [45] in a cine MRI study of 35 subjects confirmed that the path of the rectus muscles remains stable relative to the orbit over 40 degree rotations until just posterior to the equator. They concluded that the positional stability is caused by the pulleys. The existence of these musculo-fibrous structures, which were found to be continuous with the orbital wall, has been confirmed histologically.

Clark, Miller and Demer [31] found that the position of the pulleys is uniform across subjects and remains so during gaze changes. They never moved more than 1.0mm. The only exception was the inferior rectus pulley that was displaced horizontally for up to 1.3mm during up- and downward rotation of the eye, probably caused by transmission of the action of the inferior oblique to the inferior rectus pulley by Lockwood's ligament. They concluded that the functional origins of the rectus muscles are the pulleys. The finding that the inferior and superior rectus muscle thicken and retract, with the thickest cross-section shifting backwards upon contraction, has been confirmed qualitatively in the studies of Lasudry and coworkers [96] and Scheiber and associates [131].

### C) *Oblique muscles*

In a study of seven subjects, Demer and Miller [42] found that the cross section area of the superior oblique is on average 19 mm<sup>2</sup>, with an increase in cross section on downgaze (+7.6mm<sup>2</sup>) and a decrease on upgaze (-5.5mm<sup>2</sup>). On contraction, the point of maximal cross-section shifts posteriorly as in rectus muscles. The contraction and relaxation during gaze changes occur mainly in the posterior (nontendinous) half of the muscle.

Lasudry and coworkers [96] found that in upgaze the inferior rectus muscle is covered by the inferior oblique muscle and that these muscles disengage in

downgaze. The anterior shift of the inferior oblique on downgaze is only 50% of the anterior shift of the inferior rectus insertion.

#### *D) Eyelids, Lockwood and Whitnall Ligaments*

Goldberg and colleagues [69] describe the kinematics of the upper eyelid. They found that on downgaze the levator aponeurosis remains static relative to the orbital rim and conclude that Whitnall's ligament functions as a pulley for the levator aponeurosis. They also found that the orbital septum is taut on downgaze.

Lasudry and associates [96] confirmed these findings and demonstrated that on upgaze the septum is folded under the pre-aponeurotic fat pad. They concluded that there is a tight linkage between the tarsus and Lockwood's ligament. They also found that on downgaze, lid retraction is mainly effected by the inferior rectus muscle.

Goldberg and colleagues [69] also described the kinematics of the lower eyelid. They found that both eyelid margin and the anterior inferior oblique margin move much less than the globe. In fact, the anterior capsulopalpebral fascia itself, the main skeleton of the lower eyelid, does not stretch on downgaze. The stretch is located posteriorly to the inferior oblique muscle.

In the study by Clark, Demer and Miller [35] cited earlier, evidence was found that the action of the inferior oblique is transmitted to the inferior rectus pulley by Lockwood's ligament, and shifts this pulley horizontally.

#### *E) Optic nerve*

In a cine MRI study of the optic nerve, Smiddy and coworkers [141] described the optic nerve path in primary position and on superonasal rotation. Abramoff and colleagues [2] quantified the optic nerve path during horizontal gaze changes automatically using heuristic segmentation. They found that in control subjects the optic nerve path is curved and nonlinearly related to the rotation of the eyeball. They proposed that the curved path is due to the network of connective tissue in the posterior orbit first described by Koornneef [53;93].

#### *F) Orbital fat*

Scheiber and colleagues [131] concluded from a qualitative cine study that the motion of intraorbital fat and connective tissue is limited. However, Lasudry and coworkers [96] carefully measured the shift in position of intraconal fat caused by gaze changes. They found that the volume of intraconal fat displaced by the optic nerve is about 0.56ml between upgaze and downgaze, and that on average 37% of the pre-aponeurotic fat pad is shifted laterally during upgaze. They concluded that the orbital fat has semi-fluid properties and its motion is quite extensive. They proposed that this behavior is related to the connective tissue septa.

### *G) Orbital soft tissue*

In a number of pilot studies, Abràmoff and colleagues [4-6;145] employed cine MRI and optical flow motion estimation to measure the motion of the eyeball and other soft tissues.

## 4. PATHOLOGIC CHANGES OF FUNCTIONAL ANATOMY

For the purpose of clarity, the findings are listed by disorder, and not by tissue.

### *A) Strabismus related to rectus muscles*

Bloom and associates [21] reported qualitative cine MRI evidence of reduced transversal and coronal muscle cross section in patients with IIIrd or VIth nerve palsies.

Demer and Miller [43] found that in patients with rectus muscle palsy, the cross-section of the paralytic rectus muscle was reduced (from 45.0 mm<sup>2</sup> to 29.4mm<sup>2</sup>) and its maximum cross-section had shifted anteriorly. The authors proposed that both these changes indicate chronic denervation atrophy of the involved muscle.

Clark, with Demer and Miller [31], found that pulley positions are uniform among control subjects and patients with incomitant strabismus. In two patients with strabismus, however, pulleys of rectus muscles were displaced perpendicular to their plane of action, and the authors suggest that this might be related to these patients' poor response to strabismus surgery.

### *B) Strabismus related to superior oblique palsy*

Demer and Miller [42] studied seven patients with chronic superior oblique palsy using coronal cine MRI. They found a reduction in muscle cross-section (average - 4.4mm<sup>2</sup>) and decreased change in cross-section during gaze. They concluded that superior oblique palsy is characterized by atrophy manifested by reduced cross-section, and absent contractility manifested by lack of increase in cross-section and of posterior displacement during down gaze.

Clark, Miller and Demer [32] showed that in patients with superior oblique palsies, the pulley of the medial rectus is displaced 1.1mm superiorly on average. They proposed that this shift is related to atrophy of the adjacent superior oblique belly, but does not explain superior oblique palsy deviations.

### *C) Strabismus related to orbital fractures*

Bailey and coworkers [13], and Jewell and coworkers [85] have presented sagittal cine MRI studies of orbital floor fractures. Both gave only anecdotal qualitative descriptions of inferior rectus entrapment. Their statement that their methods add to static CT or MRI evaluation of orbital floor fractures is not supported by their findings, however, since entrapment is more effectively diagnosed with cover, prism and other tests of ocular motility and forced duction testing. In orbital floor

fractures, reduction of upward rotation is more common than reduction of downward rotation.

Totsuka and associates [150] have used sagittal cine MRI to study this phenomenon and found evidence that connective tissue becomes entrapped in the fracture. The inferior rectus was usually not involved. They concluded that entrapment might limit muscle relaxation more than contraction because of the usual position of entrapment at the weakest, middle part of the orbital floor.

Shin and colleagues [135] studied two patients with orbital floor fractures, using sagittal and coronal cine MRI. They found evidence that in one patient the inferior rectus had been lost, while in the other there was potential for reattachment. These findings influenced surgical management of these patients.

Abràmoff and coworkers [2] have applied MRI-dynamic color mapping (See chapter 5) in two patients with orbital floor fractures. They found that the optic nerve path is more nonlinear (4.5mm maximum) in these patients and proposed that this is caused by fibrotic changes in the connective tissue skeleton in the posterior orbit, and that the optic nerve path can be used as an indicator of such changes.

#### *D) Strabismus as a complication of surgery*

Miller and Demer [115] have presented evidence that it is difficult to disrupt the pulleys in normal strabismus surgery. They reported that rectus muscle paths are not influenced in spite of aggressive transposition surgery for A and V pattern misalignment with transpositions of up to 10mm.

Shin and coworkers [135] presented the results of coronal and sagittal cine MRI in two cases of complicated strabismus after endoscopic sinus surgery, with loss of rectus and superior oblique muscle segments. These studies influenced patient management. They concluded that clinically adequate information about an extraocular muscle might often be determined by simple visual inspection of cine MRI scans.

#### *E) Duane's syndrome*

Bloom and coworkers [22] were the first to study two patients with Duane's syndrome and dissociated vertical deviation (DVD) with coronal cine MRI. They found no significant vertical displacement of either medial or lateral rectus muscles on up- and downgaze.

Cadera and associates [27] presented anecdotal evidence of co-contraction of the medial and lateral rectus muscles by visual inspection of cine MRI. Similar results were reported by Bailey and colleagues [13] and Jewell and coworkers [85] in 3 patients with Duane's esotropia (apparently the same group).

#### *F) Strabismus related to high myopia*

In an extensive study, Krzizok and coworkers [95] studied 37 patients with high myopia, esotropia and hypotropia using coronal quantitative cine MRI. They found that the path of the lateral rectus is displaced downward in the anterior- and mid-

orbit, a finding that explains the typical deviations. They proposed that this is caused by the increased major axis of the eyeball in high myopia. They found no evidence of mechanical restriction of the globe by the orbital wall.

#### *G) Graves' orbitopathy*

Bailey and colleagues [13], and Jewell and coworkers [85] were the first to study patients with Graves' orbitopathy (apparently the same group). They found enlargement of the rectus muscles and loss of optic nerve movement.

Bailey and colleagues [14] published a study of 25 patients with Graves' orbitopathy using sagittal and transversal cine MRI. They found evidence of rectus muscle stretching in the active, but not the burnt-out phase of the disease, and confirmed their earlier results. They claim that their methods add to the evaluation of patients with Graves' orbitopathy. This claim is not supported by their results. In fact, it is difficult to see how visually inspecting movies can influence management of patients with Graves' orbitopathy.

Abràmoff and coworkers [2] have used quantitative cine MRI in eight patients with Graves orbitopathy and strabismus. They found that the optic nerve motion path is more nonlinear in some patients with Graves' orbitopathy and diplopia.

#### *H) Nystagmus*

Jaeger and coworkers [84] examined three patients with horizontal end-point nystagmus. Using a 5Hz Dynamic MRI setup, they could detect nystagmus up to 5beats/s. They presented the hardly surprising finding that during nystagmus, the contracting rectus muscle shortens and the relaxing muscle lengthens by the same amount. At present, it is difficult to envisage any added value of dynamic or cine MRI in the evaluation of nystagmus.

#### *I) Myokymia*

In a cine MRI study of two patients with superior oblique myokymia (paroxysmal twitching), Mehta and Demer [111] found that the cross-section of these muscles is reduced compared to the normal superior oblique cross-section. They proposed that a IVth nerve insult is the cause of both atrophy and myokymia.

#### *J) Anophthalmic socket*

Ghabrial and colleagues [65] have studied the anophthalmic socket (after enucleation) with cine MRI. In this qualitative study, they found that the motion of the soft tissues in the socket is generally decreased compared to the normal contralateral orbit.

In a pilot study for this thesis, Abràmoff and colleagues [5], studied the motion of soft tissues in the anophthalmic socket with a cine MRI technique. They found that the motion of orbital soft tissues, including muscle, the optic nerve and orbital fat, ranges between 0.0 to 1.4mm per degree of gaze change and is reduced with respect to the normal orbit.

## 5. EXPECTED DEVELOPMENTS IN IMAGING TECHNIQUES

Further improvements are expected in cine MRI acquisition rates and image quality, so that fast cine 3D and dynamic studies may become feasible. Functional MRI may be applied in the near future in the study of dynamic extraocular muscle metabolism. Finally, advances are expected from imaging science, so that quantification of soft tissue velocity, of tissue motion paths and of volume changes of orbital fat and muscles may become available in the clinic in the future.

## 6. DISCUSSION

Our idea of the functional anatomy of the orbit has changed over the last few years due to the results such as those described above. Since the studies of Koornneef [93] it has been acknowledged that connective tissue plays an important role in orbital anatomy and pathology [53]. Anterior parts of this connective tissue network, the muscle pulleys, have been found to form the functional origin of the rectus and inferior oblique muscles, similar to the way the trochlea was already acknowledged to be the functional origin of the superior oblique muscle. Other tissue structures, including Lockwood's and Whitnall's ligaments, seem to form the functional origin for the eyelid retractors. This network may even play a role in the posterior orbit.

Aside from the study of functional anatomy and pathology for research purposes, imaging techniques are gaining acceptance in the clinic. Clinicians use cine MRI to diagnose the cause of different types of strabismus based on changes in muscle cross-section and pulley location and decide on the optimum therapy. It has been possible to evaluate the role of slipped muscle in complicated strabismus after surgery. It can help determine whether connective tissue has become entrapped in orbital floor fractures. It can measure soft tissue motion after enucleation in reduced prosthesis motility. Finally, it may play a role in the localization of tumors if these cannot be localized in a specific tissue on static scans [2].



# 3

## Fast cine MRI of the orbit

Presented in part at the annual meeting of the Radiological Society of North America, Chicago, Illinois, October 1997.

### 1. INTRODUCTION

Reproducibility of results implies precise description of methods. The purpose of this chapter is to help others avoid some of the problems that were encountered in the course of this research while developing orbital cine MRI (Magnetic Resonance Imaging) methods, since journals offer but limited space for method descriptions. The Philips Gyroscan™ NT 1.5T MR scanner running under software release 7.1.2 was used in all studies, but the methods should, generally, carry over to any other 1.5T scanner. The programs used to process MR images are available on the associated website at "<http://www.isi.uu.nl/people/michael>." (see below).

### 2. PATIENT PREPARATION

Careful preparation of the patient prior to the scan is important for successful cine MRI. Cine MRI of the orbit requires active co-operation of the patient during the scan. In addition, the physics of magnetic resonance imaging are difficult to explain in comparison to those of a computed tomography (CT) scan. Therefore, patients are frequently fearful of the procedure without explicitly expressing such.

Our approach was as follows. The patient was asked to participate in the study after the nature of the study had been explained. He or she then received a brochure explaining the cine MRI examination and containing the informed consent form. Among other things, the brochure stressed that he or she was expected to lie perfectly still during the scan, while gazing only with the eyes, and not with the head. Recently, a picture of the scanning procedure has also been added (Figure 1).



Figure 1. NT scanner with patient on dolly outside the scanner bore. The head coil is not in place, the headband has not been fixated and the fixation aid has not yet been fitted.

A separate appointment was commonly planned at least one week later. For practical reasons, this appointment was usually combined with a visit to the treating ophthalmologist. At this second appointment, the details of the procedure were again explained, and any questions were answered, as far as possible. Usually, the informed consent was then signed. The visit also allowed any contraindications (presence of any magnetic metal within the skull, of any magnetizable metal anywhere else in the head, of a pacemaker, of claustrophobia or a history of psychosis) to be ruled out once more.

### 3. MR SCANNING

Practical MR scanning is by necessity a compromise between image quality, the time patients can hold fixation, economical use of scanner time slots and the convenience of the scanning protocol to MR operators. In general, longer scanning times per fixation period increase image quality. Longer scanner time slots allow more time for setup of fixation aids, operator intervention and longer cine sequences. It is difficult, however, to achieve these goals. Long scanning times increase motion and blinking artifacts, since it is difficult to gaze at a fixed target without blinking for an extended period. Scanner time slots are limited for



Figure 2. *Snow White machine* fixation aid.

economical reasons. MR scans were performed by a rotating team of two MRI operators from a pool of about twelve, any one of whom might be on duty at the moment of orbital cine MR scanning. This arrangement precluded elaborate fixation aids, complicated scanning protocols with many options, and extended operator intervention (for example to reposition patients), even though operators were trained for orbital cine MR scanning and a written protocol was available.

We performed many experiments to find an optimal orbital cine MR scanning protocol, given the above constraints. Fixation times over twenty seconds were found to result in motion artifacts, while most subjects and patients could fixate up to fifteen seconds with only small motion artifacts. Consequently, fifteen seconds was estimated to be the upper limit to fixation time. Corneal anesthesia was found not to improve scanning quality if the fixation time was below twenty seconds, and was not used. After it had been shown that objective measurement of motion was possible based on sequences of seven to nine volumes (Chapter 4), the minimal sequence length was set at seven. This allowed us to maximize MR efficiency and minimize patient fatigue, since the patient spent only about 20 minutes in the scanner bore. The time slot was set at 30 minutes.



Figure 3. *Brainwash* fixation aid. Top: View of fixation aid with ends of optic fibers (all of them illuminated for clarity). Note the optic fibers exiting from the back of the device. Bottom: view of sequencer box (left) connected to a bank of LED's (center) that fits under the fiber optic bank (right).

#### 4. GAZE SEQUENCING

Proper gaze sequencing requires the use of fixation marks [41]. The fixation marks could not be left on the inside of the scanner bore, because such marks confused patients that had to undergo functional MRI experiments that are performed in the same scanner; thus, a fixation aid was needed to maximize patient cooperation and minimize operator time for setup. Two different devices were developed and (partially) manufactured by me to serve as fixation aids.

The first device was dubbed the *Snow White machine* (Figure 2) and consisted of a transparent acrylic half-pipe that fits snugly in the scanner bore. On the inside is a row with nine fixation marks indicated with numbers 1-9. This sequence is horizontal and level with respect to the patient's eyes and face in the scanner. The straight-ahead fixation mark is at number 5. The marks are  $8^\circ$  apart if the rotational centers of the eyes are 200mm from it. This 200mm distance was found to be a practical approximation of the average distance of the eyes to the fixation aid. Though extreme gaze positions are attractive, in practice, many patients were unable to gaze. There are also two rows, vertical with respect to the patient's face, one  $20^\circ$  to the left and one at  $20^\circ$  to the right of the straight-ahead fixation mark. The *Snow White machine* was left transparent to minimize claustrophobia.

The other device was dubbed the *Brainwash* fixation aid (Figure 3). It was developed because some patients had difficulty understanding the meaning and order of the marks in the *Snow White machine*. It had generally the same distribution of the fixation marks but small lights were used - instead of numbers. These lights were made to light up one by one in a specific color, synchronized to the cine scanning protocol.

Synchronizing was triggered by the sounds of the MR gradient coil, recorded with a microphone, since an electronic triggering output is not available on the NT (for medico-legal reasons). The lights were actually the ends of fiber-optic cables



Figure 4. Patient being slid into the scanner, the *Snow White machine* is in place.

running from the scanner control room, where they were lit by a sequencer box that contained three-color Light Emitting Diodes (LED's) for every fiber. Three programs were available on the sequencer, selectable by a switch: a program showing a sequence of horizontal white lights, and two programs showing vertical sequences in red and green respectively. The MR operator could start a sequence by the press of a button, and the sequencer then waited for the sound of the activation of the gradient coil before lighting the next light in the sequence. This way, a patient could be instructed to follow the white, green or red lights respectively. Though initial experiments were favorable, the *Brainwash* turned out to be too cumbersome to set up. In the later studies, it was no longer used, and only the *Snow White machine* was used.

The eyes were not occluded. A choice had to be made between either a much (1/4) reduced image resolution (due to halving of the acquisition time) with occlusion or no occlusion. Otherwise, occlusion would unacceptably have increased scan time and patient fatigue, because all scans would have had to be performed twice. It was found easy to determine the horizontal and vertical fixation angles from the cine MRI scans, so occlusion was not needed for this. In addition, it was found that most patients are usually able to fixate consciously with their 'best' eye. Thus, there were almost no sudden flips of the fixating eye during a sequence. This is important because such flips would have resulted in one double image and one missing image in an already very brief sequence.

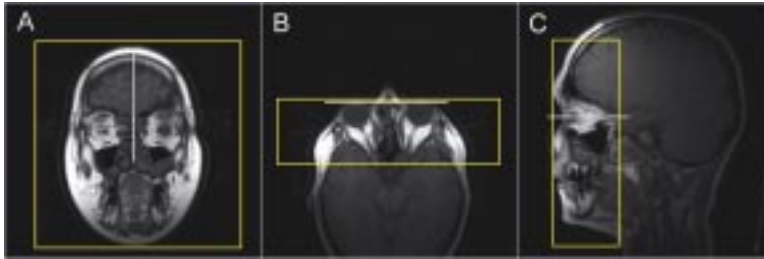


Figure 5. Survey scans. A. coronal plane; B transversal plane; C sagittal plane. The borders of the volume slab that is typically scanned during cine MR scanning are indicated in yellow. The white lines indicate some of the landmarks used to align the patient's head position with the axes of the scanner. In A, the interhemispheric fissure, in B the line connecting the center of both lenses, in C, the line from the globe-optic nerve center to the optic foramen.

## 5. MR PROTOCOL

A head-coil was used in all studies, since a surface-coil was found not to improve results and increase scanning-time [41]. For the earlier studies (Chapters 4 and 6), two-dimensional transversal and sagittal scans were acquired with an acquisition time of 6 seconds per image [146]. After improvements in the NT software (> release 6.0), a faster protocol was developed. This protocol was used in the later studies (Chapters 5, 7, 8), where three-dimensional coronal volumes were acquired with an acquisition time < 16 seconds pre whole volume. Only this last protocol will be covered in detail in this section. Before actual MR scanning, sagittal, coronal and transversal survey scans were made. See Figure 5. These scans were used to check alignment of the orbital axes and to set the scanned volume.

The fast volume protocol had the following settings: Gradient scanning sequence (with Turbo Field Echo), a TE (Echo Time) of 4.598 ms, a TR (Repetition Time) of 9.36 ms, Flip Angle 20 degrees, matrix 256x256, field of view 60%, slice thickness 2.0mm, slice distance 2.0mm. These settings result in anisotropic volumes of 256x256x20 voxels, with a voxel size of 0.82x0.82x2.0mm<sup>3</sup>, and an acquisition time of 15.6s. Foldover suppression was not used, since it increased scanning time by 60%, but did not improve image quality, as the foldover was located outside the orbit.

Three sequences of volumes were acquired using the above settings. One horizontal sequence of 9 volumes with the patient gazing at the horizontal fixation marks, and two vertical sequences of 7 volumes each with the patient gazing at one of two vertical rows. During scanning, the patient was asked to fixate the mark next to the number, and the scanning was started. Between sequences, a brief rest is given to allow the patient to relax. The volume sequences were then saved on Optical Disks (OD). The MR data for each patient were about 70-100 Megabytes (MB). See Figure 6.

## 6. DIGITAL DATA COLLECTION

The Gyroscan™ scanning software stores the scanning data in an image format proprietary to Philips (for medico-legal and commercial reasons). The Gyroscan™ at the UMC Utrecht has no facilities for data transfer or conversion to publicly available imaging formats, such as the Digital Imaging and Communications in Medicine (DICOM) format. (Such an option is marketed by Philips, however). Thus, the imaging data are only available on the Gyroscan™ terminals and on Easyvision™ workstations also supplied by Philips.

The MR data can be converted to a 'normal' format by exporting the data from the Gyroscan™ to Compact Disk-Read Only Memories (CD-ROMs) via an Easyvision™ workstation. The CD-ROM will then contain the volume sequences in the form of separate DICOM 3.0 image files. This method has several drawbacks: each CD-ROM can contain the data of only about 4-5 patients and it takes about three to four hours to write such a CD-ROM. More important, all volume and sequence information is subsequently lost, and the volume sequences are stored flat as separate DICOM image files with non-mnemonic names of the form IM\_0699. About one in two CD-ROMs thus obtained were unreadable, and the whole procedure then had to be repeated. The reason was that the CD-ROM writing capability of the Easyvision™ workstation is not very stable under most software releases if any other processing is done anywhere else on the Easyvision™ network. In practice, this meant that the CD-ROMs had to be created at night or in the weekends, when the network was relatively idle. For this thesis, about 15 Gigabytes (GB) of MR data were collected using the above methods.

## 7. IMAGE PROCESSING TOOLS

For the image processing programs the reader is referred to the website associated with this thesis at "<http://www.isi.uu.nl/people/michael>." The software (including sources) and documentation including manuals that I have written and that are related to this thesis are available there. Before using them, please observe the copyright and disclaimer notices below or on the website. All programs are in Java and will thus run without modification on any computer system that has browser capabilities. All can be downloaded free of charge, while some of them are available as applets and so do not need to be downloaded.

- ◆ FlowJ, a 2-D optical flow estimation and flow visualization package. FlowJ contains the implementations of four optical flow algorithms: Lucas and Kanade, Uras, Fleet and Jepson and Singh. It also implements four different flow field visualization methods: hedgehog, dynamic color mapping (described in this thesis), spotnoise, and dynamic color spotnoise (described in this thesis). The FlowJ interface and implementation was tested in collaboration with more than 500 users.

- ◆ Flow3J, a package for 3-D optical flow estimation and visualization. Flow3J implements the 3-D optical flow estimation algorithm and the scintillation rendering algorithm developed in Chapter 5.
- ◆ VolumeJ, a volume rendering package that I developed in my spare time. Written in Java, it is fully object-oriented and so allows polymorphic rendering of any object that has a classification and an interpolation method: scalar volumes, but also vector volumes. Two examples of polymorphic rendering that are available are the rendering of red, green, blue (RGB) color volumes (as obtained, for example, by confocal color microscopy imaging systems), and also of 3-D flow fields used in Flow3J (see above). It has been interfaced to ImageJ, the Java image processing program written developed by Wayne Rasband at the United States National Institutes of Health and available at <http://rsb.info.nih.gov/ij>, and can read, manage and write DICOM 3.0 (also the Philips and Siemens dialects) image formats. The VolumeJ interface and capabilities were developed and tested in collaboration with over 3000 users.

#### *Disclaimer*

The software described above and any extensions or alterations are provided "as is" and without warranty of any kind, express, implied or otherwise, including without limitation, any warranty of merchantability or fitness for a particular purpose. The software is experimental only and has not been designed for, tested or approved for clinical use. Any use of the software is at the user's risk. Any conclusions based on the software or its use are solely the user's. I expressly disclaim any responsibility or liability for any and all adverse medical or legal effects, including personal, bodily, property or business injury, and for damages or loss of any kind whatsoever, resulting directly or indirectly, whether from negligence, intent or otherwise, from any use or disuse of the software, from errors in the software, or from misunderstandings arising from the software itself or its use.

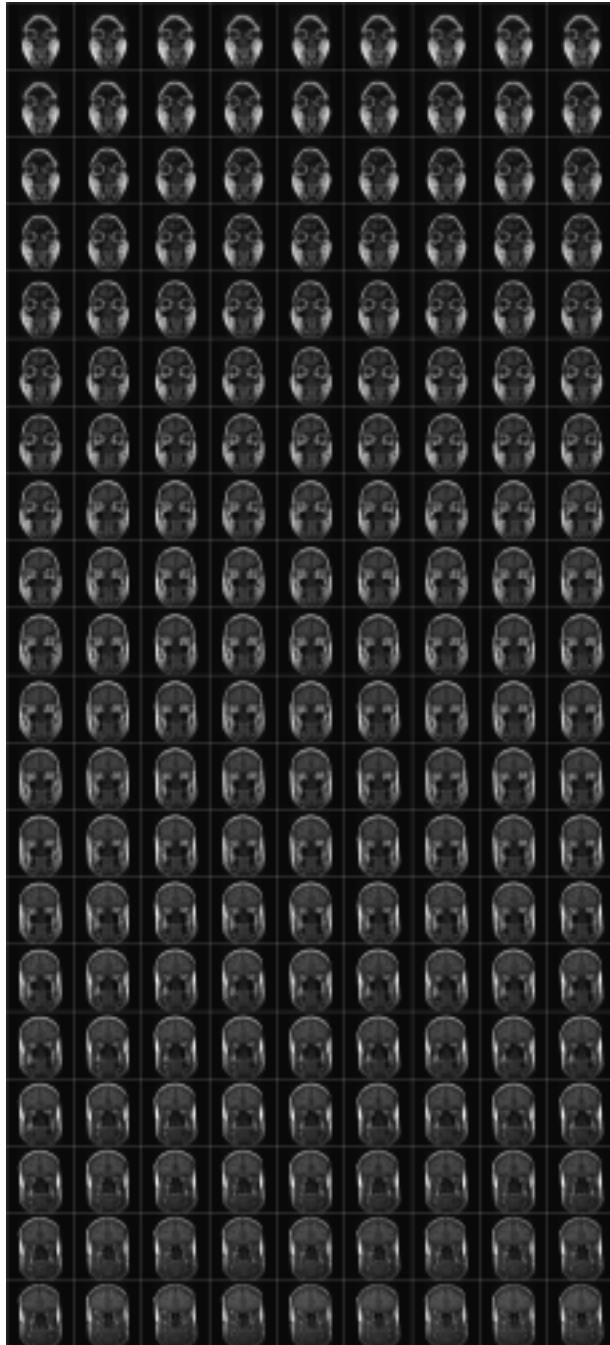


Figure 6. Horizontal gaze cine MR volume sequence of 9 volumes. Across: fixation 1-9 (t-axis). Down: volume frames.



# 4

## Objective quantification of the motion of soft tissues in the orbit

Orbital soft tissue motion analysis aids in the localization and diagnosis of orbital disorders. A technique has been developed to quantify objectively and visualize motion in the orbit during gaze. T1-weighted MR volume sequences are acquired during gaze and soft tissue motion is quantified using optical flow techniques. The flow field is visualized using color-coding: orientation of the flow vector coded by hue and magnitude by saturation of the pixel. Current clinical circumstances limit MR image acquisition to short sequences and short acquisition times. The effect of these limitations on the performance of optical flow computation has been studied for four representative optical flow algorithms: on short (9 frames) and long (21 frames) simulated sequences of rotation of an MR imaged object, on short measured MR sequences of controlled rotation of the same object and on short MR sequences of motion in the orbit. On the short simulated and motion-controlled sequences, the Lucas and Kanade algorithm showed the best performance with respect to both accuracy and robustness. These motion estimates were accurate to within 20%. Motion in the orbit ranged between 0.05 - 0.25 mm/° gaze. Color-coding was found to be attractive as a visualization technique, because it shows both magnitude and orientation of all flow vectors without cluttering.

### 1. INTRODUCTION

Disorders of orbital tissues, such as space-occupying lesions, enucleation (the removal of an eye) with prosthesis implantation, Graves' orbitopathy and trauma all influence the motion of soft tissues in the orbit related to change of gaze [113]. The diagnosis and management of orbital disorders will be improved if the motion of orbital soft tissue can be measured in an objective manner. Orbital tumors may then be localized and differentiated, reducing the need for invasive biopsies; the causes of ocular motility disorders in Graves' orbitopathy and trauma may be clarified; and the motility of the prosthesis and the attachments after enucleation may be better understood.

Recently, cinematic MRI has been introduced to non-invasively assess the motion of tissues in the orbit [4;13]. T1-weighted images are acquired in a stop-

shoot manner at a series of gaze-positions, which yields image sequences that are evaluated by visual inspection of animations. The resulting qualitative judgments are subject to a large intra- and inter-observer variability [4].

In order to determine soft tissue motion in an objective and quantitative manner, we have developed a method that allows quantitative analysis and visual assessment of orbital motion. The starting point is an improved fast cinematic 3D (3-Dimensional) T1-weighted MRI (Magnetic Resonance Imaging) technique, which acquires volume sequences during horizontal and vertical gaze respectively. The two-dimensional motion of soft tissues in these sequences is analyzed by computing the optical flow field [20]. The motion field is visually assessed by means of a color-coded mapping, where the hue of a pixel codes for the orientation and the saturation for the magnitude of the flow vector.

Optical flow algorithms have been shown to give good performance on motion analysis of simulated and natural scenes [19]. For the application at hand, however, several factors are expected to negatively influence the quality of the flow fields. Cinematic MRI requires cooperation from the patient, because he/she needs to actively fixate a sequence of targets for many seconds at close range without blinking. A common reason for patients to undergo cinematic MRI is that they have double vision or other ocular motility disorders, and this makes fixation more difficult. Obviously, increasing the fixation period and the number of targets (the sequence length) improves the MR image sequence quality. In clinical practice, we found that patients get tired during fixation periods exceeding approximately fifteen seconds or after more than approximately nine fixations. It is therefore preferable to acquire short sequences of up to nine frames, and acquire a single frame within fifteen seconds. This sequence length compares unfavorably to the sequences of 15-21 frames used by Barron et al., in their comparative study of optical flow algorithms [19].

Cinematic MR image sequences of motion in the orbit accordingly have relatively low resolution, with aliasing in both space and time. Additionally, intensity, noise and phase of the resonance signal are not isotropic, but are dependent on the orientation of the tissue relative to the gradient of the MR field, because of partial volume effects, RF coil inhomogeneity and susceptibility artifacts. Finally, tissue-motion is not limited to translation or rotation; it also shows dilation, shear and torsion, giving rise to occlusion boundaries. On the other hand, well known confounders of optical flow computation such as transparency, shading and perspective are not present.

The aim of this chapter is to introduce a method to objectively quantify and visualize motion of orbital soft tissue. The main component of the approach is the analysis of the motion field by optical flow techniques. In view of the severe constraints dictated by clinical use on sequence length and image quality, the performance of several representative optical flow algorithms has been studied on long (21 frames) and short (nine frames) simulated sequences of rotation of an MR imaged object, on short and long measured MR sequences of controlled rotation of the same object and on short measured MR sequences of the motion of the human



Figure 1. Setup of the sirloin steak in the rotation device.

orbit. A color-coding technique (dynamical color mapping) is used for visual assessment of orbital soft tissue motion.

## 2. METHODS

### *A) Image acquisition*

Cine MRI time sequences were obtained using the following protocol [146]. Gradient echo T1-weighted volumes were acquired on a 1.5 T MR scanner (Philips NT) using a head-coil (TFE, TE 6.9 ms/TR 12 ms, FOV 180 mm, matrix 256x256x46) with an acquisition time of 15s. The T1 relaxation times were coded as signal intensities and stored in DICOM (Digital Communication in Medicine) 3.0 format as series of separate image volumes. Two-dimensional image sequences were extracted from these volumes on a transversal axis transecting both horizontal rectus muscles and the optic nerve, and on two sagittal axes transecting both vertical rectus muscles. Motion of the head of the patient was restrained by a flexible headband.

### *B) Image sequences*

Because the true motion field in the orbit is unknown, we have used simulations and measurements of controlled motion of an object to compare the computed flow fields with the known motion fields. The lengths of the sequences were chosen to correspond to either the maximum support of the algorithms as reported by Barron et al., i.e., 21 frames (for the Fleet and Jepson algorithm [19]) or to the number of frames that are acquired in clinical practice, i.e., nine frames.

For all experiments, the above acquisition technique was used. Simulated sequences were created by rotating a single image obtained from a sirloin steak sequence (see below) using bilinear interpolation at 5-degree intervals, resulting in sequences of either 21 or nine frames (called *SteakSynth* in this chapter).

For the motion-controlled sequences, a sirloin steak was mounted in a transparent box fitted with an angle ruler (Figure 1). A sirloin steak consists of bands of several millimeters width of alternating muscle and fat tissue that approximates the alternating fat-muscle-fibrous tissue structure of orbital soft tissue. This box was placed in the MR scanner bore, allowing manual rotations with a precision of one degree. The phantom was manually rotated 5 degrees per frame, and a sequence of 21 frames was obtained (called *SteakMR* in this chapter).

For the acquisition of orbital image sequences, the patient fixated on sequential marks placed at 8 degrees intervals on the inside of the scanner bore. Sequences of nine volumes were acquired in horizontal and vertical gaze. From these sequences of nine volumes, nine frames transversally respectively sagittally were extracted on a plane through both rectus muscles [4] (Figure 2).

### C) Pre-filtering

Pre-filtering has been reported to improve the quality of image derivatives [11;19;120;165] for the Lucas and Kanade algorithms. We have looked at:

- ◆ Gaussian smoothing, performed by convolution with a Gaussian kernel in  $2D + \text{time}$  [29], and
- ◆ nonlinear diffusion filtering, as developed by Perona et al. [124], by recursively filtering all images in a sequence using nonlinear diffusion. The parameters for the diffusion equation were set to the values reported in [11] and [124]. This filter favors intra-tissue smoothing by limiting diffusion in regions of high gradient. It has been reported to be superior to Gaussian smoothing for pre-filtering MR image sequences for optical flow computation [11].

## 3. OPTICAL FLOW COMPUTATION

### A) Background

The optical flow field is a vector field that expresses the kinematic relationship between local 2D image (or 3D volume) samples [60]. Optical flow algorithms use the spatio-temporal patterns of image or signal intensity to estimate the optical flow field. In analogy with the mammalian visual system, most optical flow methods follow a two stage system [39;79;107]. In the first stage, possibly analogous to retinal image processing [58], the spatio-temporal patterns in the image sequence structure are decomposed into components or primitives. These may be scaled derivatives, wavelet responses, etc. [20]. Since the optical flow constraint equation (see below) is under-determined, an additional constraint must be introduced.

In the second stage, analogous to post-retinal processing, the resulting system of equations is solved to estimate the actual optical flow [60]. In their comprehensive reviews, Barron and coworkers have classified optical flow algorithms and studied their performance on both synthetic and natural (non-

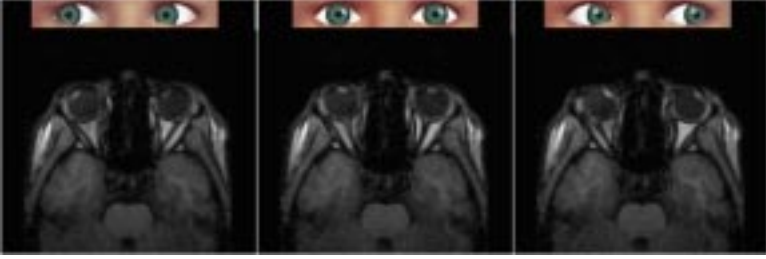


Figure 2. Typical frame of an orbital cine MRI sequence. The corresponding position of the eyes is shown (top).

medical) image series [19;20]. The best performance on natural noisy images was obtained by Fleet and Jepson's phase-based (differential) algorithm [59], Lucas and Kanade's first order differential algorithm [101], and the second-order differential algorithm of Uras and coworkers [153].

The best region-based matching algorithm, proposed by Singh [140], was found to have inferior performance compared to these three methods. Matching algorithms are attractive because they require a temporal support of only two to three frames. In contrast, differential techniques preferably need a larger support of fifteen to twenty-one frames per sequence [19], depending on the exact implementation. For example, the Lucas and Kanade technique requires 15 frames for Gaussian smoothing in  $2D+time$  with a standard deviation of 1.5, if a four order central difference operator is used to obtain the gradients, while the Fleet and Jepson technique requires 21 frames. This need for a large temporal support is one of the reasons the findings of Barron et al., [19] do not necessarily carry over to our application.

### B) Algorithms

The starting point of optical flow computation is the Optical Flow Constraint Equation [60]:

$$dI(\mathbf{x},t)/dt = 0 \quad (2)$$

where  $I(\mathbf{x},t)$  is the (possibly pre-filtered) signal intensity series at pixel  $\mathbf{x}$  and time  $t$ , and  $dI/dt$  the total derivative of  $I$ . This constraint expresses the assumption that structures do not change in signal intensity as they move. The standard deviation of the scale at which  $I(\mathbf{x},t)$  is evaluated by the various algorithms varied between 0.4 and 2.5 in this study. To make the optical flow vector  $\mathbf{v}$  explicit in the two-dimensional case, (2) can be expressed as the gradient constraint equation:

$$\left( \frac{\partial I}{\partial x} + \frac{\partial I}{\partial y} \right) \bullet \mathbf{v} + \frac{\partial I}{\partial t} = 0 \quad (3)$$

This is one equation with two unknowns, the components  $v_x$  and  $v_y$  of the flow vector  $\mathbf{v}$ . To solve (3) for  $\mathbf{v}$ , an additional model needs to be introduced.

We have compared four optical flow algorithms; those by Lucas and Kanade [101], Uras and coworkers [153], Fleet and Jepson [59], and Singh [140]. Because the review by Barron [19] contains extensive derivations of these algorithms, we have not reproduced them here. Instead, the four algorithms are briefly discussed and the various parameter settings and their meaning are listed in Table 1. Except where noted, the parameters were set to the values given in the review by Barron et al.

- ◇ Lucas and Kanade algorithm [101]. If the flow is regular over a small region  $\Omega$ ,  $\mathbf{v}$  in (3) can be linearly approximated by first weighting the local first order derivatives of signal intensity  $I(\mathbf{x},t)$  in  $\Omega$  with a Gaussian and then optimizing the resulting system of equations by least squares minimization. The derivatives are obtained by convolution with either a Gaussian derivative kernel [120], a four-point central difference kernel as in [19] or a  $2D+time$  Sobel kernel [143]. If the central difference kernel or Sobel kernels were used, pre-filtering was performed using Gaussian smoothing or nonlinear diffusion filtering. The Gaussian derivative kernels have been used because these are integrated differentiation/smoothing kernels with a constant basis. The reason we have used the Sobel derivative kernel is that it is a compact kernel with a small temporal support (3 frames), so that less frames are necessary.
- ◇ Uras et al. algorithm [153]. By considering only the second order derivatives of  $I(\mathbf{x},t)$  ( $I_{xx}$  etc.) and ignoring first and all higher order derivatives, an analytical solution can be found for  $\mathbf{v}$  in (3). The image is divided into regions and the most reliable estimate  $\mathbf{v}$  for that region is selected. The derivatives are obtained by convolution with a four-point central difference kernel as in [19].
- ◇ Fleet and Jepson algorithm [59]. This is not an optical flow algorithm in the strict sense since it defines optical flow in terms of phase characteristics instead of intensity characteristics. The optical flow is estimated from the phase characteristics of the output  $R$  of a convolution of the image sequence  $I(\mathbf{x},t)$  with complex-valued  $2D+time$  Gabor wavelets [58].  $R$  is then deconvoluted to decompose the image sequence into component velocities according to scale, magnitude and phase. An over-determined system of equations is formed by constraining the frequency variation and amplitude of these components. A linear regularity constraint is placed on this system, to estimate  $\mathbf{v}$  by least squares minimization. Because the implementation by Barron et al. [19] contains many additional constraints on the system of components, we have followed their implementation closely.

- ◆ Singh and coworkers algorithm [140]. This algorithm is not a true optical flow algorithm either because it computes  $\mathbf{v}$  as the shift of pixel regions. In the first step, velocities are estimated by minimizing a distance measure, the sum of squared differences. The central part of the resulting matrix is then centered around its minimum and converted into a probability distribution. The subpixel velocities  $\mathbf{v}_c$  are then computed from the mean of this distribution. We have again followed the implementation by Barron et al., closely.

The algorithms were implemented as classes in the Java language. A package with

Parameter	Algorithm(s)	Value(s)	Meaning
$\lambda$	Nonlinear diffusion	1	Nonlinearity of diffusion process
$i$	Nonlinear diffusion	10	Number of recursions
$K$	Nonlinear diffusion	2.0	Diffusion coefficient
$\sigma_s$	Lucas and Kanade, Uras	1.5	Spatial scale of Gaussian smoothing/derivatives
$\sigma_t$	Lucas and Kanade, Uras	0.5 – 1.5	Temporal scale of Gaussian smoothing/derivatives
$\sigma_w$	Lucas and Kanade	1.0	Spatial scale of Gaussian regularization kernel
$\tau$	Lucas and Kanade	1.0	Reliability threshold (floor of eigenvalues)
$\omega$	Uras	1, 2 or 8 pixels	Size of regularization region
$\tau$	Uras	0 or 1	Reliability threshold (floor of largest eigenvalue)
$\sigma_s$	Fleet and Jepson	0.83, 1.5 or 2.0	Spatial scale of Gabor filter envelope
$\sigma_t$	Fleet and Jepson	0.83 (9 frames) 2.0 (21 frames)	Temporal scale of Gabor filter envelope
$\tau$	Fleet and Jepson	2.5	Combined frequency/amplitude threshold
<i>resid</i>	Fleet and Jepson	< 0.5 (21 frames) < 2.0 (9 frames)	Residual error of LSE for optical flow vector
<i>maxamp</i>	Fleet and Jepson	0.02 (21 frames) 0.05 (9 frames)	Minimum Gabor filter response amplitude
$N$	Singh	4 pixels	Maximum displacement per frame
$\sigma$	Singh	1.5	Standard deviation for difference of Gaussians
$\tau$	Singh	1.0 – 10.0	Reliability threshold for step 1
$n$	Singh	2	Step 1 window size (2n+1)
$w$	Singh	1 or 2	Step 2 window size (2w+1)
$i$	Singh	10	Step 2 number of iterations

Table 1. Summary of parameters and values used. For details, refer to [19].

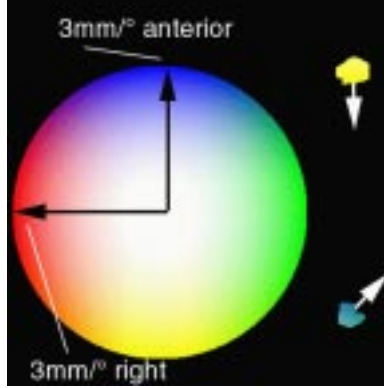


Figure 3. (left) Color space of dynamic color mapping and (right) two moving blobs with optical flow magnitudes of 1 pixel/frame in the direction indicated by their respective arrows.

these implementations is available at “<http://www.isi.uu.nl/people/michael.>”

#### 4. PERFORMANCE AND ACCURACY MEASUREMENT

The true motion field  $\mathbf{v}_{ref}$  is known for the simulated and motion controlled sequences. Following Barron et al. [19], the estimated optical flow vector  $\mathbf{v}$  will be compared with this gold standard through an angular error measure:

$$\psi = \arccos(\mathbf{v}_{ref} \cdot \mathbf{v}) \quad (4)$$

where  $\psi$  denotes angular error (reported in  $^\circ$ ) and  $\mathbf{v}_{ref}$  the true motion. This error measure combines errors in both orientation and magnitude in a single number.

We define the density as the number of reliable flow vectors divided by the total number of pixels in an image. Reliable flow vectors are the estimates that are above the threshold  $\tau$  (see Table 1). Densities are shown for pixels where the magnitude of the true flow vector ranges from zero to three pixels per frame, because motion in the orbit is not expected to exceed this range and flow was found not to be reliable out of this range.

For the true orbit sequences,  $\mathbf{v}_{ref}$  is not known which prevents a quantitative evaluation. Performance was evaluated by qualitative comparison of the dynamic color mappings of the computed flow fields of orbital MR sequences.

#### 5. DYNAMIC COLOR MAPPING

The computed flow fields are displayed using a mapping technique displaying all flow vectors as colored pixels over the original MR frame [7]. Thus, a multi-modality image is obtained that combines functional (motion) and anatomical information in a single image. We have chosen to use a color mapping instead of a quiver or feather format to avoid visual clutter where flow information is dense.

Hue and Saturation of the HSV (Hue, Saturation, and Value) [29;61] space are used to code the orientation and magnitude of the flow vector, respectively. The main axes of orientation are thus represented by complementary color pairs: blue-yellow for anterior-posterior ( $90^\circ - 270^\circ$ ) and green-red for right-left ( $0^\circ - 180^\circ$ ).

Orientations that are not on these axes are represented by mixings of hues. Because higher magnitudes are coded by more intense colors, flow-vectors with higher velocities are easier to discriminate, while lower velocities will show pastel colors. A similar technique to display 3D gravitational fields was described by Hall [74]. The resulting mapping is as follows:

$$p(s) = \left[ \begin{array}{l} 1 - \frac{\|\mathbf{v}\|^{k_m}}{\rho} \left\{ \begin{array}{l} 0, \text{ if } 0 \leq \mathbf{v}_\alpha < \frac{\pi}{2} \\ \frac{1 - \sin(2\mathbf{v}_\alpha)}{2}, \text{ if } \frac{\pi}{2} \leq \mathbf{v}_\alpha < \pi \\ \frac{3 + \cos(2\mathbf{v}_\alpha)}{4} c_y, \text{ if } \pi \leq \mathbf{v}_\alpha < \frac{3\pi}{2} \\ \frac{1 - \cos(2\mathbf{v}_\alpha)}{4} c_y, \text{ if } \frac{3\pi}{2} \leq \mathbf{v}_\alpha < 2\pi \end{array} \right. \\ \\ 1 - \frac{\|\mathbf{v}\|^{k_m}}{\rho} \left\{ \begin{array}{l} \frac{1 - \sin(2\mathbf{v}_\alpha)}{2}, \text{ if } 0 \leq \mathbf{v}_\alpha < \frac{\pi}{2} \\ 0, \text{ if } \frac{\pi}{2} \leq \mathbf{v}_\alpha < \pi \\ \frac{1 - \cos(2\mathbf{v}_\alpha)}{4} c_y, \text{ if } \pi \leq \mathbf{v}_\alpha < \frac{3\pi}{2} \\ \frac{3 + \cos(2\mathbf{v}_\alpha)}{4} c_y, \text{ if } \frac{3\pi}{2} \leq \mathbf{v}_\alpha < 2\pi \end{array} \right. \\ \\ 1 - \frac{\|\mathbf{v}\|^{k_m}}{\rho} \left\{ \begin{array}{l} \frac{1 - \cos(2\mathbf{v}_\alpha)}{4}, \text{ if } 0 \leq \mathbf{v}_\alpha < \pi \\ 0, \text{ if } \pi \leq \mathbf{v}_\alpha < 2\pi \end{array} \right. \end{array} \right]$$

(5)

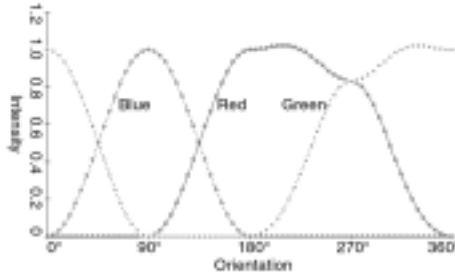


Figure 4 Relation of the orientation of the flow vector  $\mathbf{v}_\alpha$  to the red, green and blue components of the pixel  $p(s)$ . Note that the total brightness (red + green + blue) around  $270^\circ$  is higher than 1.0, to avoid mapping those orientations to brown instead of yellow.

with

$\|\mathbf{v}\| = \sqrt{v_x^2 + v_y^2}$  the magnitude of flow vector  $\mathbf{v}$

$k_m$  = a constant that influences saturation

$\mathbf{v}_\alpha = \arcsin\left(\frac{v_y}{\|\mathbf{v}\|}\right)$ , the angular orientation of  $\mathbf{v}$

$\rho$  the maximum displayable magnitude of  $\mathbf{v}$

$c_y = 1 + \frac{1 - \cos(2\mathbf{v}_\alpha)}{3}$  a 'yellow correction' factor

$p(s) = [\text{red}(s), \text{green}(s), \text{blue}(s)]^T$  the RGB values of the pixel at  $s$ .

Figure 3a presents an example of a mapping of the corresponding color space for all velocities with  $\|\mathbf{v}\|$  in  $\{0 \dots \rho\}$  and  $\mathbf{v}_\alpha$  in  $\{0^\circ \dots 360^\circ\}$ , and an example of two moving blobs that shows how both magnitude and orientation are coded by a single color. The relation between  $\mathbf{v}_\alpha$  and RGB-values is shown in Figure 4. In this study,  $k_m$  was 1.0 (linear mapping), and  $\rho$  was 3.0 pixels/frame except where indicated. The original MR signal intensity gray-value image is shown if the flow vector is zero or unreliable.

## 6. EXPERIMENTAL RESULTS

This section reports on the quantitative performance of the different techniques and shows the flow fields obtained in color-coded images as described above.

The error estimates and densities given in the text and the tables apply to the sequences measured: other sequences gave similar results. Processing times for the different algorithms in pixels/second are shown in Table 2. These timings were

<i>pixels (frames)</i>	<i>SteakSynth 150x150 (&lt; 21 frames)</i>	<i>SteakMR 150x150 (9 frames)</i>	<i>OrbitMR 256x256 (9 frames)</i>
Lucas and Kanade	8.9k	7.6k	6.7k
Uras et al.	6.4k	5.6k	5.8k
Singh	61	59	58
Fleet and Jepson	54	36	72

Table 2. Summary of typical processing times (*pixels/s*) using JDK 1.1.8 and Celeron 400MHz processor.

obtained under the Sun Java Runtime Environment 1.3 (<http://www.sun.com>), on a PC with a 400MHz Celeron processor.

#### A) Simulated sequences

We have tested the four techniques on the simulated sequences, with lengths of both 21 and 9 frames. Table 3 summarizes the main results of the four techniques for the long simulated sequence of 21 frames. Figure 5a-d shows the correspondence between true and estimated magnitudes (up to 4.0 pixels/frame), as a function of flow magnitude in the form of densities for the different techniques. A diagonal distribution would be obtained in case of optimal correspondence.

	<i>n</i>	<i>Average <math>\psi</math></i>	<i>Standard Dev</i>	<i>Density</i>
Lucas and Kanade (CD4P, $\sigma=1.5$ , $\tau=1$ )	15	10.4°	8.6°	55.0%
Lucas and Kanade (CD4P, $\sigma=1.5$ , $\tau=5$ )	15	8.7°	5.6°	21.4%
Lucas and Kanade (non-linear diff, CD4P, $\tau=5$ )	15	11.4°	8.5°	12.1%
Lucas and Kanade (Sobel, $\sigma=1.5$ , $\tau=5$ )	13	9.3°	7.0°	36.2%
Lucas and Kanade (Gaussian differentiation, $\sigma=1.5$ , $\tau=1$ )	13	8.4°	5.3°	20.6%
Lucas and Kanade (Gaussian differentiation, $\sigma=1.5$ , $\tau=5$ )	13	8.4°	5.1°	16.4%
Uras ( $\sigma=1.5$ , $\tau=1$ , $\omega=2$ )	15	19.1°	17.1°	31.2%
Uras ( $\sigma=1.5$ , $\tau=1$ , $\omega=8$ )	15	20.9°	15.8°	30.3%
Uras ( $\sigma=1.5$ , $\tau=0$ , $\omega=2$ )	15	29.6°	28.6°	100.0%
Uras (non-linear diff, $\tau=1$ , $\omega=2$ )	15	38.3°	31.5°	62.2%
Fleet and Jepson ( $\sigma=2.0$ , $\tau=2.5$ , resid < 0.5)	21	7.8°	10.0°	49.9%
Singh (step1 only, n=2, N=4, t=0)	3	26.1°	33.4°	70.8%
Singh (n=2, w=2, N=4, t=6.8)	3	29.4°	36.4°	66.9%

Table 3. Summary of results for long simulated sequences *SteakSynth*. *n* = number of frames for support.

	$n$	Average $\psi$	Standard Dev	Density
Lucas and Kanade (CD4P, $\sigma_s=1.5$ , $\sigma_t=0.83$ , $\tau=1$ )	9	11.9°	9.4°	61.1%
Lucas and Kanade (CD4P, $\sigma_s=1.5$ , $\sigma_t=0.3$ , $\tau=1$ )	7	19.8°	14.4°	66.2%
Lucas and Kanade (Sobel, $\sigma_s=1.5$ , $\sigma_t=1.1$ , $\tau=1$ )	9	9.9°	7.1°	40.3%
Lucas and Kanade (Sobel, $\sigma_s=1.5$ , $\sigma_t=0.83$ , $\tau=1$ )	7	10.5°	7.7°	42.9%
Lucas and Kanade (Gaussian differentiation, $\sigma_s=1.5$ , $\sigma_t=1.1$ , $\tau=1$ )	7	9.7°	6.1°	22.9%
Uras et al. ( $\sigma_s=1.5$ , $\sigma_t=0.83$ , $\tau=1$ , $\omega=2$ )	9	19.4°	18.0°	39.6%
Fleet and Jepson ( $\sigma=0.83$ , $\tau=2.5$ , resid < 2.0, maxamp 0.02)	9	59.3°	13.2°	76.7%
Fleet and Jepson ( $\sigma_s=2.0$ , $\sigma_t=0.83$ , $\tau=2.5$ , resid < 0.5, maxamp 0.05)	9	12.1°	13.6°	19.3%
Singh (step1, $n=2$ , $N=4$ , $t=0$ )	3	26.1°	33.4°	70.8%

Table 4. Summary of results for short simulated sequences *SteakSynth*.  $n$  = number of frames for support.

The Lucas and Kanade algorithm often under-estimates magnitudes (5a), although estimated magnitudes are quite accurate up to 3.0 pixels/frame. Uras (5b) shows clustering of magnitudes around specific values because of the regularization. The Fleet and Jepson algorithm is closest to the diagonal optimum for these simulated sequences (5c). It is clear from (5d) that the Singh algorithm has problems with subpixel velocities, so that estimates are clustered around specific magnitudes.

The true flow field and the four flow fields with the best performance on this sequence for each algorithm are shown in Figure 6b-f. The Lucas and Kanade algorithm performs well, with a good density, as shown in Figure 6c. There was little influence (for *these* sequences) of the type of derivative computation on performance (central difference  $8.7^\circ \pm 5.6^\circ$ , Sobel  $9.3^\circ \pm 7.0^\circ$  and Gaussian  $8.6^\circ \pm 5.6^\circ$ , see Table 3).

$\psi$  is much lower if the threshold  $\tau$  is increased, which reveals the trade-off between accuracy and density. Non-linear diffusion pre-filtering *decreased* performance (to  $11.4^\circ \pm 8.5^\circ$ ) at lower densities. The performance of the Uras algorithm was inferior to that of the Lucas and Kanade algorithm. A region size of  $\omega=2$  gave the best performance. Increasing the regularization region did not noticeably influence performance, but resulted in a lower spatial resolution of the flow field (Figure 6d). Non-linear diffusion filtering decreased performance (from  $19.1^\circ \pm 17.1^\circ$  to  $38.3^\circ \pm 31.5^\circ$ , see Table 3) for this algorithm, but the density increased. The Fleet and Jepson algorithm had the best performance on these long sequences with  $\psi$  slightly smaller than the Lucas and Kanade algorithm, and higher densities (Figure 6e). The Singh algorithm had the worst performance (Figure 6f). We were unable to substantially improve performance for this

	$n$	Average $\psi$	Standard Dev	Density
Lucas and Kanade (CD4P, $\sigma_s=1.5$ , $\sigma_i=0.83$ , $\tau=1$ )	9	16.7°	13.5°	59.7%
Lucas and Kanade (CD4P, $\sigma_s=1.5$ , $\sigma_i=0.4$ , $\tau=1$ )	7	22.3°	17.5°	38.5%
Lucas and Kanade (non-linear diff, CD4P, $\tau=5$ )	9	26.8°	21.2°	57.2%
Lucas and Kanade (Sobel, $\sigma_s=1.5$ , $\sigma_i=0.9$ , $\tau=1$ )	7	14.6°	10.8°	41.3%
Lucas and Kanade (Gaussian differentiation, $\sigma_s=1.5$ , $\sigma_i=1.2$ , $\tau=1$ )	7	15.7°	12.3°	24.7%
Lucas and Kanade (Gaussian differentiation, $\sigma_s=1.5$ , $\sigma_i=1.2$ , $\tau=5$ )	7	12.9°	7.9°	19.1%
Uras ( $\sigma_s=1.5$ , $\sigma_i=0.83$ , $\tau=1$ , $\omega=2$ )	9	27.6°	26.2°	43.1%
Uras ( $\sigma_s=1.5$ , $\sigma_i=0.4$ , $\tau=1$ , $\omega=2$ )	9	58.7°	41.4°	38.0%
Uras (non-linear diff, $\tau=1$ , $\omega=2$ )	9	27.7°	25.6°	43.1%
Fleet and Jepson ( $\sigma=0.83$ , $\tau=2.5$ , resid < 2.0, maxamp 0.02)	9	79.9°	47.4°	32.7%
Fleet and Jepson ( $\sigma_s=2.0$ , $\sigma_i=0.83$ , $\tau=2.5$ , resid < 0.5, maxamp 0.05)	9	41.2°	30.3°	3.4%
Singh (step1, $n=2$ , $N=4$ , $t=0$ )	3	67.8°	44.1°	95.7%

Table 5. Summary of results for (short) motion controlled *SteakMR* sequence.  $n$  = number of frames for support.

algorithm by changing the threshold  $\tau$ ,  $w$  or  $N$ . The second stage was of no help in improving  $\psi$ .

The optical flow constraint equation (2) assumes that the denominators of the derivatives  $\partial t, \partial x$  and  $\partial y$  have the same order of magnitude. Flow magnitudes larger than one pixel/frame may threaten this assumption. We have tested whether this assumption still holds at flow magnitudes up to three pixels per frame. Both decreasing  $\partial t$  by a factor of 3 (by inserting 2 intermediate subframes between frames) and increasing  $\partial x$  and  $\partial y$  by a factor of 3 (by scaling the frames) did not appreciably influence performance of the algorithms on the 21 frame simulated sequences.

Table 4 summarizes the results on the short simulated sequences of nine frames for true flow vector magnitudes up to three pixels per frame. The Lucas and Kanade and the Uras algorithms are robust in the face of a lower temporal support and show only slightly decreased performance. Gaussian derivatives again gave a small advantage ( $9.7^\circ \pm 6.1^\circ$ ) over other types of derivative computation (as expected).

Non-linear diffusion filtering did not have an impact on these results. The Fleet and Jepson algorithm now shows inferior performance and density compared to the previous two algorithms, and is more sensitive at shorter sequence lengths. This is related to pushing the temporal frequency of the Gabor wavelet envelope close to its Nyquist frequency. Relaxing the constraints on the normal components

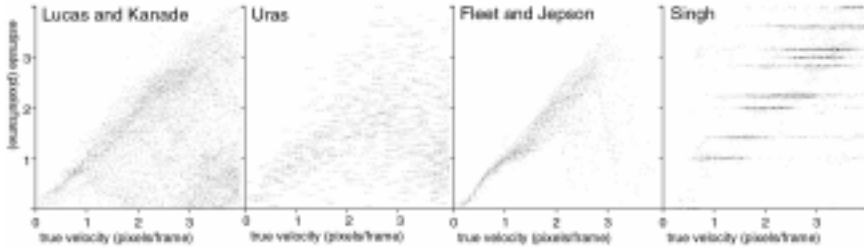


Figure 5. Relationship between true velocities (horizontal axis) versus estimates (vertical axes) for a simulated sequence *SteakSynth* 21 frames. a: Lucas and Kanade ( $\sigma=1.5$ ,  $\tau=1.5$ ,  $\sigma_w=1.0$ ); b: Uras ( $\sigma=1.5$ ,  $\tau=1.5$ ,  $\omega=2$ ); c: Fleet and Jepson ( $\sigma=2$ ,  $\tau=2.5$ , *residuals* < 0.5); d: Singh (step 1 only,  $n=2$ ,  $w=2$ ,  $N=4$ ,  $\tau=6.8$ ).

did not improve performance. The Singh algorithm has a temporal support of only three frames, and therefore performance is unchanged in comparison to sequences of 21 frames.

### B) Motion controlled sequences

Table 5 summarizes the main results of the four techniques on the motion-controlled sequences with a length of nine frames for true flow vector magnitudes up to three pixels per frame.

The true flow field and the four flow fields with the best performance for each algorithm are shown as color-coded images in Figure 7. The Lucas and Kanade algorithm (7a) again had the optimum performance here, with reasonable accuracy and relatively high densities. The best results were obtained if the derivatives were computed using Gaussian derivative kernels ( $12.9^\circ \pm 7.9^\circ$ ). Computation of the derivatives using the  $2D+time$  Sobel kernel ( $14.6^\circ \pm 10.8^\circ$ ) and especially the four-point central difference kernel ( $16.7^\circ \pm 13.5^\circ$ ) gave results that were not as good.

The Gaussian derivative and Sobel derivative kernels needed only *seven* frames (instead of the nine that were available) to obtain this performance (increasing the scale so that nine frames were used did not improve performance).

The performance of the Uras algorithm (7b) was not as good, which can be attributed to the higher sensitivity of second order derivatives to noise and aliasing present in measured MR sequences. Performance was again slightly worse with non-linear diffusion filtering than with Gaussian pre-filtering.

The Fleet and Jepson algorithm (7c) is not robust. This is due to the sensitivity to noise and the variability of phase to different orientations of the tissue to the MR gradient field. This lack of robustness is not solely due to the shorter sequence length since performance was much better on the simulated sequences of nine frames. The decreased performance of the Singh technique (7d) must be related to non-isotropic MR noise. Non-linear diffusion filtering did not improve performance for this algorithm.

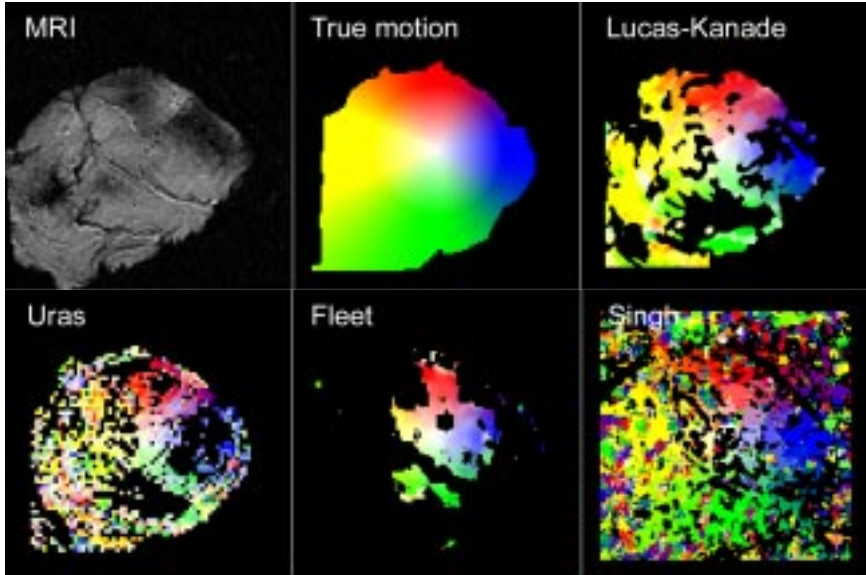


Figure 6. a: simulated and motion controlled sequences central frame; b: true flow field; c-f: estimated flow fields for simulated sequence of 21 frames; c: Lucas and Kanade ( $\sigma=1.5$ ,  $\tau=1.0$ ,  $\sigma_n=0.8$ ); d: Uras ( $\sigma=1.5$ ,  $\tau=1.0$ ,  $\omega=2$ ); e: Fleet and Jepson ( $\sigma=2$ ,  $\tau=2.5$ ,  $residuals < 0.5$ ); f: Singh (step 1 only,  $n=2$ ,  $w=2$ ,  $N=4$ ,  $\tau=6.8$ ).

### C) Real orbit sequences

The true flow field in the orbit is not known for real orbit sequences, so the performance of the different techniques cannot be measured objectively. Therefore, we show the flow fields of the human orbit estimated by each technique in Figure 8.

The various parameters have been set to values that gave optimum performance on the simulated and phantom sequences. The images are as seen from below, i.e. left is right, and top is front. The subject was gazing from right to left in the horizontal plane, and the flow is measured in the  $0^\circ$  position (gaze straight ahead).  $\rho = 3\text{pixels/frame}$ , which means that a fully saturated pixel is moving 0.26 mm for every degree change in angle of gaze. All velocities given are approximations averaged over the specific tissue. The Lucas and Kanade algorithm gives the best flow fields (8a), with the Uras technique (with  $\omega=2$ ) a close second (8b). Larger  $\omega$  are useless for our purposes, as is shown in Figure 7c, a flow field estimated at  $\omega=8$ . The fields obtained with the Fleet and Jepson and Singh algorithms are practically useless. The flow fields shown have been estimated with parameters set to relax the constraints for these algorithms: with the parameters set

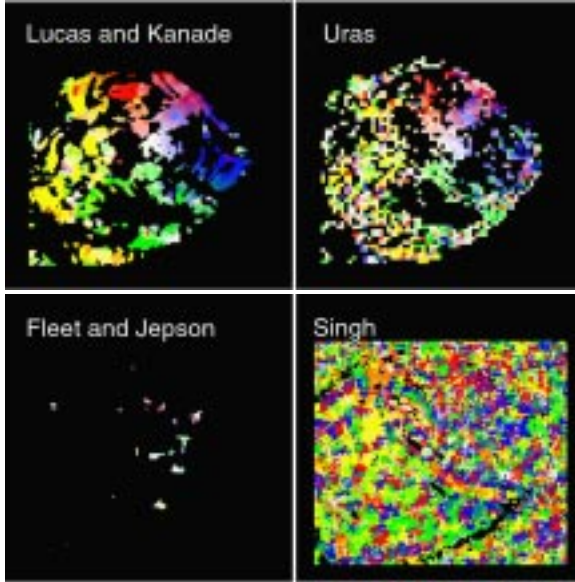


Figure 7. Estimated flow fields for motion controlled sequence of 9 frames; a: Lucas and Kanade ( $\sigma_s=1.5$ ,  $\sigma_r=0.83$ ,  $\tau=1.0$ ,  $\sigma_w=1.0$ ); b: Uras ( $\sigma_s=1.5$ ,  $\sigma_r=0.83$ ,  $\tau=1.0$ ,  $\omega=2$ ); c: Fleet and Jepson ( $\sigma_s=2.0$ ,  $\sigma_r=0.83$ ,  $\tau=2.5$ , *residuals* < 1.0); d: Singh (step 1 only,  $n=2$ ,  $w=2$ ,  $N=4$ ,  $\tau=6.8$ ).

as in the review by Barron and coworkers [19], no flow vectors could be estimated for both algorithms.

The following discussion of the content of the flow field concerns Figure 8a and 8b only. The lens moves to the right (green,  $0.25\text{mm}/^\circ$ ), the medial rectus muscle of the right eye which is relaxing moves forward (yellow,  $0.15\text{mm}/^\circ$ ) and the insertion of the lateral rectus muscle of the right eye which is contracting moves backward (blue,  $0.12\text{mm}/^\circ$ ), while the muscle itself is moving posterior and to the left (purple).

The optic nerve of the right eye is dragged by the eyeball and moves to the left (red,  $0.14\text{mm}/^\circ$ ). Its anterior portion has the largest motion (most saturated red,  $0.18\text{mm}/^\circ$ ). Similar motion can be seen in the left orbit. Because the subject follows his gaze by slightly turning his head, some flow is estimated in the rest of the head ( $< 0.05\text{mm}/^\circ$ ). The orbital fat just back of the eyeball has a very intricate motion, and is following the optic nerve in some regions (reddish), while in other regions it is moving anteriorly or posteriorly. This is probably related to its three-dimensional expansion and contraction. Around the junction of the optic nerve to the eyeball, where adjacent pixels move in three different directions, the smoothness constraint imposed on the regional velocity field limits resolution of such flows.

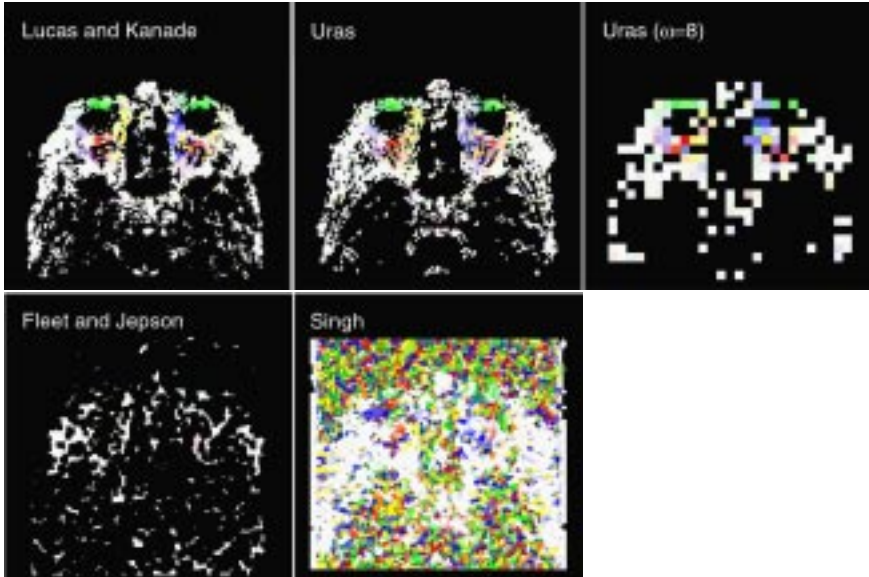


Figure 8. Estimated flow fields for real orbit *OrbitMR* sequence of 9 frames; a: Lucas and Kanada ( $\sigma_s=1.5$ ,  $\sigma_t=0.83$ ,  $\tau=1.0$ ,  $\sigma_w=1.0$ ); b: Uras ( $\sigma_s=1.5$ ,  $\sigma_t=0.83$ ,  $\tau=1.0$ ,  $\omega=2$ ); c: Uras ( $\sigma_s=1.5$ ,  $\sigma_t=0.83$ ,  $\tau=1.0$ ,  $\omega=8$ ); d: Fleet and Jepson ( $\sigma_s=2.0$ ,  $\sigma_t=0.83$ ,  $\tau=10$ , *residuals* < 5.0); e: Singh (step 1 only,  $n=2$ ,  $w=2$ ,  $N=4$ ,  $\tau=8.0$ ).

## 7. DISCUSSION

In order to quantify orbital soft tissue motion in an objective manner, this chapter compares the performance of several optical flow algorithms on T1 weighted MRI sequences of the orbit. Owing to the clinical constraints, these sequences are typically short, noisy and aliased. The algorithms evaluated are the differential algorithms by Lucas and Kanade [101], Uras et al. [153] and Fleet and Jepson [59], and the regional matching algorithm by Singh [140]. The algorithms have been tested on long (21 frames) and short (nine frames) simulated sequences of rotation of an MR imaged object, on short measured MR sequences of controlled rotation of the same object and on short MR sequences of the human orbit. Dynamic color mapping, a color-coding mapping algorithm, was introduced to display the flow fields by mapping the (two-dimensional) flow vectors to the color of a single pixel. Our results indicate that:

- ◆ The Lucas and Kanade algorithm is more robust in the face of sequence length and MR anisotropy, especially if Gaussian derivatives are used. Motion can be estimated in measured MR sequences of seven frames with an angular error of less than  $13^\circ$ . On short sequences, and long MR sequences the algorithm's density and accuracy are better than that of the Fleet and Jepson algorithm, contrary to the results in [19]. Only on the long simulated sequences did the Fleet and Jepson algorithm show the best performance. The performance of the Uras algorithm was inferior to the Lucas and Kanade algorithm. Zientara et al. [165] have combined the estimates of the Uras and the Lucas and Kanade algorithms to improve the flow field estimation. We see no use for this, as the average error of the Uras algorithm is everywhere higher than that of the Lucas and Kanade algorithm. While the Singh algorithm is theoretically attractive because it has a temporal support of only three frames, its performance was disappointing due to its sensitivity to noise and partial volume effects, even at displacements larger than 1 pixel/frame. As far as processing time is concerned, the Lucas and Kanade and Uras algorithms were on average a factor of 100 faster for a 256x256 pixel format than both the Fleet and Jepson and the Singh algorithms. We found non-linear diffusion filtering not to be useful to improve the performance of any of these four algorithms for our purposes.
- ◆ Dynamic color mapping shows all flow vectors without cluttering, in contrast to the hedgehog, quiver and arrow methods in common use. It is possible to evaluate the full flow field, and this has been of help for our purposes in making a qualitative assessment of flow field quality if the true flow field is not known.
- ◆ Using a combination of cinematic MRI and optical flow computation, the motion of soft tissue in the orbit can be predicted to within an angular error of  $13^\circ$  in sequences of seven frames, corresponding to an error in orientation and magnitude substantially below 20%. The true optical flow field in the orbit is - as stated previously - unknown, and was in fact the inspiration for the technique described in this article. Hence, the objective quantification by optical flow computation can only be validated by clinical use, but our results validate the choice of techniques, at the very least [7].
- ◆ Soft tissue motion in the orbit ranges between 0.0 to 0.25 mm/ $^\circ$  of gaze change, depending on the type of tissue and the position of the tissue relative to the globe. Occlusion effects due to shear are difficult to detect using any of these four algorithms and are a subject of future research.

## 8. ACKNOWLEDGMENT

We are grateful to the anonymous reviewers for their valuable comments to earlier versions of this chapter and to Wilbur Bartels for the use of his MR rotation device. The first author is currently supported by a grant from the *dr. F.P. Fischer Stichting*.

# 5

## Computation and visualization of three-dimensional soft tissue motion in the orbit

Presented in part at the annual meeting of the Association for Research in Vision and Ophthalmology, Fort Lauderdale, Florida, May 2000.

This chapter presents a method to measure the soft tissue motion in 3-D in the orbit during gaze. It has been shown that 2-D quantification of soft tissue motion in the orbit is effective in the study of orbital anatomy and motion disorders [3]. However, soft tissue motion is a three-dimensional phenomenon, and part of the kinematics is lost in any two-dimensional measurement. Therefore, T1-weighted MR volume sequences are acquired during gaze, and soft tissue motion is quantified using a generalization of the Lucas and Kanade optical flow algorithm to 3-D. New techniques have been developed for visualizing the 3-D flow field as a series of color-texture mapped 2-D slices or as a combination of volume rendering for display of the anatomy and scintillation rendering for the display of the motion field. We have studied the performance of the algorithm on (4-D) volume sequences of synthetic motion, simulated motion of a static object imaged by MR, an MR imaged rotating object, and MR imaged motion in the human orbit during gaze. The accuracy of the analysis is sufficient to characterize motion in the orbit, and scintillation rendering is an effective visualization technique for 3-D motion in the orbit.

### 1. INTRODUCTION

It has been shown that the objective measurement of the motion of orbital soft tissue can improve the diagnosis and management of orbital disorders, and may shed new light on the kinematics of orbital tissue [3;7]. In these studies, a technique was introduced that uses cinematic MRI and optical flow computation of the motion field. This technique was limited to two dimensions. However, any technique based on two-dimensional (2-D) optical flow computation can only estimate the motion projected in the imaging plane. Since soft tissue motion and

deformation is intrinsically three-dimensional (3-D) in nature, 3-D quantification may be beneficial. Problems for which 3-D quantification may be useful include the measurement of intraconal fat kinematics [96], measurement of muscle kinematics [41] and elucidation of the effect of muscle pulleys [113].

This study introduces a method to measure quantitatively and visualize 3-D motion and deformation. The method is based upon fast cinematic (cine) 3-D volumetric T1-weighted Magnetic resonance imaging (MRI) in which hypervolumes (time series of volumes) are acquired during horizontal and vertical gaze. The three-dimensional motion present in the hypervolume is then analyzed with a 3-D optical flow algorithm. The algorithm is a 3-D generalization of the 2-D Lucas and Kanade optical flow algorithm, that was found to have the best performance on MR images [3]. A motion-to-color mapping was shown to be effective to visualize a 2-D-motion field in a small space [3], and this approach has been extended to create colored-textures that reflect the magnitude and orientation of the flow field in 3-D space. Other approaches to measure the motion in 3-D cine MRI sequences have been described, such as Cine Phase Contrast (PC) MR [134] and MR-tagging [164]. Cine PC MRI utilizes the phase changes of the MR signals due to tissue motion [15;52;123]. It can only determine relatively regular and large motion fields, and is less attractive to determine small-scale non-translational motion, as in this application. Human heart motion has also been successfully estimated with MR-tagging. The grid formed by such tags is sparse in comparison to the size of the orbit and only a few tags would cover the orbital tissues allowing only rough estimates of motion. These methods thus seem less attractive to measure motion in the orbit.

A limitation to the proposed method is that cine MRI requires active cooperation from the patient. Since the main reason to undergo cine MRI is double vision or another ocular motility disorder, the number of MR acquisitions and the time allowed for them is necessarily severely constrained. This limits both the resolution of the volume and the number of volumes that can be acquired per motion sequence.

The purpose of this chapter is to quantify 3-D motion and deformation of soft tissues in the orbit objectively. To this end, 3-D optical flow computation and 3-D motion visualization are introduced as techniques to analyze and present the measurement results. In view of the constraints outlined above, a side objective of the study is to establish whether the optical flow fields thus obtained are of sufficient quality to be clinically useful.

## 2. METHODS

### *A) MR volume acquisition*

Cinematic MRI (3-D+time) hypervolumes were obtained using the following protocol. Gradient echo T1-weighted volumes were acquired on a 1.5 T MR scanner (Philips NT) using a head-coil with the following settings: Turbo Field Echo, Echo Time (TE) 4.598 ms, Repetition Time (TR) 9.36 ms, flip angle 20



Figure 1. Single slices from single volumes of the three objects imaged for this chapter. a. Single slice from single volume from *Cube* hypervolume ( $60 \times 60 \times 60 \times 25$ ). b. Single slice from *SteakMR* hypervolume ( $256 \times 256 \times 40 \times 25$ , central portion shown). c. Single slice from *OrbitMR* hypervolume ( $256 \times 256 \times 23 \times 9$ ). d. Slice from *OrbitMR* Volume of Interest selected for motion estimations ( $180 \times 50 \times 23 \times 9$ ).

degrees, matrix  $256 \times 256 \times 40$ , resulting in a voxel size of  $0.8 \times 0.8 \times 2.0$ mm and an acquisition time of 15s per single volume for a single fixation position. The T1 relaxation times were coded as signal intensities and the hypervolumes stored in DICOM 3.0 format as series of separate consecutive images.

### B) Simulated, measured hypervolumes

Since the true 3-D motion field in the orbit is unknown, simulations and MR measurements of controlled motion of an object were used to compare the flow field estimates with known motion fields. Simulated sequences were created by translating (at different velocities) a cube in 3-D space, and obtaining  $60 \times 60 \times 60 \times 25$  hypervolumes of the resulting motion sequence. We chose one of these for this study, called *Cube*.

Motion-controlled MR measured hypervolumes were obtained by rotating a sirloin steak in a transparent box fitted with an angle ruler as in [3] in the MR scanner bore. The phantom was manually rotated 5 degrees per frame, and  $256 \times 256 \times 40 \times 25$  hypervolumes of the resulting motion sequence were obtained. We chose one of these for this study, called *SteakMR*.

In addition, a single MR volume of the sirloin steak was synthetically rotated 5 degrees per frame using (tri-)linear interpolation, resulting in a  $256 \times 256 \times 40 \times 9$  hypervolume of the resulting synthetic rotation sequence. We chose one of these for this study, called *SteakSynth*.

In the orbit, soft tissues undergo both rigid motion and (non-rigid) deformation. However, it is very difficult to evaluate experiments with deformation. This is because the deformation field cannot be objectively measured so as to provide the gold standard for the optical flow estimates. Therefore, we have synthetically simulated the three-dimensional deformation of a single MR volume of the sirloin steak, which resulted in a sequence called *SteakDeform*. The deformation simulated the impression of a rigid body (a ball of 3.0mm) into the top of the steak, with the bottom of the steak being held fixed against a rigid plane over its entire width and being unrestrained at the sides. The ball impressed with 1.2mm/frame. Tri-linear interpolation was used.

True orbital soft tissue motion hypervolumes were obtained by having a healthy subject fixate on sequential marks placed at 8 degrees intervals along horizontal and vertical lines on the inside of the scanner bore. Each hypervolume thus acquired consists of a sequence of volumes (256x256x23x9) of the resulting horizontal and vertical gaze motion sequences, and each volume corresponds to a single gaze position. Three subjects were studied and we chose one of these sequences, called *OrbitMR*.

Single slices of a single volume of each of the sequences are shown in Figure 1.

### 3. OPTICAL FLOW COMPUTATION

#### A) Background

The optical flow field is a vector field that expresses the kinematic relationship between local 2-D or 3-D image samples [60]. Optical flow algorithms use the spatio-temporal patterns of these image or signal intensity samples to estimate the motion field. Optical flow computation has been used by several researchers for 2-D motion studies of MR sequences [11;47;51;165]. The Lucas and Kanade first order differential algorithm is the most robust estimator of 2-D motion in MR sequences [3]. The starting point of optical flow computation is the Optical Flow Constraint Equation [60;78]:

$$dI(\mathbf{x},t)/dt = 0 \quad (1)$$

where  $I(\mathbf{x},t)$  is the (possibly pre-filtered) signal intensity series at location  $\mathbf{x}$  and time  $t$ , and  $dI/dt$  the total derivative of  $I$ . (1) expresses the assumption that structures do not change in signal intensity as they move. To make the optical flow vector  $\mathbf{v}$  explicit in the three-dimensional case, (1) can be expressed in terms of first order partial derivatives as:

$$\nabla I(\mathbf{x},t) \cdot \mathbf{v} + I_t(\mathbf{x},t) = 0 \quad (2)$$

with  $\nabla I(\mathbf{x},t)$  the gradient of  $I$ , and  $I_t(\mathbf{x},t) = \frac{\partial I(\mathbf{x},t)}{\partial t}$ , the partial derivative of  $I(\mathbf{x},t)$

with respect to time. This is one equation with three unknowns, the components  $v_x$ ,  $v_y$ , and  $v_z$  of the 3-D flow vector  $\mathbf{v}$ . Thus, this equation defines a plane for the normal component of the 3-D velocity vector. To solve (2) for  $\mathbf{v}$ , two additional constraints need to be introduced.

#### B) 3-D Optical flow algorithm

Lucas and Kanade over-constrained the 2-D version of (2) by assuming the flow to be regular over a small neighborhood. The 2-D motion vector can then be estimated by linear optimization from the over-constrained system of equations. By weighting the equations for this neighborhood with a Gaussian, the influence of neighboring (normal) flow vectors on the estimate is increased relative to that of

vectors that are more distant. By generalizing this approach to three dimensions, the 3-D motion vector  $\mathbf{v}$  is estimated from a system of equations (each of the form of (2)) for the neighborhood  $\Omega$  :

$$\mathbf{A}\mathbf{V} = \mathbf{b} \quad (3)$$

where, for  $\mathbf{x}_i = I \dots m$ ,  $\mathbf{x}_i \in \Omega$ ,

$$\mathbf{A} = \begin{bmatrix} I_x(\mathbf{x}_1, t) & I_y(\mathbf{x}_1, t) & I_z(\mathbf{x}_1, t) \\ I_x(\mathbf{x}_2, t) & I_y(\mathbf{x}_2, t) & I_z(\mathbf{x}_2, t) \\ \vdots & \vdots & \vdots \\ I_x(\mathbf{x}_m, t) & I_y(\mathbf{x}_m, t) & I_z(\mathbf{x}_m, t) \end{bmatrix}$$

$$\mathbf{V} = \begin{bmatrix} v_x \\ v_y \\ v_z \end{bmatrix}$$

$$\mathbf{b} = -[I_t(\mathbf{x}_1, t), \dots, I_t(\mathbf{x}_m, t)]^T$$

The system is weighted on both sides with a 3-D Gaussian  $W$  with standard deviation (of the associated probability function)  $\sigma_w$ :

$$\mathbf{W}\mathbf{A}\mathbf{V} = \mathbf{W}\mathbf{b} \quad (4)$$

where, for  $\mathbf{x}_i = I \dots m$ ,  $\mathbf{x}_i \in \Omega$ ,

$$\mathbf{W} = \text{diag}\{W(\mathbf{x}_1), W(\mathbf{x}_2) \dots W(\mathbf{x}_m)\}$$

The optimum solution for  $\mathbf{V}$  in (4), in a least squares sense, is obtained using the pseudoinverse [29]:

$$\mathbf{V} = [\mathbf{W}\mathbf{A}]^\dagger \mathbf{W}\mathbf{b} \quad (5)$$

where

$$[\mathbf{W}\mathbf{A}]^\dagger = \text{pseudoinverse of } [\mathbf{W}\mathbf{A}].$$

Provided  $|\left[ \mathbf{A}^T \mathbf{W}\mathbf{A} \right]| \neq 0$ , the pseudoinverse is identical to the least-squares inverse  $[\mathbf{A}^T \mathbf{W}\mathbf{A}]^{-1} \mathbf{A}^T$ . It can be found efficiently in closed form:

$$\mathbf{A}^T \mathbf{W}\mathbf{A} = \begin{bmatrix} \sum_{\mathbf{x} \in \Omega} W(\mathbf{x}) I_x^2 & \sum_{\mathbf{x} \in \Omega} W(\mathbf{x}) I_x I_y & \sum_{\mathbf{x} \in \Omega} W(\mathbf{x}) I_x I_z \\ \sum_{\mathbf{x} \in \Omega} W(\mathbf{x}) I_x I_y & \sum_{\mathbf{x} \in \Omega} W(\mathbf{x}) I_y^2 & \sum_{\mathbf{x} \in \Omega} W(\mathbf{x}) I_y I_z \\ \sum_{\mathbf{x} \in \Omega} W(\mathbf{x}) I_x I_z & \sum_{\mathbf{x} \in \Omega} W(\mathbf{x}) I_y I_z & \sum_{\mathbf{x} \in \Omega} W(\mathbf{x}) I_z^2 \end{bmatrix} \quad (6)$$

with  $I_x=I_x(\mathbf{x},t)$  etc., so that

$$\mathbf{A}^T \mathbf{W} \mathbf{b} = \begin{bmatrix} \sum_{\mathbf{x} \in \Omega} W(\mathbf{x}) I_x I_x I_x \\ \sum_{\mathbf{x} \in \Omega} W(\mathbf{x}) I_y I_y I_y \\ \sum_{\mathbf{x} \in \Omega} W(\mathbf{x}) I_z I_z I_z \end{bmatrix} \quad (7)$$

and

$$\left[ \mathbf{A}^T \mathbf{W} \mathbf{A} \right]^{-1} = \begin{bmatrix} \frac{\Xi_{yy} \Xi_{zz} - \Xi_{yz}^2}{\left[ \mathbf{A}^T \mathbf{W} \mathbf{A} \right]} & \frac{\Xi_{xz} \Xi_{yz} - \Xi_{xy} \Xi_{zz}}{\left[ \mathbf{A}^T \mathbf{W} \mathbf{A} \right]} & \frac{\Xi_{xy} \Xi_{yz} - \Xi_{xz} \Xi_{yy}}{\left[ \mathbf{A}^T \mathbf{W} \mathbf{A} \right]} \\ \frac{\Xi_{xz} \Xi_{yz} - \Xi_{xy} \Xi_{zz}}{\left[ \mathbf{A}^T \mathbf{W} \mathbf{A} \right]} & \frac{\Xi_{xx} \Xi_{zz} - \Xi_{xz}^2}{\left[ \mathbf{A}^T \mathbf{W} \mathbf{A} \right]} & \frac{\Xi_{xy} \Xi_{xz} - \Xi_{xx} \Xi_{yz}}{\left[ \mathbf{A}^T \mathbf{W} \mathbf{A} \right]} \\ \frac{\Xi_{xy} \Xi_{yz} - \Xi_{xz} \Xi_{yy}}{\left[ \mathbf{A}^T \mathbf{W} \mathbf{A} \right]} & \frac{\Xi_{xy} \Xi_{xz} - \Xi_{xx} \Xi_{yz}}{\left[ \mathbf{A}^T \mathbf{W} \mathbf{A} \right]} & \frac{\Xi_{xx} \Xi_{yy} - \Xi_{xy}^2}{\left[ \mathbf{A}^T \mathbf{W} \mathbf{A} \right]} \end{bmatrix} \quad (8)$$

with  $\Xi_{xy} = \sum_{\mathbf{x} \in \Omega} \{W(\mathbf{x}) I_x(\mathbf{x},t) I_y(\mathbf{x},t)\}$ , so that  $\mathbf{V}$  can be evaluated analytically. This

is important for an acceptable performance, since otherwise  $\left[ \mathbf{A}^T \mathbf{W} \mathbf{A} \right]^{-1} \mathbf{A}^T$  would have to be computed iteratively.

In the discrete case, the partial derivatives of  $I$ ,  $I_i$ , where  $i \in \{x, y, z\}$ , are of dimension  $length^{-1}$ , so that the derivative products of the matrix in (6) have dimension  $length^{-2}$ . The eigenvalues  $\lambda_1$ ,  $\lambda_2$  and  $\lambda_3$ , with  $\lambda_1 > \lambda_2 > \lambda_3$ , of (6) form a metric for the regularity of the (gradients in the) neighborhood  $\Omega$  and are used as a reliability index as in [19]. If  $\lambda_3$  is larger than a threshold  $\tau$  (of dimension  $length^{-2}$ ), the flow in  $\Omega$  is assumed to be regular in 3-D, and  $\mathbf{v}$  is assumed to be reliable. If  $\lambda_2$  is larger than  $\tau$ , but not  $\lambda_3$ , the flow in  $\Omega$  is assumed to be regular in two dimensions only, and the normal of  $\mathbf{v}$  is obtained by projecting the result of (5) onto the eigenvector associated with  $\lambda_1$  (the largest eigenvalue).

Many structures in the orbit do not have a 3-D texture, but a predominantly 2-D texture, such as blood vessels and nerves. If strict 3-D regularity is imposed on the motion of these structures, the normal of  $\mathbf{v}$  cannot be used to give an indication of the motion.

### C) Derivative computation

The quality of the optical flow field computed by the above method depends on the accuracy of the partial derivatives  $\frac{\partial I}{\partial x}$ ,  $\frac{\partial I}{\partial y}$ ,  $\frac{\partial I}{\partial z}$  and  $\frac{\partial I}{\partial t}$  in (2), which are obtained from the (discrete) motion sequences [19]. As mentioned above, due to the clinical constraints, the hypervolumes that contain the 3-D MRI motion sequences are aliased both spatially and temporally. In [3] we have examined the 2-D performance of three forms of derivative computation, using central difference kernels, Sobel 2-D+time derivative kernels and Gaussian derivatives. In that study, Gaussian derivatives [120] were found to have the best performance. The continuous form of the Gaussian derivative kernel is given by:

$$G(x) = e^{-\frac{x^2}{2\sigma^2}} \text{ and } G'(r) = -\frac{1}{\sigma^2} r e^{-\frac{x^2}{2\sigma^2}} \quad (9)$$

The temporal and spatial components of the scale  $\sigma$  of the Gaussian and its derivative in (9) were separated as  $\sigma_t$  and  $\sigma_s$  respectively, because the number of volumes  $n$  in the sequence is low (typically nine). It is important to understand that the main constraint in this application is the clinical limit on  $n$ . It might therefore seem attractive to compute the derivatives using a 4-point central difference kernel or a 4-D Sobel kernel (Table 1), since if no pre-smoothing is used,  $n = 5$  respectively  $n = 3$ , are sufficient for these differentiation kernels. Indeed, these two are often used in the literature on 2-D optical flow computation, see for example [19]. However, in the 2-D case, their performance without prefiltering was found to be very low as a consequence of aliasing [3]. Performance might be improved by pre-smoothing with a Gaussian, but the temporal scale  $\sigma_t$  of the smoothing kernel is then limited by  $n$  in the manner explained above. At a given sequence length  $n$ , the maximum of the temporal scale  $\sigma_t$  for a specific Gaussian derivative kernel (if the derivatives are computed using Gaussian derivatives) or Gaussian smoothing kernel (if they are computed using 4-point central difference or Sobel operators) is limited to  $\sigma_{t,\max}$ :

$$\begin{aligned} \sigma_{t,\max}(\text{Gauss}) &= \frac{n-1}{6} \\ \sigma_{t,\max}(\text{Sobel}) &= \frac{n-3}{6} \\ \sigma_{t,\max}(\text{CD}) &= \frac{n-5}{6} \end{aligned} \quad (10)$$

i.e., if  $n = 9$ ,  $\sigma_{t,\max}(\text{Gauss}) = 1.33\dots$ ,  $\sigma_{t,\max}(\text{Sobel}) = 1$  and  $\sigma_{t,\max}(\text{CD}) = 0.66\dots$  We have looked at the effect of the scale  $\sigma_t$  (at given  $n$ ) on the performance of the optical flow algorithm with Gaussian derivatives, and also compared the performance of the three derivative operators described above at given  $n$ , with  $\sigma_{t,\max}$  computed as in (10).

The 4-D Sobel kernel is given in Table 1. The algorithms were implemented in the Java language. A package with these implementations is available at “<http://www.isi.uu.nl/people/michael>.” (please observe copyright and disclaimer statements).

#### 4. PERFORMANCE AND ACCURACY MEASUREMENTS

The true 3-D motion field  $\mathbf{v}_{ref}$  is known for the simulated and motion controlled sequences. The estimated 3-D motion vector  $\mathbf{v}$  is compared to  $\mathbf{v}_{ref}$  through an angular error measure, by a trivial generalization of the error formula of Barron et al. [19]:

$$\psi = \arccos(\hat{\mathbf{v}}_{ref} \cdot \hat{\mathbf{v}}) \quad (11)$$

where  $\psi$  denotes angular error, the difference in angle between correct and measured flow vectors (reported in degrees),  $\hat{\cdot}$  denotes normalization, and  $\mathbf{v}_{ref}$  the true motion. This measure combines errors in orientation and magnitude in a single number. We define the density as the number of reliable (i.e. if the smallest eigenvector is larger than a threshold  $\tau$ ) flow vectors divided by the total number of voxels in an image.

#### 5. 3-D MOTION VISUALIZATION

##### A) Background

In order to interpret the three-dimensional optical flow fields in relation to the anatomy of the orbit, it is helpful to display the flow fields combined with a contour surface of the underlying soft tissue anatomy.

		z-1			z			z+1		
		x-1	x	x+1	x-1	x	x+1	x-1	x	x+1
t-1	y-1	-2	0	2	-3	0	3	-2	0	2
	y	-3	0	3	-6	0	6	-3	0	3
	y+1	-2	0	2	-3	0	3	-2	0	2
t	y-1	-6	0	6	-9	0	9	-6	0	6
	y	-9	0	9	-18	0	18	-9	0	9
	y+1	-6	0	6	-9	0	9	-6	0	6
t+1	y-1	-2	0	-3	-3	0	3	-2	0	2
	y	-3	0	3	-6	0	6	-3	0	3
	y+1	-2	0	2	-3	0	3	-2	0	2

Table 1. 4-D ‘Sobel’ differentiation kernel.

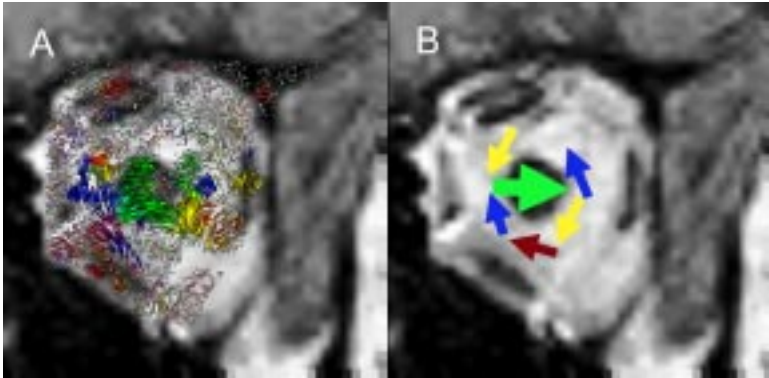


Figure 2. 2-D section visualization. Shown is the motion of the intraconal tissue around the optic nerve in the apex of the orbit. (left) A: flow field displayed over static MRI of the left orbit (coronal view). (right) B: schematic view of motion as explanation of A. The colors of the arrows in B are made to correspond to the spotnoise colors of the motion vectors in A. The green arrow indicates the motion of the optic nerve (the front of the eye is gazing in the opposite direction), while the tissue in front of the optic nerve is moving out of its way, and the tissue behind the optic nerve fills in the gap left behind. See Figure 8 for the parameters.

We have used two methods: a stack of 2-D sections of the 3-D flow field laid over the anatomy also shown as a 2-D stack, and a 3-D volume rendering of the flow field combined with a rendering of the static anatomy volume. Visualization of 3-D flow phenomena, as opposed to scalar volumes, is difficult and tends to produce complex images with heavily overlapping geometry [109]. Occlusion and depth ambiguities strain viewers' abilities to interpret the motion data. For example, arrow plots are generally not useful for three-dimensional flow, since depth perception of one-dimensional objects (the arrows) is poor compared to surface objects, and populating three-space with arrows easily produces overloaded images. In addition, most approaches assume that the flow field is locally regular and dense [17]. A visualization method was developed to display the 3-D flow field of the motion of orbital tissues, and still allow the relation to the underlying anatomy to be seen.

### *B) 2-D Section visualization*

We have previously found that color classification of 2-D motion vectors is effective in presenting the motion field in a compact manner, with both orientation and magnitude of the flow vector displayed in a single pixel [3]. However, color classification can sometimes make it difficult to see the orientation of the flow. Spot noise [161] allows the visualization of regular and dense flow fields using textures formed of random noise oriented along the orientation of the flow vector. With this technique, the noisiness of the texture makes it difficult to show the magnitude of the flow vector. By coloring the local texture using our classification

scheme, the advantages of both of these techniques are combined. The texture is formed by displaying two-dimensional elliptical Gaussians that are oriented in the direction of the flow vector. The pixel intensities of the texture are multiplied with the color resulting from classification of the magnitude of the flow vector at that pixel. Thus, both the orientation of the collective motion of a tissue, and the orientation and magnitude of the motion of each individual pixel are visualized. See Figure 2.

### C) 3-D Volume visualization

Particle visualization is a method whereby vectors are projected onto the image as small blurred ellipses oriented along the (projected) direction of motion [161]. We have adapted that method to show the flow field as a thinly transparent texture of colored particles that we have called *scintillations*. These are then projected over a surface rendering of the anatomical static 3-D MRI volume [17;98]. Thus, the collective motion of a region of soft tissue can be appreciated as a texture, and the individual motion vectors are still discernible.

The visualization proceeds as follows. While the static MRI volume is being rendered (involving voxel interpolation, gradient interpolation, opacity, shading and viewplane compositing computations [98;99] at all relevant volume locations), the interpolated 3-D flow vector corresponding with each volume location is also inspected. Only a jittered (i.e. pseudo-random on a grid) subset of vectors in the flow field is visualized to avoid cluttering. If a flow vector is reliable (see above) and to be visualized, the voxel at that location is not rendered. Instead, a scintillation  $\xi$  is projected onto the viewplane. A scintillation is a small, colored, elongated, oriented half-ovoid Gaussian with parameters  $\xi_c$ , its color,  $\xi_s$ , its shape and  $\xi_o$ , its opacity.

The color  $\xi_c$  of the scintillation is determined by classification of the 3-D motion vector according to a 3-D generalization of the scheme adopted in [3]: the color is cast into HSV (Hue, Saturation and Value) [29] space by coding the magnitude  $|\mathbf{v}|$  of the motion vector into the hue channel and the 2-D orientation (along a specified axis in 3-D) into the saturation channel. Faster motion shows as brighter colors.

The shape  $\xi_s$  of the scintillation is determined by classification of the 3-D motion vector. The length of the half-ovoid is dependent on the magnitude  $|\mathbf{u}|$  of the 2-D projection of the flow vector  $\mathbf{v}$  onto the viewplane. Faster motion thus shows as more elongated scintillations. The elongation effect of the scintillation is determined by a scaling factor  $\sigma_l$ . Only half of the resulting ovoid is shown. As  $|\mathbf{u}|$  approaches zero, the scintillations become round dots, the size of which is determined by the standard deviation of (the associated probability function of) a Gaussian,  $\sigma_l$ . The computation of  $\xi_s$  is as follows:

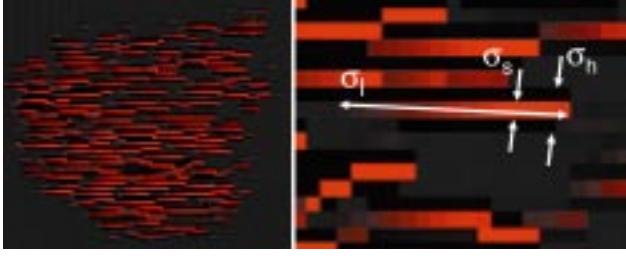


Figure 3. Example of scintillations. (left) a. Texture formed by multiple scintillations. The underlying motion field is a translation to the right (seen from the back) with an average motion of 1.0 voxel/volume (frame). The hue and orientation of the scintillations code for the direction of the flow vector, while the length of the half-ovoid and the saturation of its color code for the magnitude of the flow vector. The background has been made dark-gray and the underlying static object is not shown on purpose. (right) b. Detail of scintillation. Shown are the parameters that define the shape of a scintillation and its halo:  $\sigma_d$ , the size of the short axis of the half-ovoid (here, 0.4),  $\sigma_l$  the scaling factor for the long axis and  $\sigma_h$  the size of the short axis of the halo (here, 0.7).

$$\begin{aligned}
 \mathbf{U}_h &= \mathbf{M}\mathbf{V}_h \\
 \varepsilon_1 &= \mathbf{u}_i p_i - \mathbf{u}_j p_j \\
 \varepsilon_2 &= \mathbf{u}_j p_i + \mathbf{u}_i p_j \\
 \sigma_l &= \sigma_d + \sigma_s |\mathbf{u}| \\
 \xi_{s(p_i, p_j)} &= e^{-\left( \frac{\varepsilon_1^2 + \varepsilon_2^2}{\sigma_s^2 + \sigma_l^2} \right)}, \text{ if } \varepsilon_2 < 0 \\
 \xi_{s(p_i, p_j)} &= 0 \text{ otherwise}
 \end{aligned} \tag{12}$$

where  $\mathbf{M}$  = a 4x4 projection transformation matrix (relating homogeneous voxel coordinates to projection viewplane coordinates),  $\mathbf{V}_h = (\mathbf{v}_x, \mathbf{v}_y, \mathbf{v}_z, 1)^T$ , i.e.  $\mathbf{v}$  in homogeneous coordinates,  $\mathbf{U}_h = (\mathbf{u}_i, \mathbf{u}_j, \mathbf{u}_k, \mathbf{u}_l)^T$  the projection of the motion vector onto the viewplane (in homogeneous coordinates),  $\varepsilon_1$  and  $\varepsilon_2$  the short and long axes of the half-ovoid,  $\xi_s$  = the scintillation shape,  $\mathbf{p} = (p_i, p_j)$  a point in  $\xi_s$ ,  $\mathbf{u} = (\mathbf{u}_i, \mathbf{u}_j)^T$ ,  $\sigma_d$  the standard deviation of a Gaussian determining the minimum length and width of the ovoid, and  $\sigma_l$  a scaling factor determining the effect of  $\mathbf{U}$  on the length of the major axis of  $\xi_s$ .

The opacity  $\xi_o$  defines how transparent the scintillation is. If the flow field is not sparse, depth differences between scintillations need to be accentuated to allow individual scintillations to be discerned [81]. In order to accomplish this effect, an opaque halo is rendered around every scintillation by manipulating the opacity,  $\xi_o$ .  $\xi_o$  is a 2-D Gaussian with a standard deviation  $\sigma_h$  that defines the length of its short axis, with  $\sigma_h > \sigma_s$ :

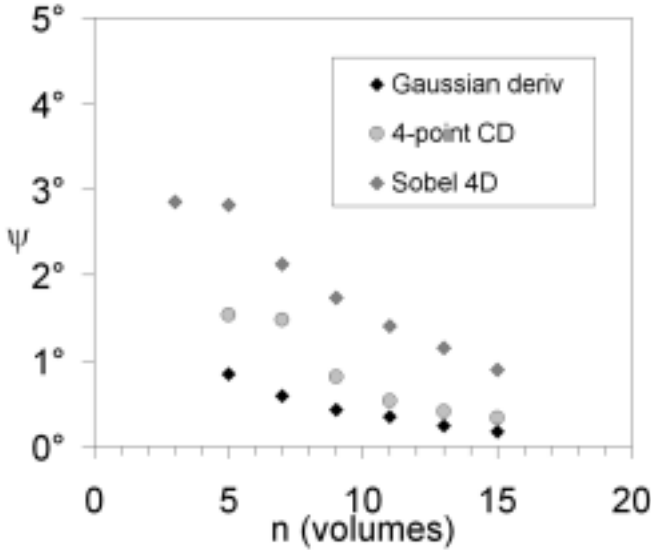


Figure 4. Performance of the 3-D algorithm on *Cube* expressed as angular error  $\psi$  (in degrees) as a function of temporal scale  $\sigma_t$  of either the Gaussian derivatives or Gaussian prefiltering;  $\sigma_r = \sigma_w = 1.2$  and  $\tau = 5$ .

$$\xi_o(p_i, p_j) = \left| \mathbf{v} \right| \left( e^{-\left( \frac{\epsilon_1^2}{\sigma_h^2} + \frac{\epsilon_2^2}{\sigma_l^2} \right)} \right) \quad (13)$$

Thus, a tiny dark opaque halo is created around a scintillation, to make individual vectors discernible [50;90]. The approach is illustrated in Figure 3.

## 6. EXPERIMENTAL RESULTS

This section reports on the quantitative performance of the optical flow algorithm and shows visualizations of the 3-D motion fields obtained. For these experiments, the scale of the neighborhood  $\Omega$ ,  $\sigma_w$ , was set to the spatial scale at which the derivatives were computed or at which Gaussian smoothing was performed, i.e.  $\sigma_w = \sigma_s$ .  $\sigma_s = 1.3$  in all experiments described in this chapter while the voxel dimensions are  $0.8 \times 0.8 \times 2.0$  mm. Therefore, the scale of the neighborhood  $\Omega$  is approximately  $4.8 \times 4.8 \times 12.0$  mm, corresponding to the scale of the moving and deforming structures in the orbit, that ranges from approximately 4-5 mm (optic nerve cross-section) to 40 mm (rectus muscle length) in size in any one dimension.

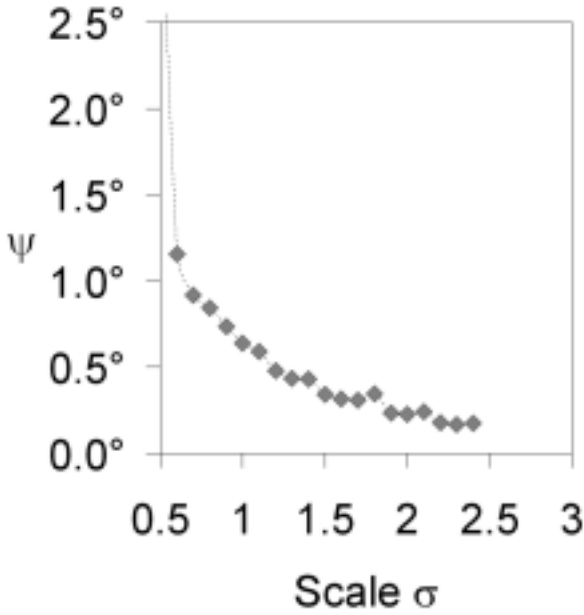


Figure 5. Performance of the 3-D optical flow algorithm expressed as angular error  $\psi$  (in degrees) as a function of the temporal scale  $\sigma$ , of the Gaussian derivatives,  $\tau = 5$ .

#### A) Synthetic sequences

The first experiment was designed to check the reliability of the 3-D optical flow computation and compare its performance to that of the Lucas and Kanade algorithm on the *Square2* sequence (a simulated motion sequence formed of a

	Angular Error $\psi$	Standard Dev	Density
$\tau=0$	10.56°	20.59°	67.86%
$\tau=1$	0.54°	0.27°	8.10%
$\tau=5$	0.48°	0.23°	3.87%

Table 2. Performance on *Cube* using Gaussian derivatives at scale  $\sigma_t=1.3$  (in other words, 9 volumes were needed in the sequence) at different thresholds  $\tau$ . In all experiments,  $\sigma_s=\sigma_w=1.3$ .

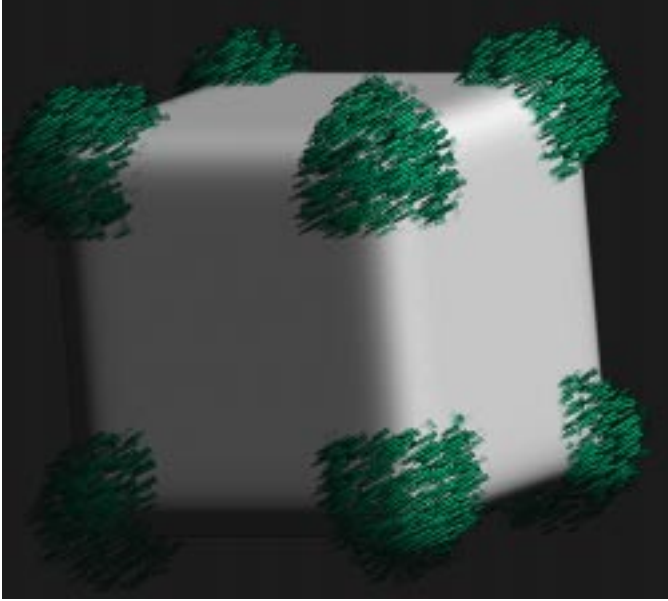


Figure 6. Scintillation rendering of the 3-D flow field of *Cube* combined with a rendering of the cube itself. The cube is translating at  $(1.3, 1.3, 1.3)$  voxels per volume (to the upper-right-back). Motion is visible only at the corners of the cube. Gaussian derivatives,  $\sigma_i=1.3$ ,  $\tau = 5$ .

blurred black square on a white background moving at  $(1.3, 1.3)$  pixels per frame) as found by Barron et al. [19]. The *Cube* sequence was created as the 3-D equivalent of *Square2*, and has a motion of  $(1.33, 1.33, 1.33)$  voxels per volume, i.e. to the upper-right-back. (see Figure 1a for a single slice from a single volume).

Table 2 summarizes the performance of the algorithm on *Cube* using Gaussian derivatives at different thresholds  $\tau$ . The performance is comparable to that of the Lucas and Kanade algorithm on *Square2*: at  $\tau=1$ , the average error was  $0.21^\circ \pm 0.16^\circ$  (at a density of 7.9%) for *Square2* [19], while for *Cube* it is  $0.54^\circ \pm 0.27^\circ$  (at a density of 8.10%).

As discussed above, an important constraint in this application is  $n$ , the number of volumes in a sequence. We have studied the effect of  $n$  on the performance (i.e. angular error  $\psi$ ) of the algorithm with *Cube* and compared the effect of using Gaussian, central difference and Sobel derivative operators (the last two with Gaussian smoothing) at the maximum scale  $\sigma_{max}$  allowed by  $n$  (see Equation (10)), as shown in Figure 4. With *Cube*, Gaussian derivatives for gradient estimation perform superior to the others given  $n$  and have reasonable performance even at  $n = 5$  (when  $\sigma_{max} = 0.66\dots$ ). We have also studied the performance of the algorithm, using Gaussian derivatives, in terms of temporal scale space on the *Cube* sequence.

	<i>SteakSynth</i>			<i>SteakDeform</i>			<i>SteakMR</i>		
	Angular Error $\psi$	Standard Dev	Density	Angular Error $\psi$	Standard Dev	Density	Angular Error $\psi$	Standard Dev	Density
$\tau=0$	7.55°	8.25°	77.92%	4.79°	8.34°	74.79%	18.43°	16.18°	97.00%
$\tau=0.5$							16.02°	11.41°	9.60%
$\tau=1$	4.29°	3.19°	5.03%	1.76°	2.20°	30.05%	12.26°	7.26°	3.45%
$\tau=2.5$							7.13°	3.42°	0.32%
$\tau=5$	3.99°	1.65°	0.09%	1.66°	2.53°	12.09%	3.91°	1.66°	0.01%

Table 3. Performance on *SteakSynth*, *SteakDeform* and *SteakMR* volume sequences with  $n=9$ ; Gaussian derivatives at temporal scale  $\sigma_t=1.3$ , for different thresholds  $\tau$ . Because for *SteakMR* the densities are so low at  $\tau=5$ , results are also given for intermediate values of  $\tau=0.5$  and  $\tau=2.5$ .

See Figure 5. At a temporal scale  $\sigma_t=1.3$ , which corresponds to  $n=9$ , the angular error  $\psi$  is under  $0.5^\circ$ .

Figure 6 shows a visualization of the flow field of *Cube* combined with a rendering of the cube itself. The 3-D motion vectors can be determined only at the corners of the cube. The motion vectors show as blue-green scintillations, and due to their halos, the flow vectors are separable, and also visible as a semi-transparent texture.

### B) MR simulated and measured sequences

It is important to understand that since densities are expressed as a fraction of all voxels, densities of 0.1%-1% are actually not very sparse and still useful for this application.

Table 3 summarizes the main results of the algorithm on the three sequences using Gaussian derivatives at different thresholds  $\tau$ .

The *SteakSynth* hypervolume was obtained by synthetic rotation of the steak volume (obtained by static MRI, Figure 1b), with an angular rotation step of 5 degrees per volume around the z-axis. The decrease in performance compared to the *Cube* hypervolume is probably caused by the fact that the derivatives are more discontinuous due to the aliasing and partial volume effects of the MR acquisition process.

The *SteakDeform* hypervolume was obtained by synthetic non-rigid three-dimensional deformation of the steak volume (obtained by static MRI, Figure 1b) using a simulated rigid ball and supporting plane. The better performance compared to *SteakSynth* is caused by the more regular differences in the magnitude

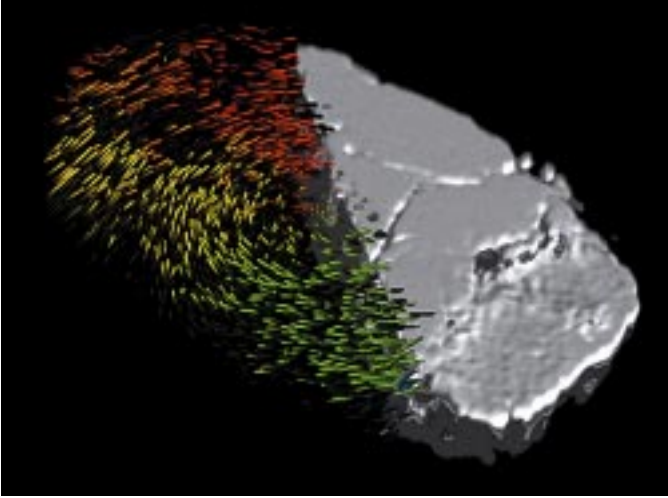


Figure 7. Scintillation rendering of the 3-D motion field of (left) of *SteakMR* combined with a volume rendering of the ‘anatomy’ of the steak (right). The anatomy under the motion field is not shown since the motion field is too dense. The axis of rotation is oriented perpendicular to the surface of the steak. Gaussian derivatives,  $\sigma_i=1.3$ ,  $\tau = 5$ .

of the deformation (over space), compared to the more rapid magnitude differences (over space) of a rotation.

The *SteakMR* hypervolume was obtained by rotating the steak at 5 degrees per volume (around the z-axis) and acquiring an MRI volume at each step. Compared to *SteakSynth*, performance of the algorithm has deteriorated. This is probably caused by aliasing in the temporal dimension caused by partial volume effects and the anisotropic phase effect of the orientation of the tissue relative to the gradient of the MR field. Since the density at  $\tau=5$  is smaller than 0.01%, which is not very useful for our purposes, results are also reported for intermediate thresholds  $\tau=0.5$  and  $\tau=2.5$ .

Figure 7 shows a scintillation rendering of one half of the flow field of *SteakMR* together with the anatomy of the steak for the other half.

### C) MR measured orbital sequences

We have used 3-D optical flow computation to determine the motion as a function of gaze position in hypervolumes of the orbit, *OrbitMR*. Since the true motion field  $\mathbf{v}_{ref}$  is unknown in this case, it is impossible to obtain quantitative data on performance. We found that the obtained 3-D flow fields are similar to those obtained using 2-D optical flow estimation along different planes.

To evaluate the clinical usefulness of 3-D motion estimation, we have tried to measure the 3-D motion of the *intraconal* tissue. The intraconal tissue is the fatty and fibrous tissue located in between the extraocular muscles, around the optic nerve, and is composed of tiny globules of fat suspended between connective

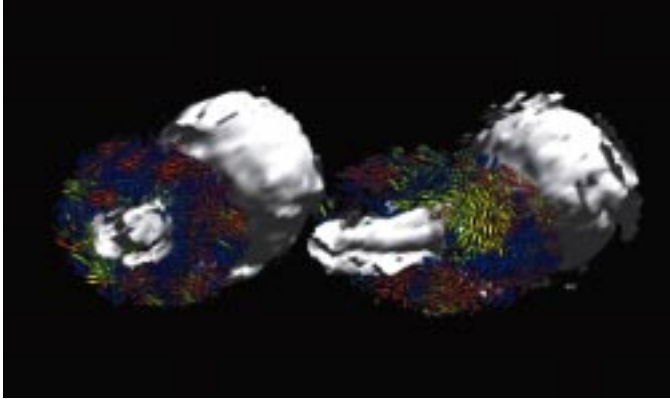


Figure 8. Scintillation rendering of the 3-D motion field of *OrbitMR*, combined with a static rendering of both globes and both optic nerves. Shown as seen from inside the skull looking forward towards globes (right is right). Only the motion field of the intraconal tissue close to the optic nerve is displayed, because it would otherwise be obscured by the motion of the rectus muscles and other tissues. The subject is gazing from left to right, and the optic nerve (at the back of the globe) therefore moves in the opposite direction, to the left. The motion of the intraconal tissue is coupled to that of the optic nerve above and below it (green, i.e. to the left). At the trailing edge of the right optic nerve (right in this Figure) this tissue can be seen to fill the space left by the motion path of the nerve. From the top of the nerve it fills in a *downward* direction (yellow) and from the bottom of the nerve it fills in an *upward* direction (blue). This is best seen around the right nerve. Gaussian derivatives,  $\sigma_i=1.3$ ,  $\tau = 2.5$ .

tissue septa [94]. Since the space within the orbital cavity is fixed, this tissue has to deform when the muscles and the globe move during gaze. The kinematics are unknown, but are relevant since it has recently been proposed that this tissue may form a functional skeleton for the orbital contents [8]. The 3-D motion field of the intraconal tissue was measured in three subjects.

One of the motion fields, with the subject gazing from left to right, is shown in 2-D in Figure 2 and in a scintillation rendering in Figure 9. The intraconal fat can be seen to deform from over and under the optic nerve into the space left by it as it trails the movement of the globe. The intraconal tissue thus fills the vacuum left by the nerve, as behind a spoon moving through syrup. Therefore, it deforms like a liquid and not like a solid (if it deformed like a solid matter such as a sponge, it would have deformed in the same direction as the nerve, filling up the space from sideways instead of from top and bottom).

## 7. DISCUSSION

This chapter introduces a 3-D optical flow algorithm and a 3-D optical flow visualization technique to objectively quantify and visualize the 3-D motion of soft tissues in the orbit from MR volume sequences. In addition, it studies the quality of the motion fields obtained, given the clinical constraints on sequence length and

resolution. The Lucas and Kanade algorithm [101] was generalized to three dimensions, and tested on (4-D) motion sequence hypervolumes of synthetic motion of a stylized object (a cube), of synthetic motion of an MR imaged natural object (a steak), of an MR imaged rotating natural object (the same steak), and of MR imaged motion in the human orbit during gaze. The 3-D motion field was visualized by rendering color-textured 2-D slices with the 2-D motion, and also by scintillation rendering, so as to display the 3-D motion field combined with conventional volume rendering of the underlying (static) anatomy.

Previous approaches to 3-D optical flow estimation have been successful in determining 3-D motion and deformation from 3-D volumetric CT and MR sequences of the human heart [144] and the human brain [72;75]. Human cardiac optical flow computation from CT sequences has been rigorously validated [72]. These approaches are based on 3-D generalizations of Horn and Schunk's algorithm, using a global smoothness constraint on the motion field [78]. Local smoothness constraints, such as Lucas and Kanade's algorithm [19], where the flow is constrained to be regular only in the neighborhood of the point where the optical flow vector is to be determined, were found to give better and more robust performance in 2-D optical flow estimation in both natural scenes [19] and in MR sequences [3].

Our results indicate that 3-D optical flow computation by the algorithm introduced in this study is feasible. Its performance on synthetic 3-D volume sequences is comparable to that obtained by conventional 2-D optical flow measurement algorithms on 2-D sequences. The algorithm is sensitive to the quality of the partial derivatives, and the best performance was reached using Gaussian derivatives. The performance on realistic MR volume sequences is quite acceptable. The derived flow fields are of sufficient quality for clinical purposes. In fact, we have been able to measure the previously unknown kinematics of the intraconal tissue, which was found to deform like a liquid and less like a solid.

The results also show that 3-D optical flow visualization by scintillation rendering, combined with surface rendering of the anatomy, gives an insight into the relation of tissue motion with the underlying anatomy. This allows an evaluation of the quality of the 3-D flow field when the true flow field is not known.

In conclusion, 3-D optical flow computation has sufficient performance to estimate the motion of soft tissues in the orbit for clinical purposes, and scintillation rendering is effective in understanding the relationship between tissue motion and underlying anatomy.

## 8. ACKNOWLEDGMENT

We are grateful to the anonymous reviewers for their valuable comments to earlier versions of this chapter, to Wilbert Bartels for the use of his MR rotation device and to Koen Vincken, PhD for his help in setting up the website. The first author is supported by the *Dr. F.P. Fischer Stichting* and the *Department of Ophthalmology of the Vrije Universiteit Medical Centre*.

# 6

## MRI Dynamic Color Mapping: a new quantitative technique for imaging soft tissue motion in the orbit

Presented in part at the annual meeting of the Association for Research in Vision and Ophthalmology, Fort Lauderdale, Florida, May 1997.

*Purpose:* to investigate both feasibility and clinical potential of magnetic resonance imaging-dynamic color mapping (MRI-DCM) in measuring the motion of soft tissues in the orbit and in the diagnosis of orbital disorders by detecting changes in motion. *Methods:* Sequences of MRI scans were acquired (acquisition time, 5 seconds) in a shoot-stop manner, while the patient fixated at a sequence of 13 gaze positions ( $8^\circ$  intervals). Motion was quantified offline (in mm per degree of gaze change) using an optical flow algorithm. The motion was displayed in a color-coded image in which color saturation of a pixel shows the displacement and the hue the displacement's orientation. Six healthy volunteers and four patients (two with an orbital mass and two with acrylic ball implant after enucleation) were studied. *Results:* the technique was found to be clinically feasible. For a gaze change of  $1^\circ$ , orbital tissues move between 0.0-0.25mm/deg, depending on the type of tissue and location in the orbit. In the patients with an orbital mass, motion of the mass was similar to that of the medial rectus muscle, suggesting disease of muscular origin. In the enucleated orbits, soft tissue motion was decreased. One eye showed attachment of the optic nerve to the implant, which could be verified by biopsy specimen. *Conclusions:* MRI-DCM allows noninvasive and quantitative measurement of soft tissue motion and the changes in motion due to pathologic conditions. In cases in which the diagnosis of a tumor in the apex is in doubt, it may reduce the need for biopsy. In contrast to static computed tomographic (CT) scans and MRIs, it can differentiate between juxtaposition and continuity, and may be a new and promising tool in the differential diagnosis of intraorbital lesions.

### 1. INTRODUCTION

The introduction and refinement of noninvasive imaging techniques such as computed tomographic (CT) scans and magnetic resonance imaging (MRI) have been revolutionary in the differentiation of orbital diseases. However, these

techniques are static and, in a number of cases, leave unanswered questions about the origin of lesions and the relationship between tissues during motion. This relationship, the kinetics of the eye and orbital tissue due to gaze, is highly complex and incompletely understood [64]. Cinematic MRI, and also dynamic CT and dynamic ultrasound, were developed to surmount these limitations and evaluate the motion of tissues in the orbit in relation to gaze changes [13;42]. Cinematic MRI scans and the other two modalities, however, are evaluated by inspection of videos and consequently allow only qualitative judgments that are subject to large intra- and interobserver variability. By measuring motion quantitatively, this may be avoided. In addition, data reduction can be achieved. Clinicians can gain an understanding of orbital motion by inspecting a single image, instead of a video of typically several minutes' duration.

We have developed a new technique, MRI-dynamic color mapping (MRI-DCM) to measure the motion of orbital tissues quantitatively, using cinematic MRI with short acquisition times (5 seconds/image), combined with powerful image processing techniques [11;13;42]. The purpose is to express the motion of orbital soft tissues in millimeters per degree of change in gaze and display these in a color-coded image in which the hue of a pixel is determined by the orientation and its saturation by the length of the underlying motion vector [3;146]. This technique allows the study of motion in relation to gaze changes, but not yet of saccades and pursuit movements, because the temporal resolution of orbital cinematic MRI currently does not allow it.

Disorders of orbital tissues can all influence soft tissue motion: for example, space-occupying lesions, enucleation with prosthesis implantation, Graves' orbitopathy or trauma. Measuring such changes may aid in localizing and differentiating orbital tumors, exploring prosthesis motility and observing tissue attachments in the case of enucleation and trauma. In addition, it is known that in Graves' orbitopathy, motility disturbances are related to muscle tightness and swelling, increased intraorbital pressure and inflammatory changes in muscles and intraorbital fat tissue. After decompression surgery, motility disturbances may either increase or decrease, and surgical management of these disturbances is not as straightforward as in other cases of acquired strabismus. By measuring the motion of orbital tissues, we might be able to understand more fully the causes of motility disorders in Graves' orbitopathy, especially after decompression surgery.

The purpose of the present study was to investigate the feasibility and usefulness of MRI-DCM and to establish the additional value of MRI-DCM in the differential diagnosis of orbital lesions.

## 2. METHODS

All subjects were treated in accordance with the tenets of the Declaration of Helsinki, and informed consent was obtained after the nature of the study had been

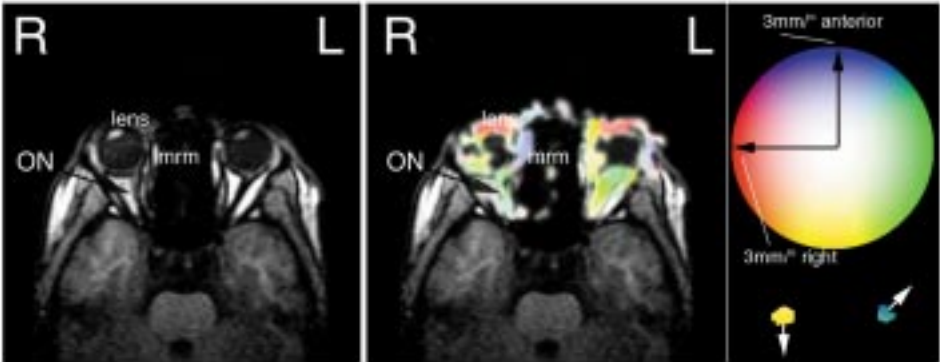


Figure 1. Normal orbital soft tissue motion obtained by MRI-DCM in normal subject 2. 1a. Typical MRI image from the sequence. MRI images are as viewed from below. mrm = medial rectus muscle; ON = optic nerve. 1b. MRI-DCM. The subject gazes from left to right. Wherever the flow is zero or cannot be measured reliably, the original MRI image is visible. 1c. The circle in the upper part serves as an aid to relate a particular color to orientation and motion. The arrowheads on the perimeter of the circle indicate motion of 0.3 mm/deg directed anteriorly and left respectively. At the bottom of 1c., two examples are given of blobs that move in the orientation indicated by the white arrow (posteriorly and left-anteriorly) at 0.3 mm/deg.

explained. The approval of the institutional review board of our hospital was granted for the research protocol and the informed consent form.

Cinematic MRI scans are obtained according to our previous protocol [146]. Images are acquired on a 1.5-T MR scanner (Philips Gyroscan NT, release 4, Eindhoven, the Netherlands), using a head-coil. The scans are angulated to include the optic nerves and the rectus muscles. Transversal and sagittal sequences of gradient echo T1-weighted images (turbo field echo [TFE], echo time [TE] 6.9 ms, recovery time [TR] 12 ms, 4-mm slice thickness, field of view 170 mm, matrix 128 x 128 or 256 x 256, scan-time 5 sec) are acquired in a shoot-stop manner. During acquisition, the patient fixates sequentially on a row of 13 horizontal fixation marks placed at  $8^\circ$  intervals. The sequences are stored in digital imaging and communication (DICOM) format and analyzed using software developed by the first author. The actual gaze angles are corrected for parallax taking into account interpupillary distance and distance of lateral orbital rim to the fixation marks.

After prefiltering with a Gaussian spatiotemporal filter, the image sequences are quantified. The motion estimates are obtained by the optical flow algorithm that was first introduced by Lucas and Kanade and has been extensively described in a review by Barron et al. [19]. The algorithm obtains estimates of the motion of all points in the image of interest in a sequence of time-varying images using T1 signal intensity variations over time. All optical flow vectors are converted (from pixels per frame) to millimeters per degree/ millimeters of motion per degree change in gaze. The optical flow fields are subsequently mapped to a color-coded

Structure	Orientation	Motion (mm/deg)
Lens	Left - right	0.19-0.25
Optic nerve (anterior part)	Left - right	0.13-0.19
Optic nerve (posterior part)	Left - right	0.0-0.05
Medial rectus muscle	Anterior - posterior	0.7-0.12
Lateral rectus muscle	Anterior - posterior	0.8-0.12
Orbital fat	Left-anteriorly - right anteriorly	0.0-0.06

Table 1. Range of orbital soft tissue motion measured with MRI-DCM in 6 normal subjects. Motion is averaged over the corresponding anatomic region and only given if reliable. Compare these measurements to the theoretically expected motion of the lens, which can be calculated from the axial length of the eye as follows:  $\text{motion}_{\text{lens}} \approx 2\pi \text{radius}_{\text{eyeball}}/360 \text{ mm}/^\circ$ . For an (average) axial length of 25mm, the expected motion is 0.22 mm/deg.

image so that the color of any pixel shows both orientation over  $360^\circ$  (coded by hue) and length of the flow vector (coded by saturation) for that pixel (See Figure 1c). All pixels with reliable flow are set to the color appropriate for their magnitude and orientation in the corresponding gray-scale MRI image. If the flow is zero or cannot be measured reliably, the original MRI gray value shows [3]. At displacements of  $0.3 \text{ mm}/^\circ$ , the color of the pixel is fully saturated, while at lower displacements it becomes progressively paler. The software was written in Java and is available free of charge, including the sources, from the first author on request.

### 3. RESULTS

#### A) MRI-DCM

All subjects and patients were cooperative and underwent the MRI-DCM uneventfully. There was no need for conjunctival anesthesia and blinking did not interfere with image quality. Some patients tended to follow the gaze by small head movements for the  $40^\circ$  and  $48^\circ$  marks. Some, especially elderly patients, had difficulty sustaining fixation on the last targets in a sequence.

Optical flow and dynamic color maps could be obtained from all patients. Motion in areas with little or no features (i.e., areas with similar signal intensity values) on MRI, such as the vitreous and the intraconal space, was difficult to

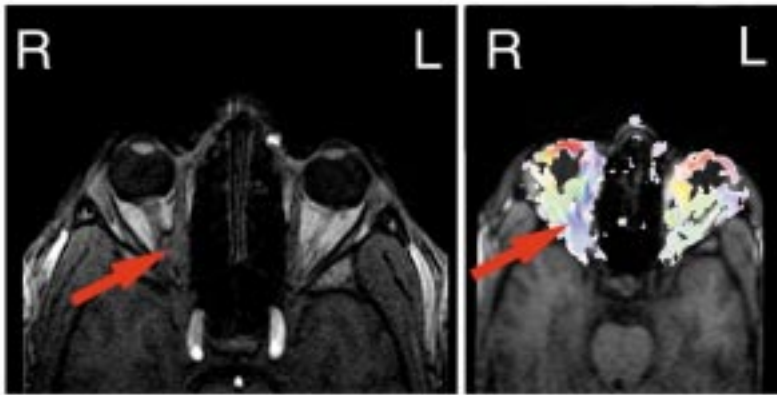


Figure 2. Localization of orbital mass in patient A. 2a. Static transversal MRI scan with (red arrow) a mass extending along the posterior portion of the medial rectus muscle and the optic nerve. b. MRI-DCM indicating (red arrow) that both the medial rectus muscle and the portion of the mass overlying the optic nerve move in the same orientation while the anterior portion of the optic nerve moves in a different orientation.

measure reliably, so that no flow could be shown in these areas (Figure 1). The optical flow and dynamic color mapping techniques are relatively fast, so that a sequence of DCM maps is generated in a few seconds.

### B) Healthy subjects

In order to obtain normal values for soft tissue motion, six healthy volunteers, four males and two females, were studied. The age varied between 23 and 35 years with normal corrected vision, normal ocular motility and normal ocular axis length. Figure 1 presents an example of MRI-DCM. The subject is gazing from left to right in a horizontal plane. The flow shown has been measured with the gaze at  $0^\circ$  (straight ahead). The colored index aids in understanding the relation of color to flow vector length and orientation. All motions discussed below are averages over the region of the corresponding soft tissue where motion could be measured reliably.

The lens moves to the right (red, average 0.20mm/deg), the medial rectus muscle of the right eye moves anteriorly (blue, average 0.15mm/deg) and the insertion of the lateral rectus muscle of the right eye moves posteriorly (pale yellow, average 0.12mm/deg). The optic nerve of the right eye moves to the left (green, 0.14mm/deg). Its anterior portion has the largest motion (most saturated green, 0.18mm/deg). Similar motion can be seen in the left orbit. There is slight motion around the nose because the subject follows his gaze by slightly turning his head ( $< 0.05$ mm/deg). The reliability of optical flow measured over relatively smooth areas such as intraconal fat was usually below the threshold so that no flow is shown there. The motion of various anatomical structures is summarized in Table 1.

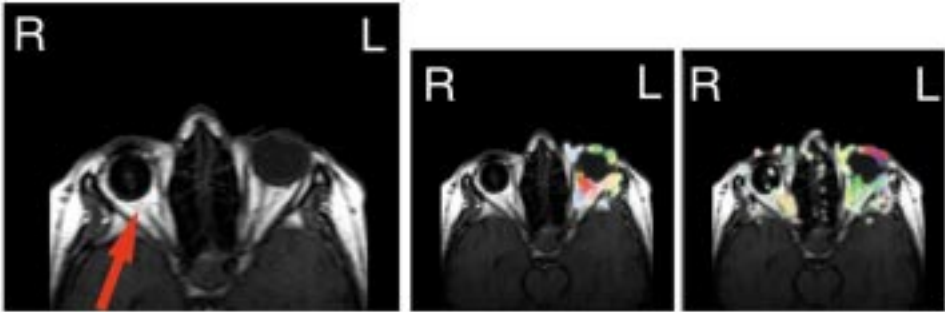


Figure 3. (Patient C) Enucleation with implant in right orbit, optic nerve not attached. a. Static transversal MRI scan. The optic nerve stump on the right seems close to or continuous with the implant. b. MRI-DCM with patient gazing from right to left. c. MRI-DCM with patient gazing from left to right. The healthy left eye moves normally. The implant on the right moves very little while the optic nerve stump does not move in b. and moves anteriorly in c. Shear is present and the optic nerve is not continuous with the implant.

### C) Patients

In order to investigate the usefulness of our approach for the differential diagnosis of intraorbital disorders, we examined four patients. Patients A and B had an orbital mass. As the history and diagnosis of patient B is very similar to that of patient A, we present only patient A in detail.

Patient A is a 35-year-old man with painful diplopia over a period of 18 months, and decreased visual acuity of the right eye over the last 2 months. On admission, his visual acuity was 0.2 OD, 1.25 OS; abduction was limited OD and the Hertel values were 24 mm OD, 21 mm OS. Funduscopy revealed optic disk edema. Thyroid stimulating hormone (TSH), T3 and T4 serum levels were normal. A CT scan and T1-weighted MRI scan (Figure 2a) showed a mass in the apex of the orbit, adjacent to the medial rectus muscle and the optic nerve. These images did not differentiate between a mass related to the optic nerve (meningioma or glioma), or to the medial rectus muscle (myositis or metastasis), or adherent to, but not continuous with the muscle (idiopathic inflammatory orbital tumor).

MRI-DCM was consequently obtained. In Figure 2b, the patient gazed from left to right. The anterior portion of the optic nerve (green, 0.18mm/deg) is moving to the left and the medial rectus muscle is moving anteriorly (blue, 0.13mm/deg). The mass in the apex covering the optic nerve is blue as well, suggesting that its motion is correlated with that of the medial rectus muscle and not with that of the optic nerve (which is green). The most likely explanation is that the mass is continuous with the muscle and in juxtaposition to the optic nerve, supporting the diagnosis of myositis. Because of this tentative diagnosis, treatment was started with intravenous steroids, with immediate result. Six months after treatment,

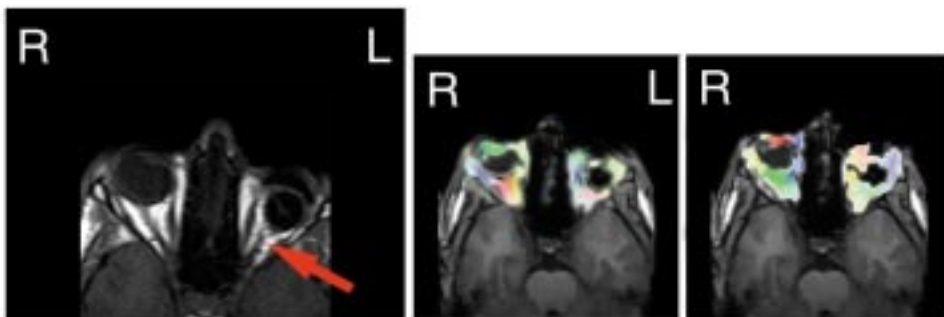


Figure 4. (Patient D) Enucleation with implant, optic nerve attached. a. Static transversal MRI scan. b. MRI-DCM with patient gazing from left to right. c. MRI-DCM with patient gazing from right to left. The implant on the left shows decreased motion compared to the healthy right orbit (0.14mm/deg) but moves concurrently with the stump. Shear is absent and the optic nerve is continuous with the implant.

patient had recovered visual acuity to 1.0 OD and improved but still slightly limited abduction.

Patients who have undergone enucleation of the eyeball may have persistent problems, such as cosmetic deformity, deep orbital pain and decreased motion of prosthesis. The usefulness of our technique was determined by examination of patients C and D. Enucleation has been performed according to the technique described by Collin [36] using a sclera-covered acrylic ball as the implant.

The right eye of patient C, a 35-year-old woman, had been enucleated two years before the study because of a painful blind eye. Figure 3a shows a static transverse MRI scan. The external ocular prosthesis is visible. In these figures, the optic nerve stump seems to be close to the (round) implant (compare with the healthy optic nerve of the contralateral eye). However, it is impossible to differentiate between juxtaposition of the nerve to the implant and continuity with the implant. Figure 3b and c show the MRI-DCM for patient C. On left gaze (Figure 3b), the lens of the left eye is moving left, in green. The implant on the right side hardly moves left (pale green, 0.04 mm/deg). The insertion of the lateral rectus moves anteriorly (pale blue, 0.05 mm/deg). The optic nerve stump does not show discernible motion (0.00 mm/deg). On right gaze (Figure 3c), the motion of the left eye is reversed. There is now some motion on the enucleated side, and the implant moves right (pale purple, 0.03 mm/deg). The posterior portion of the stump moves posteriorly (pale orange, 0.04 mm/deg). This shear of nerve and implant indicates juxtaposition and not continuity.

The left eye of patient D, a 53-year-old woman, was enucleated five years before the study because of a choroidal melanoma. Figure 4a shows the static MRI scan.

It is impossible to differentiate between juxtaposition of the nerve to the implant and continuity with the implant. Figures 4b and c show MRI-DCM for

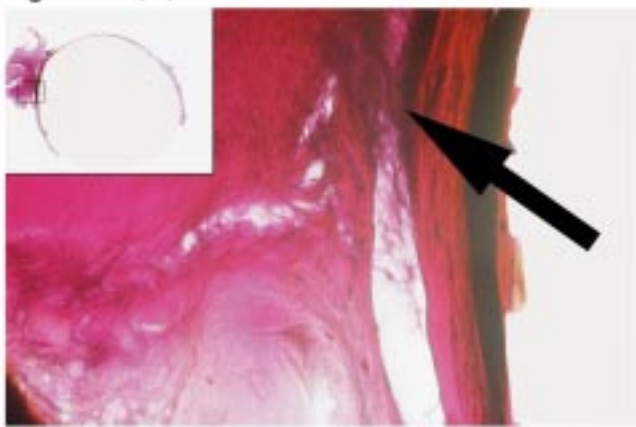


Figure 5. Histological section of surgically removed implant of patient D. The scleral cover on the right is connected to the stump of the optic nerve on the left by a mass of collagen fibers forming a pseudo-disk (black arrow). Inset: macroscopic aspect of the removed implant with the optic nerve including the remnant of the central retinal artery attached to it. Staining: Hematoxylin-eosin. Inset magnification,  $\times 0.8$ .

patient D. On leftward gaze (Figure 4b), the lens of the right eye moves leftward. The front of the implant moves left (green,  $0.14 \text{ mm}^\circ$ ), and the stump moves right (light red,  $0.04\text{-}0.1 \text{ mm}^\circ$ ). On rightward gaze (Figure 4c), soft tissue motion has the reverse orientation. In contrast to patient C, this absence of shear between nerve and implant indicates continuity, not juxtaposition. Patient D underwent orbital exploration because of persistent and drug-resistant orbital pain. Figure 5 shows a histological section of the removed implant where the optic nerve can be seen to be attached over a large area to the back of the scleral cover.

#### 4. DISCUSSION

This study introduces a new technique for measuring the motion of soft tissues in the orbit, MRI-DCM. The technique allows the non-invasive determination of the kinetics of orbital tissues such as muscle, optic nerve, orbital fat and tendon in millimeters per degree change in gaze position. The technique is feasible using clinical MRI equipment, is tolerated by subjects and patients and, by its quantitative nature, avoids intra- and inter-observer variation. It has about the same cost as conventional MRI and, if a static MRI is requested, can be performed simultaneously at that appointment.

There are a few disadvantages to MRI-DCM. It can be difficult in patients who cannot concentrate for an extended period of time, especially elderly patients who may find the large number of targets confusing. By improving the optical flow algorithm, we have meanwhile (after this study was completed) been able to reduce this number. The technique is contraindicated in patients with pacemakers or arterial clips, and in some patients with metal implants. Optical flow and DCM

are image-processing methods that are most sensitive to tissues that show many MRI features (and have relatively inhomogeneous signal intensities). Motion is more difficult to measure reliably in tissues that are relatively 'smooth,' such as vitreous and fat. Up to now, only two-dimensional motion can be measured.

MRI-DCM allows measurements of soft tissue motion in healthy subjects. Motion tends to range between 0.0 and 0.25 mm/deg, depending on the type of tissue and the position of the tissue in the orbit relative to the eyeball. The measured range of motion for the lens is close to the one expected from the calculations (Table 1). No objective measurement is currently available for orbital kinetics. The only possible validation would be by an invasive technique, probably influencing the very kinetics it is meant to measure.

MRI-DCM allows additional information beyond CT and MRI in orbital lesions and, in contrast to these techniques, allows a differentiation between juxtaposition and continuity of tissues. In patient A, MRI-DCM showed that the mass was continuous with the medial rectus muscle (the most likely cause being an origin in the muscle), thus facilitating the diagnosis of myositis. It may be of clinical value in differentiating the origin of a retrobulbar lesion and may replace the need for a risky biopsy in the apex of the orbit.

MRI-DCM allows measurement of soft tissue motion after enucleation. In patients C and D, soft tissue motion in the entire enucleated orbit (0.0 - 0.14 mm/deg) was less than that in the healthy contralateral orbit (0.0 - 0.24 mm/deg). This is in agreement with earlier nonquantified observations [65].

Little is known about the anatomy in the orbit after enucleation and implant. MRI-DCM allows differentiation between juxtaposition of the optic nerve to and continuity with the scleral cover of the implant after enucleation. Much to our surprise we discovered that after enucleation, the optic nerve stump showed regrowth to the sclera cover. The latter finding has been confirmed by biopsy [4]. Such attachments have previously not been recognized, probably because on static CT and MRI scans, it is impossible to differentiate between juxtaposition and continuity of structures. Further studies should be undertaken to reveal the clinical significance of this phenomenon.

We want to stress that the common basis for this last conclusion is that the more similar the motion of two adjacent structures (i.e., the more similar their colors in a MRI-DCM image) the more likely it is that they are continuous. In this study, we examined only this aspect of orbital kinetics. We hope to extend our studies to disorders of ocular motility in the future.



## 7

# Patients with persistent pain after enucleation studied by MRI Dynamic Color Mapping and histopathology

Presented in part at the annual meeting of the Association for Research in Vision and Ophthalmology, Fort Lauderdale, Florida, May 1997.

*Purpose:* to study possible causes of persistent pain in patients who underwent enucleation of the globe and in whom all other non-invasively detectable causes of pain had been ruled out. *Methods:* Twenty patients were studied, 10 with intractable pain (score > 5 on a 0-9 self-reporting pain scale) persisting for more than 6 months after enucleation (for various reasons) and 10 without pain (score < 4) enucleated at least 6 months at least 6 months after enucleation. Magnetic resonance imaging (MRI) – dynamic color mapping (MRI-DCM) was used to quantify the motion of the optic nerve in millimeters per degree, 2 to 3 mm behind the implant. Histopathologic study of biopsy specimens was used to verify imaging findings. *Results:* The optic nerve was attached to the implant in almost all (19/20) patients. On average, the motion was significantly less in patients with persistent intractable pain ( $0.04\text{mm/}^\circ$ ) than in patients without pain ( $0.08\text{mm/}^\circ$ ) on average (normal orbit,  $0.13\text{mm/}^\circ$ ). A biopsy specimen was available in 5 out of 10 patients with persistent pain, and in 4 of those 5, microscopic neuroma was found close to the optic nerve–implant junction. *Conclusions:* In the enucleated orbit, the optic nerve is usually attached to the implant and soft tissue motion is decreased. In patients who have persistent pain after enucleation, motion is decreased even more, and a high percentage of microscopic amputation neuromas are found. Increased stiffness of orbital soft tissue and optic nerve attachment after enucleation are detectable using MRI-DCM, and may play a role in susceptible patients in the development of microscopic amputation neuroma and pain.

## 1. INTRODUCTION

The main indications for removal of an eye are intra-ocular tumors, persistent ocular pain and cosmesis. Enucleation is usually effective in resolving pain [133;159], but, in rare cases, pain may persist [67;112;147]. The following causes of persistent pain after enucleation (or anophthalmic socket pain) are detectable by

non-invasive means: nonoptimal fit of prosthesis, migration of the implant, lacrimal insufficiency, inflammatory conditions, space-occupying lesions and psychiatric disorders [67]. Another cause however, painful microscopic amputation neuroma (nerve tumor), is only diagnosable by removal of the implant and adherent tissues and subsequent histologic analysis [67]. Neuromas are thought to be the result of tractional or compression forces on the nerve, which are also thought to cause increased stiffness of the nerves and surrounding tissues [30;108;158]. The motion of soft tissues in the enucleated orbit can be assessed by a variety of means [85]. It can be measured non-invasively and objectively by magnetic resonance imaging with dynamic color mapping (MRI-DCM), consisting of fast cinematic MRI and optical flow motion analysis [3;7].

The purpose of this study was to determine possible causes of persistent pain in patients who underwent enucleation of the globe and in whom all the noninvasively detectable causes listed above had been ruled out.

## 2. METHODS

The study involved an observational case-control design with 20 subjects: 10 patients with intractable persistent pain and 10 who served as controls. Patient data are summarized in Table 1. Patients were included in the *pain* group if they had undergone enucleation at least 6 months before inclusion, persistent pain had been present for at least 6 months and detectable causes of pain according to the criteria put forward by Glatt et al. had been excluded [67]. The pain was scored through an interview on a 0-9 pain scoring scale (see Table 2). Patients were only included if they scored 6 or more on this scale. Patient controls were selected for the *no-pain* group by random selection from the outpatient clinic records of our hospital (a tertiary care center). Patient controls were included if they had undergone enucleation at least 6 months before inclusion and scored 3 or less on the pain scoring scale. In addition to these criteria, all subjects had to more than 18 years of age and eligible for MRI-DCM examination [7]. All subjects were treated in accordance with the tenets of the Declaration of Helsinki, and written informed consent was obtained after the nature of the study had been explained. The approval of the institutional review board of our hospital was obtained for the research protocol and the informed consent form.

MRI-DCM was performed according to a protocol published previously [3;7]. Transverse sequences of gradient echo T1-weighted images are acquired while the patient sequentially fixates on a row of nine horizontal fixation marks placed at  $8^\circ$  intervals on the inside of the scanner bore. The motion in these sequences is estimated by first order optical flow computation of motion estimates. All motion vectors are converted (from pixels per frame) to ratios of millimeters per degree change in gaze.

The conversion from pixels to mm is performed by the MR scanner software, while the motion is converted from mm/frame (of  $8^\circ$  each) to  $\text{mm}/^\circ$  by division. The error of the motion measurement (direction and magnitude combined) was

Patient	Age	Gender		Reason for enucleation	Presence of painful atrophy	Type of implant	Years since enucleation	Score on pain scale	Optic nerve motion mm/°	Biopsy taken	Microscopic neuroma in biopsy?
<i>No Pain</i>											
1	59	f		melanoma	n	baseball	5	0	0.03		
2	88	m		melanoma	n	baseball	6	0	0.15		
3	83	f		melanoma	n	baseball	5	0	0.06		
4	43	m		painful atrophy (detachment)	y	baseball	5	0	0.14		
5	65	f		tumor	n	baseball	35	0	0.11		
6	59	m		painful atrophy (dislocated lens)	y	Allen	35	1	0.05		
7	66	m		trauma	n	baseball	32	1	0.09		
8	38	f		painful atrophy (endophthalmitis)	y	baseball	33	1	0.08		
9	93	f		melanoma	n	Allen	22	1	0.03		
10	25	m		painful atrophy (detachment)	y	baseball	7	2	0.06		
<i>Pain</i>											
11	57	m		painful atrophy (glaucoma)	y	Allen	11	8	0.04	y	n
12	50	f		melanoma	n	Allen	1	7	0.06	n	
13	46	f		painful atrophy (keratoplasty)	y	baseball	6	8	0.01	y	y
14	52	f		trauma	n	baseball	18	8	0.04	n	
15	52	f		painful atrophy (detachment)	y	baseball	8	6	0.01	y	y
16	22	m		painful atrophy (detachment)	y	baseball	5	8	0.03	y	y
17	47	m		trauma	n	baseball	5	7	0.03	n	
18	30	f		painful atrophy (endophthalmitis)	y	baseball	20	9	0.05	y	y
19	23	f		trauma	n	Allen	1	8	0.04	n	
20	56	m		melanoma	n	Allen	8	7	0.08	n	

Table 1. Data of *no-pain* and *pain* groups.

found to be less than 15%, and the error in magnitude by itself less than 8% in validation studies [3].

An experimental version of the DCM and optical flow software is available at no charge from the Image Sciences Institute, Utrecht, the Netherlands, at “<http://www.isi.uu.nl/people/michael>.” (please observe copyright and disclaimer notices).

Score	Examples
0	No pain
1	Occasional tenderness (less than once weekly)
2	Occasional stab of pain (less than once weekly)
3	Frequent tenderness (less than once a day)
4	Frequent stabs (less than once a day)
5	Pain occasionally distracting (more than once a day)
6	Pain frequently distracting, but work and relaxation are possible
7	Always pain, occasionally disturbs sleep
8	Pain frequently disturbs sleep
9	Pain makes concentrating on any task difficult

Table 2. English version of the anophthalmic socket pain scoring scale developed for this study. In using this scale, the use of non-opiate analgesics is disregarded.

The magnitude of the motion of the optic nerve 2 to 4 mm behind the implant was used as an indicator of soft tissue motion, and recorded in millimeters per degree. The motion of the outside of the implant, next to the stump of the optic nerve, was also recorded in mm°. Normal motion of the contra-lateral healthy eye was verified by checking the motion of the lens of that eye.

To determine attachment of the optic nerve to the implant, the orientation of the motion of the optic nerve and of the implant during left and right gaze were compared. If the orientation of the motion of these structures differed from each other less than 45°, the optic nerve was recorded as *attached* to the implant, otherwise the optic nerve was recorded as *not attached*. With rigid attachment, the motion of the optic nerve and the implant are expected to be exactly the same (in other words, the difference should not be larger than 0°). The 45° limit was chosen before to the study so that more loosely coupled attachments could also be diagnosed. Averages are presented as mean and 95% confidence interval. Patient data across groups were analyzed with Pearson’s  $\chi^2$  test. Data were averaged for the *pain* and *no pain* groups, and compared with the unpaired Student’s *t*-test. For the significance test, a two-tailed  $p < 0.01$  was used. Analysis was performed by computer (Excel 7.0; Microsoft Corp, Seattle, WA).

### 3. RESULTS

The mean age in the *pain* group was 43±13.4 (SD) years, and in the *no pain* group 63±23.2 years. There was a significant difference in age ( $p=0.015$ ), partly because

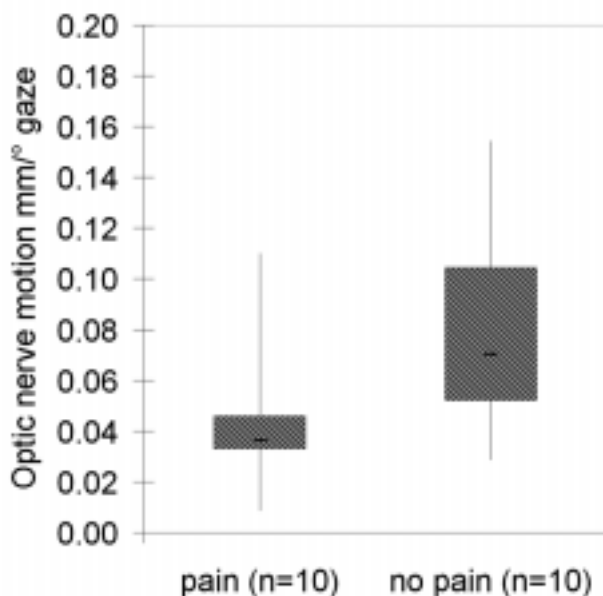


Figure 1. Optic nerve motion in patients with and without persistent intractable pain. The upper and lower edges of the box indicate the upper and lower quartiles of the motion (all in  $\text{mm}/^\circ$ ). The extent of the upper and lower whiskers indicate the maximum and minimum motion. The thick line within the box indicates the mean motion.

of biased patient selection. Of the 16 subjects originally eligible for inclusion in the *no-pain* group, three could not be reached, and three refused participation (these usually stated that they would have had to take time off from their jobs for research of no benefit to themselves). The mean age of these 16 subjects was 57.1 years, not different ( $p=0.08$ ) from the mean age in the *pain* group. There was no statistical difference in gender ( $\chi^2=0.689$ ,  $p=0.41$ ) and side of surgery ( $\chi^2=1.0$ ,  $p=0.32$ ) between the two groups. Reasons for enucleation varied, but there was no significant difference in the frequency of painful atrophy ( $\chi^2=0.84$ ,  $p=0.36$ ). No patients reported an increase or a change in character of the pain on ocular motion, all subjects were cooperative and underwent MRI-DCM uneventfully, and all subjects were able to follow all gaze positions.

Optic nerve motion, motion of the implant and attachment of the optic nerve to the implant are summarized in Table 1. The optic nerve was always attached to the implant in the *pain* group and in all except one patient in the *no-pain* group. In the normal contra-lateral eye, all subjects had normal gaze motion (average  $0.13/^\circ$ , 95% confidence interval [CI]  $0.122\text{mm}/^\circ - 0.148\text{mm}/^\circ$ ) and could fixate all marks. Figure 1 shows the mean and the upper and lower quartiles of the motion in the *pain* and *no-pain* groups. The frequency distributions of the motion in both groups

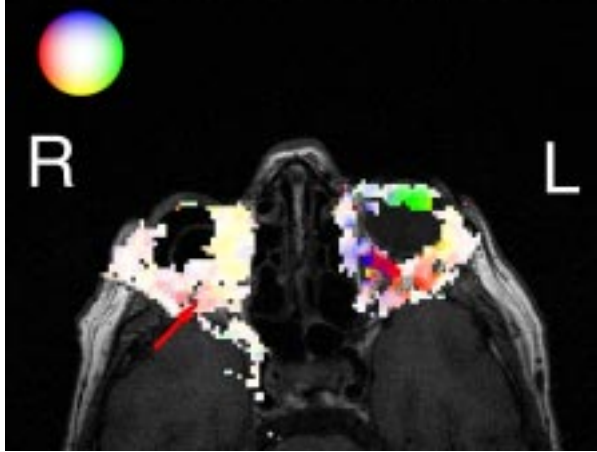


Figure 2. Visualization of soft tissue motion for patient 15 (*pain* group). Baseball implant in the right orbit, with patient gazing to his left. The optic nerve and surrounding tissues in the enucleated orbit are moving less than the normal tissues in the normal orbit (more saturated colors). The back of the implant is moving less than the optic nerve, and the optic nerves and the other soft tissues have motion of similar magnitude (similar saturation). The motion of the optic nerve is coupled to that of the back of the implant. The index in the upper left side of the figure helps in understanding the orientation and magnitude of motion in relation to a color (saturated green is fast to the left, i.e. right in the figure; pale yellow is slow posteriorly). *Red arrow*: position where optic nerve motion is measured.

approximately followed a normal distribution. The average optic nerve motion was decreased ( $p < 0.01$ ) in the *pain* group (average  $0.04 \text{mm}^\circ$ , 95% CI  $0.026 \text{mm}^\circ - 0.050 \text{mm}^\circ$ ) in comparison to the *no pain* group ( $0.08 \text{mm}^\circ$ , 95% CI  $0.053 \text{mm}^\circ - 0.108 \text{mm}^\circ$ ). This difference in soft tissue motion between groups could be entirely attributed to the difference between patients with baseball-type implants, with and without pain, as shown by segregation of the groups according to implant type. Between patients with baseball implants ( $n = 14$ ) with and without pain there was a significant average difference of  $0.06 \text{mm}^\circ$  ( $p = 0.005$ ), while between patients with Allen implants ( $n = 6$ ) there was no ( $p = 0.41$ ) difference.

There was no correlation of the soft tissue motion with age in either the *no pain* or *pain* groups. Figure 2 shows a visualization of soft tissue motion in the enucleated orbit for patient 15 from the *pain* group. Figure 3 shows the anatomy and the attachment of the optic nerve to the implant for this patient in more detail.

In 5 of 10 patients in the *pain* group, a biopsy specimen of tissue around the optic nerve-implant junction was taken through a transconjunctival incision. The other five patients refused a biopsy for a variety of reasons. In four (80%) of the former five patients, one or more amputation neuromas were present in the biopsy specimen. In one patient, the only one of this group with an Allen implant, no neuromas were found. The neuromas were always located close to the junction of the optic nerve with the implant, either along the nerve or along the anterior part of

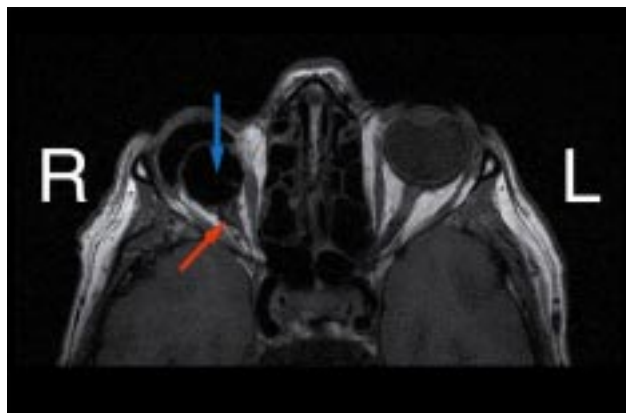


Figure 3. Static MRI for patient 15. *Blue arrow* baseball implant attached to the optic nerve in the right orbit, with the prosthesis in front of it. *Red arrow* junction of the optic nerve to the back of the sclera covered implant.

an extraocular muscle. Figure 4 shows a histological section with an amputation neuroma from patient 16. After the biopsy, three of the four patients with a neuroma showed resolution of pain (defined as a pain score of 3 or less, six months after biopsy).

#### 4. DISCUSSION

The results of this study indicate that in the enucleated orbit, tissue motion is decreased in comparison to tissue motion in the normal orbit; the optic nerve stump is usually (19/20) attached to the implant ; tissue motion is decreased even more in patients with persistent intractable (i.e. in which all non-invasively detectable causes of pain have been excluded) pain, compared to enucleated patients without pain, and this decrease is present only in patients with baseball implants; and amputation neuromas can often be found near the optic nerve / implant junction in these patients.

Possible sources of bias in this study may include the higher average age in the *no pain* group compared to the *pain* group. However, we found no correlation between tissue motion and age in our patients, and to our knowledge, there is no evidence in the literature for such an age dependent effect. Another possible source of bias is potential inaccuracy in the optical flow motion estimation technique; but the optical flow algorithm has been shown to occasionally underestimate (but not overestimate) larger motion magnitudes in validation studies [3]. Motion in the enucleated socket may be less because of the pain; however, motion in the contralateral healthy orbit was normal. The number of patients (five) in which a biopsy was available was too small to establish a relationship between decreased motion and presence or absence of painful microscopic neuroma. It is possible that in most of the other patients with pain, no neuromas would have been found. Although

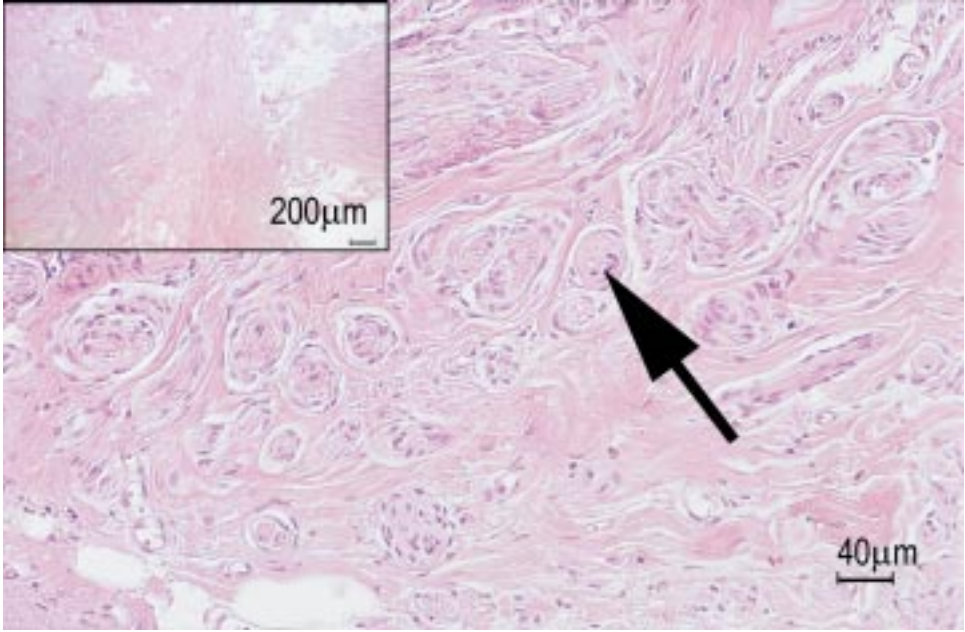


Figure 4. Biopsy specimen from patient 16 showing microscopic amputation neuroma located close to the optic nerve – implant junction. Hematoxylin-eosin stain. (*Black arrow*) small nerve fiber bundle. (*Bar*) = 40 $\mu$ m. Inset: low magnification overview with optic nerve stump on the right and fibrous tissue near its junction to the implant containing amputation neuroma on the left. (*Bar*) = 200 $\mu$ m.

neuromas often cause pain, especially if subject to pressure and/or motion, this is not always the case. It is possible that in patients without pain, neuromas are also present in the enucleated orbit [158]. However, the fact that three out of four patients had resolution of pain suggests a causal relationship.

To our knowledge, this is the largest study of patients with persistent intractable pain after enucleation and the first to look at the role of tissue motion in the enucleated orbit. The decrease in motion in patients with persistent pain and baseball implants may be related to tight attachments of the optic nerve to the intraconal fatty tissue or higher stiffness of the orbital contents due to fibrosis caused by the surgery. In combination with the movement of the optic nerve during gaze due to its attachment to the implant, this tightness or stiffness may subject the intraorbital nerves to increased, continuously changing pressure and traction and decreased motion. All these are favorable conditions for the development of painful amputation neuroma [158]. This mechanism may explain that such a large proportion of the patients who had persistent intractable pain had microscopic amputation neuroma. In these patients, by definition, no macroscopic neuromas

were present, and the neuromas that were found histologically were very small, and thus would have easily escaped detection on MRI or computed tomography.

In conclusion, this study shows that MRI-DCM may be of use in the evaluation of persistent intractable pain after enucleation. This procedure is capable of showing that tissue motion is decreased in the enucleated orbit in comparison to the normal orbit, and that the optic nerve is usually attached to the implant. Of course, its sensitivity and specificity in diagnosing this condition remain to be established. Other methods, such as semi-automatic measurement from two- and three-positional MRI, are just as capable of measuring the globe-optic nerve motion as the optical flow method used in MRI-DCM [33]. Globe-optic nerve motion was selected as a reproducible indicator of intraconal soft tissue motion: MRI-DCM is capable of measuring the motion of any orbital tissue, and we could have chosen to measure any other region in the soft tissue, which is much more difficult with semi-automatic motion measurement from two- and three-positional MRI.

In patients with persistent pain, motion is decreased even more, and in these patients, a high percentage of amputation neuromas are found close to the implant. Increased stiffness of orbital soft tissue and optic nerve attachment after enucleation are detectable using MRI-DCM. These circumstances and the consequent continuously changing pressure and motion in the enucleated orbit may play a role in some patients in the development of painful microscopic amputation neuroma and persistent intractable pain. Further study in a more extensive group is required to verify these findings, and a post-mortem study may be useful to evaluate enucleated orbits. Further study may also reveal what steps, if any, can be taken to ensure the removal of all amputation neuromas from the orbit to effect an improvement in the pain these patients experience.



# 8

## Rectus extraocular muscle paths before and after decompression surgery for Graves' orbitopathy: relationship to motility disturbances

Presented in part at the annual meeting of the Association for Research in Vision and Ophthalmology, Fort Lauderdale, Florida, May 2000.

**Purpose:** to study possible causes of motility disturbances that may result from orbital decompression surgery in patients with Graves' orbitopathy, and especially the role of rectus extraocular muscle paths.

**Methods:** Sixteen patients with Graves' orbitopathy were studied before and three to six months after translid (6 patients) and coronal (10 patients) orbital decompression surgery for disfiguring proptosis. Ocular motility changes were objectively measured by comparing maximum ductions and severity of diplopia, and the positions and the displacements of the anterior rectus muscle paths were measured using cine MRI imaging. **Results:** Averaged preoperative rectus muscle paths positions were not different from normals. Averaged postoperative muscle path positions were generally the same as preoperative paths. The only significant exceptions were centrifugal (outward from the orbital axis) displacements of the inferior rectus muscle path (IR) after translid, and of the medial rectus muscle path (MR) after coronal surgery. The amount of IR displacement with translid surgery was directly correlated with range of depression and with severity of vertical diplopia. The amount of MR displacement with coronal surgery was inversely correlated with range of abduction and directly correlated with severity of horizontal diplopia. **Conclusions:** The anterior orbital connective tissue seems to form a 'functional skeleton' that is usually (except as noted for IR respectively MR) capable of keeping the rectus muscle paths aligned after decompression surgery, and preserving the normal functions of rectus muscle pulleys. The centrifugal displacement of the IR and MR may increase the elastic component of the muscle force, leading to the specific patterns of motility disturbance that may occur in some patients after translid and coronal surgery. These findings suggest that standard surgical management of Graves' orbitopathy be supplemented by appropriate muscle surgery.

## 1. INTRODUCTION

Graves' orbitopathy can lead to disfiguring proptosis, motility disturbances and optic neuropathy. Orbital decompression surgery plays an important role in the rehabilitation of patients suffering from Graves' orbitopathy [102;137] and has been shown to be effective in restoring vision and reducing proptosis [118]. However, decompression surgery also induces or aggravates ocular motility imbalances in 10-80% of cases [49;63;122]. To date, explanations for this complication have been mostly speculative.

In 1989, Miller introduced the rectus muscle pulley concept [113]. The pulleys are musculofibrous structures in the anterior orbit that constrain the paths of the rectus muscles, relative to the orbital wall, similar to the way the trochlea constrains the path of the superior oblique muscle. They thus form the functional origin of these muscles [53], and have been demonstrated to lie a few mm posterior to the equator of the globe and keep their position as gaze varies [115]. In the first experimental test of the pulley concept, Miller et al. [115] imaged muscle paths before and after transposition surgery, and found that positions of muscle bellies relative to the orbital walls were little affected. Other studies have suggested that precise pulley location is critical to normal three-dimensional ocular kinematics [34;126;127].

Most forms of decompression surgery involve extensive dissection of the periorbita, including the pulley insertions in the orbital wall, the creation of large osteotomies from orbital rim to apex, followed by incision of the periorbita. If pulley stability relative to the orbital wall was due only to their direct insertions in the wall, such procedures would be expected to greatly influence ocular motility. From this viewpoint, it is surprising that motility disturbances occur in only a minority of patients after orbital decompression.

Our purpose is to study possible causes of motility disturbances as a result of orbital decompression surgery in patients with Graves' orbitopathy. Rectus muscle paths were measured before and after the translid and coronal approach to decompression surgery, and the relationship of path displacements to ocular motility parameters - changes in maximum duction and in diplopia - was determined.

## 2. METHODS

Sixteen patients were included in a prospective, non-randomized cohort study conducted over two years. Included patients were between 18 years and 65 years of age, diagnosed with Graves' orbitopathy, candidates for either translid or coronal decompression surgery (see below), and available for pre-operative MR (Magnetic resonance) imaging. Severity and activity of orbitopathy, the need for decompression surgery, and the approach were determined by a single surgeon in all cases (MPM). Criteria favoring translid surgery included unilateral proptosis or the possibility of a receding hairline (especially males), since coronal surgery may leave a visible scar, whereas criteria favoring coronal surgery included severe or bilateral proptosis [118].

Patients were excluded from the study if they were ineligible for MR imaging because of the presence of any metallic material in the skull (except for dental fillings), a history of psychosis or claustrophobia, or near visual acuity less than 0.3, the minimum required to see the fixation marks in the scanner bore. Four patients were excluded because they did not complete the study: two had claustrophobic complaints during the first (pre-operative) MR scan, and two did not show up for the post-operative MR scan. None of these four patients had decompression-induced duction changes and all had Not Worse diplopia (see below).

The study protocol involved three-dimensional cine MRI scanning (see below) and orthoptic examination (see below) less than one week before decompression surgery and three to six months after surgery. Of the 16 patients, six ( $n = 10$  orbits) underwent translid surgery and were included in the *translid group*. Ten patients ( $n = 20$  orbits) underwent coronal surgery and were included in the *coronal group*.

All subjects were treated in accordance with the tenets of the Declaration of Helsinki, and prior written informed consent was obtained after the nature of the study had been explained. The approval of the institutional review board of our hospital was granted for the research protocol and the informed consent form.

#### A) Ocular motility

Ocular motility was always assessed by the same researcher. It consisted of cover test, cover prism-test, Lancaster-Hess chart and measurement of monocular maximum ductions (abduction, adduction, elevation and depression) in degrees for both eyes, with the forehead and chin fixated in a modified Goldmann perimeter, as described previously [119]. Ocular motility was assessed one week before and three to six months after surgery. Horizontal and vertical diplopia changes as a result of decompression surgery were classified separately as follows:

- ◆ Not Worse - defined as unchanged or less diplopia
- ◆ Worse - defined as a shift from no diplopia in any gaze to diplopia in the extremes of gaze, *or* a shift of diplopia in the extremes of gaze to diplopia in primary or reading position
- ◆ Much Worse - defined as a shift of no diplopia to diplopia in primary or reading position.

#### B) Rectus muscle paths

MR gradient echo T1-weighted three-dimensional cine sequences were acquired in a *stop-shoot* (see below) manner on a 1.5 Tesla MR scanner (Philips Gyroscan NT version 6.0, Eindhoven, the Netherlands). A head-coil was used in TFE (Turbo Field Echo) mode with settings: TE (Echo Time) 4.598 ms, TR (Repetition Time) 9.36 ms, Flip Angle 20 degrees, matrix 256x256x20, resulting in an acquisition time of 15s per volume and a voxel size of 0.8x0.8x2.0 mm.

The patients sequentially fixated on three rows of numbered marks placed on the inside of the scanner-bore. After the acquisition of a volume (shoot), the

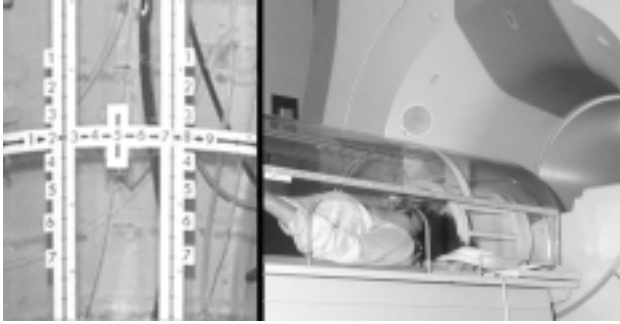


Figure 1. (left) a: Detail of fixation device with numbered fixation marks; (right) b: subject on dolly in front of MR scanner bore, with fixation device in place and adjusted to proper distance to globes.

patient fixated the next fixation mark (stop), and then the next volume was acquired, *etc.* One row was horizontal relative to the head of the patient in the scanner and had nine fixation marks placed at intervals corresponding to approximately an  $8^\circ$  gaze angle difference (from  $-32^\circ$  over  $0^\circ$  to  $+32^\circ$ ). Two rows were vertical relative to the head of the patient. Each of these two rows had seven fixation marks placed at  $8^\circ$  intervals (from  $-24^\circ$  over  $0^\circ$  to  $+24^\circ$ ), one row straight ahead of the right eye (with the left eye abducted  $20^\circ$ ), and one row straight ahead of the left eye (with the right eye abducted  $20^\circ$ ). Thus, one sequence of nine MR volumes corresponding to nine different horizontal gaze positions (from  $24^\circ$  abduction to  $40^\circ$  adduction for each eye in the vertical  $0^\circ$  position), and two sequences of seven MR volumes corresponding to seven different vertical gaze positions each (from  $24^\circ$  elevation to  $24^\circ$  depression for each eye in  $20^\circ$  abduction, and the other eye in the horizontal  $0^\circ$  position) were obtained. See Figure 1.

Actual gaze angles were corrected for parallax taking into account interpupillary distance and distance of lateral orbital rim to the fixation marks [3;7]. Motion of the head of the patient was restrained by a flexible headband. The T1 relaxation times were coded as 12-bit signal intensities and the resulting volume sequences were stored in DICOM (Digital Imaging Communications in Medicine) 3.0 format as series of separate consecutive images. The volume dimensions were calibrated in mm by the scanner software. To minimize post-processing, the patient's head was aligned in the scanner to have the interhemispheric fissure aligned with the scanner's y-axis, and the long axis of the lateral rectus muscles with the z-axis. See Figure 2 for an explanation of the axes.

Rectus muscle paths were defined as the line connecting the centroids (the digitally computed center of gravity of the muscle boundary) of muscles in consecutive planes perpendicular to the orbital axis. They were located following the methods set forward by Clark, Miller and Demer [31;33]. Our method to determine rectus muscle paths from the volume data is very similar to theirs: in

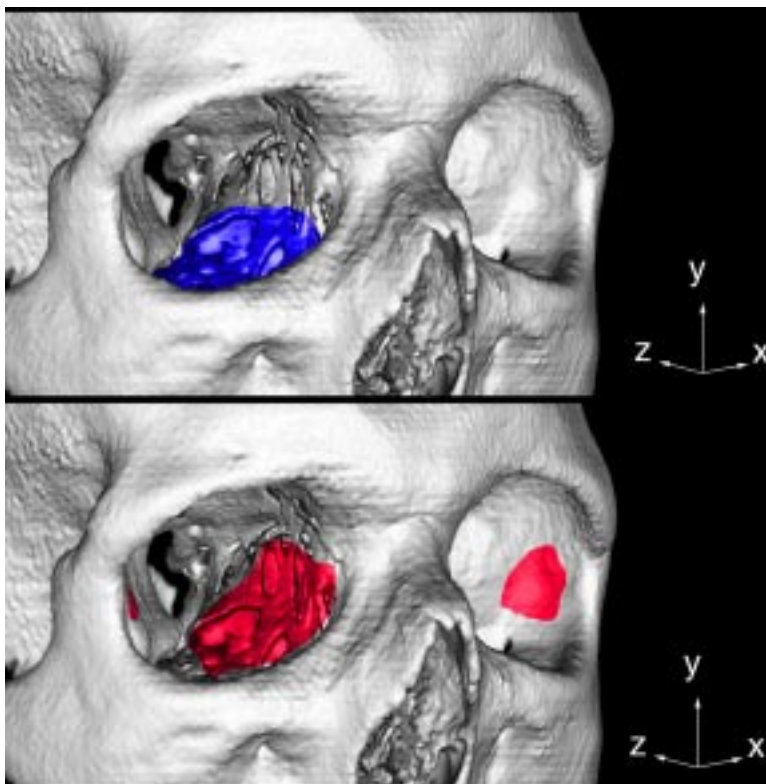


Figure 2. Osteotomies for (top) translid (two-wall) and (bottom) coronal (three-wall) decompression. Translid osteotomies are shown in blue, coronal osteotomies in red. The orbital walls and the anterior skull have been volume rendered (“<http://www.isi.uu.nl/people/michael>.”) from pre-operative high-resolution computed tomography (CT) data. The medial orbital wall is very thin, and in some areas the bone is incorrectly not shown. The arrows illustrate the orientations of the x-, y- and -z-axes.

brief, as follows. Image analysis was performed using the ImageJ program (developed by Wayne Rasband at the United States National Institutes of Health and available at “<http://rsb.info.nih.gov/ij>”) and additional programs (by the first author and available at “<http://www.isi.uu.nl/people/michael>.”).

The MRI volume data were normalized by a single (trilinear) interpolation to minimize data loss. For this interpolation, the inter-hemispheric fissure of the brain was aligned with the y-axis of the volume (‘chin to crown’), the line connecting both optic nerves in the coronal plane were aligned with the x-axis of the volume (‘ear to ear’), and the anteroposterior axis of the orbit was aligned with the z-axis of the volume (‘nose to nape of neck’). This last normalization was necessary

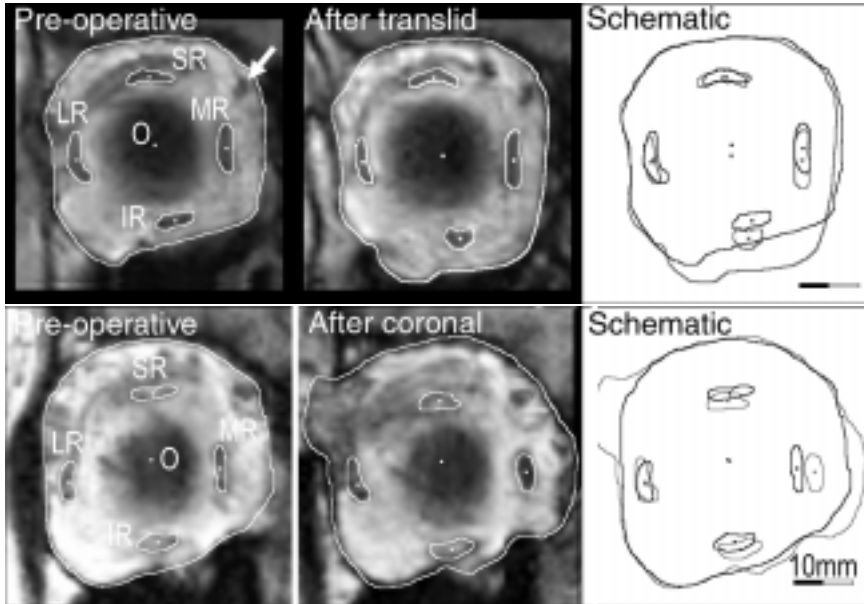


Figure 3. Determination of rectus muscle path centroids and displacement of orbital center and muscle paths in normalized MRI scan perpendicular to the orbital axis approximately 3mm before the globe-optic nerve junction. Above (A,B,C): right orbit of typical *translidid group* patient. Below (D,E,F): right orbit of typical *coronal group* patient. A) Muscle paths and orbital circumference before and B) after translidid two-wall surgery. C) Schematic drawing of circumference of orbital soft tissue and rectus muscle paths of same patient before (black) and after (light gray) surgery. The orbital tissue expands downward as a result of the decompression surgery. The inferior rectus muscle path shows the largest (downward) displacement relative to the orbital center, in this case 0.8mm. The orbital center is also displaced downward, causing a relative upward displacement of the superior rectus path. D) Muscle paths and orbital circumference before and E) after coronal three-wall surgery. D) Schematic drawing of circumference of orbital soft tissue and rectus muscle paths. The orbital tissue expands medially and laterally as a result of the decompression surgery. The medial rectus path is displaced the most, in this case 0.7mm. The orbital center moves only slightly. The bony orbital walls are not visible. The bars indicate 10mm. SR = superior rectus muscle path, IR = inferior rectus muscle path, LR = lateral rectus muscle path, MR = medial rectus muscle path, O = centroid of orbital circumference. Arrow indicates superior oblique muscle tendon.

because left and right orbits were scanned in a single volume sequence with the z-axis of the volume along the anteroposterior axis of the skull [41].

The normalizations never needed to be larger than  $5^\circ$ . The gaze angle was checked using the position of the optic nerve-globe junction. After enlarging the orbital volume data 4 times, the x-(mediolateral) and y-(superoinferior) coordinates of the area centroids of the extraocular rectus muscles and of the orbital soft tissue were measured (in mm) in the coronal plane by tracing their boundaries. See Figure 3.

The area centroid of the orbital wall circumference was used as the origin to normalize the muscle path positions to a semi-orbitocentric coordinate system as shown in Figure 3. In this coordinate system, the x- and y-coordinates are measured relative to this origin while the z-coordinates (the 'Planes' below) are measured relative to the position of the globe-optic nerve junction [115]. Since the thin bony orbital walls are not visible in MR images, the boundary of orbital soft tissue in that volume was used to trace the orbital wall circumference. This implies that the plane in which the orbital circumference and the orbital center were measured can differ before and after decompression surgery. In other words, no regard was made to pre-operative location of the orbital center or orbital walls in determining the origin of the post-operative coordinate system. The MR slice thickness (the z-dimension of the voxel) was 2.0mm, and in the x- and y-dimension 0.8mm, making measurements in the z-dimension less accurate. Planes perpendicular to the orbital axis were defined relative to the globe-optic nerve junction.

The rectus muscle paths were determined in Plane-1 which lies between 2 to 4 mm anterior to the globe-optic nerve junction, the most anterior plane in which the rectus muscles paths have shown to be stable as gaze varies [31]. This plane is located just a few mm posterior to the region where the sharp inflection (as gaze varies) of the rectus muscles was found in the studies of Clark et al., which is thought to be the functional location of the pulleys [31;33]. Since decompression surgery results in a posterior shift of the globe and the anterior orbital tissues, the anteroposterior location of Plane-1 relative to the orbital bony walls was usually not the same before and after surgery.

The position of the globe center was measured relative to the semi-orbitocentric coordinate system, in the plane corresponding to the center of the globe on the z-axis, usually Plane-6 or Plane-7, i.e. between 12 to 14 mm anterior of the junction. Rectus muscle cross-sectional areas (almost perpendicular to the long axis of the muscle) were determined in Plane+1, between 2 to 4 mm posterior to the junction.

To validate the above method, rectus muscle paths were measured in four control subjects (8 orbits) without ocular pathology. No significant differences (two-tailed t-test according to Satterthwaite [12],  $p > 0.1$ ) were found between the x- and y-positions of the muscle paths thus found and the results in the study by Clarke et al. [31].

Muscle paths were determined in primary position using the above method. To study the stability of muscle paths as a function of gaze, their motion as a function of gaze position was studied. Two-dimensional MRI dynamic color mapping (MRI-DCM) can objectively measure the motion in two-dimensional (2-D) sequences of MRI images employing a gradient optical flow algorithm [7], and has been validated on phantoms [3].

2-D image sequences were extracted from the horizontal and vertical gaze volume sequences in Plane-1 and carefully registered since motion estimation may be confused by head movements [148]. MRI-DCM was then used to determine the motion (in mm/degree of gaze change) of the muscle paths (relative to primary

position) perpendicular to the orbital axis in the sequences. The motion estimates within the boundaries of the muscle tracings (see above) were averaged so that two (one horizontal and one vertical) averages (in mm per degree of gaze change) resulted for the motion of each muscle path as a function of gaze.

### C) Decompression surgery

The different surgical techniques for decompression surgery have been described extensively [88;118;137]. Only those details pertinent to an understanding of their potential effect on rectus extraocular muscle paths are described here. During translid (two-wall) decompression surgery, the periorbital is dissected from the orbital floor and the medial wall. Large osteotomies are then created in the bony orbital floor from the orbital rim as far as the posterior wall of the antral cavity and about halfway up the bony medial wall, from the lacrimal bone to the posterior ethmoidal artery. See Figure 3 (top).

During coronal (bilateral three-wall) decompression surgery, the periorbital is dissected from all four orbital walls up to the apex. Large osteotomies are then created in the bony lateral wall, in the medial wall from the lacrimal bone to the posterior ethmoidal artery, and in the medial part of the bony floor from the lower edge of the lacrimal bone up to about the infraorbital nerve. See Figure 3 (bottom).

The bony strut between inferior and medial wall was usually preserved except in cases of extreme proptosis. In both surgical techniques, the anterior periorbital is incised circumferentially and the posterior periorbital is incised radially to increase herniation of the soft tissues. The osteotomies are usually made as large as circumstances allow, depending on criteria assessed by the surgeon, such as the amount of pre-operative proptosis, and on per-operative accessibility of bony areas and flexibility of intra-orbital tissue.

### D) Masking

The researcher localizing rectus muscle paths (MDA) was masked to orthoptic findings, and the researcher performing orthoptic examination (MELdG) was masked to rectus muscle path findings.

### E) Statistical issues

Averages are presented as mean $\pm$ standard deviation. Rectus muscle path positions were compared with a two-tailed Student's *t* test. Centrifugal displacements are defined as either vertical or horizontal displacements of the muscle path away from the orbital center. The *t* value for multiple comparisons was corrected with the Bonferroni adjustment method [12]. To correlate rectus muscle path displacements to duction and diplopia changes, displacements were computed for each individual patient from the *translid* and *coronal* groups by subtracting the preoperative muscle path x- and y-positions from the postoperative x- and y-positions (in mm). Duction changes ( $\Delta$ ) for each individual patient were computed as the difference between the absolute value of the duction after surgery minus the absolute value of the duction before surgery (in  $^{\circ}$ ). Correlation coefficients (*r*) were computed using

	Before surgery	After surgery	
	(Pooled, n = 30) (°)	translid (n = 10) (°)	coronal (n = 20) (°)
Δ Abduction	39.3±10.5	39.9±9.8	33.6±9.0
Δ Adduction	44.8±6.2	46.8±3.3	44.2±3.9
Δ Elevation	26.2±7.8	24.8±10.7	23.3±8.1
Δ Depression	55.5±6.6	57.5±4.6	56.4±5.1

Table 1. Averaged monocular maximum ductions  $\Delta$  before and after translid and coronal decompression surgery. Maximum ductions in degrees ( $^{\circ}$ ) from primary position. Average maximum ductions that undergo significant ( $p < 0.05$ ) displacements from before to after surgery compared to all pre-operative (both pre-coronal and pre-translid) positions are indicated in gray.

Pearson's product moment correlation function and compared using the statistic

$$t = \sqrt{\frac{n-2}{1-r^2}} [12].$$

Linear regressions were computed using square error minimization. Data analysis was performed using Excel 7.0 (Microsoft Corp, Seattle, WA).

### 3. RESULTS

#### A) Baseline characteristics

The mean age at inclusion was  $48.4 \pm 11.2$  years (*translid group*  $49.2 \pm 12.8$ , *coronal group*  $48.0 \pm 10.7$ ). The mean duration of Graves' orbitopathy before surgery was  $3.4 \pm 3.3$  years (*translid group*  $2.6 \pm 2.2$ , *coronal group*  $3.8 \pm 3.8$ ). 5% of patients were males (*translid group* 14%, *coronal group* 0%). The maximum ductions before and after surgery are given in Table 1.

There were no significant changes from before to after surgery, except for a significant ( $p = 0.04$ ) 5.7 degrees average decrease in maximum abduction after coronal decompression.

The distribution of diplopia changes was: in the *translid-group*, horizontal diplopia: Not Worse 6 (60%), Worse 1 (10%), Much Worse 3 (30%); vertical diplopia: Not Worse 4 (40%), Worse 2 (20%), Much Worse 4 (40%). In the *coronal-group*, horizontal diplopia: Not Worse 5 (25%), Worse 7 (35%), Much Worse 8 (40%); vertical diplopia: Not Worse 16 (80%), Worse 2 (10%), Much Worse 2 (10%).

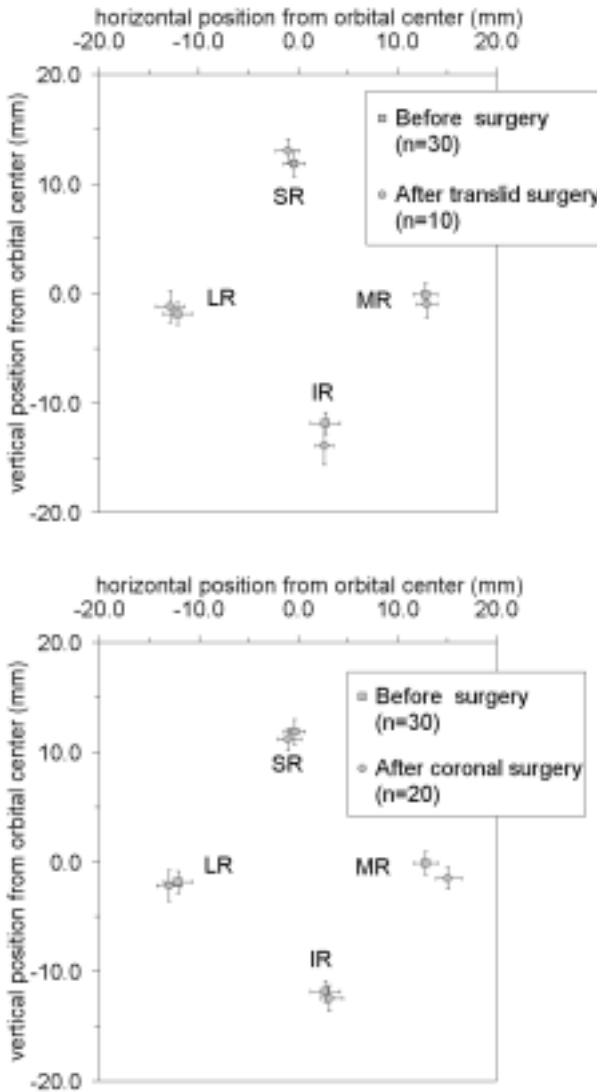


Figure 4. Averaged rectus muscle paths positions in Plane-1. a) (top) before any surgery and after translid decompression surgery. b) (bottom) before any surgery and after coronal decompression surgery. The averaged positions before surgery are the same in a) and b) and have been averaged over all translid and coronal group patients. The positions of the paths 2-4mm anterior to the globe-optic nerve junction (Plane-1), are shown in mm relative to the orbital center and as if facing the subject for a right-sided orbit. Paths for the left orbit have been mirrored. Error bands =  $\pm$  one standard deviation. (squares) preoperative positions; (circles) postoperative positions. SR = superior rectus muscle path, IR = inferior rectus muscle path, LR = lateral rectus muscle path, MR = medial rectus muscle path.

	Before surgery		After surgery			
	(Pooled, n = 30)		<i>p-translid</i> (n = 10)		<i>p-coronal</i> (n = 20)	
	x (mm)	y (mm)	x (mm)	y (mm)	x (mm)	y (mm)
MR	12.8±1.2	-0.1±1.0	13.0±1.0	-1.0±1.2	15.1±1.4	-1.5±1.0
IR	2.8±1.5	-11.8±1.0	2.7±0.9	-13.9±1.7	3.1±1.4	-12.5±1.2
LR	-12.1±2.1	-1.8±1.0	-12.9±1.4	-1.2±1.4	-13.0±1.3	-2.2±1.4
SR	-0.4±0.4	11.8±1.2	-1.0±1.2	13.0±1.1	-1.0±1.3	11.2±1.0

Table 2. Averaged rectus muscle paths positions before and after translid and coronal decompression surgery. Positions in mm relative to orbital center. Average positions that undergo significant ( $p < 0.001$ ) displacements after surgery compared to all pre-operative (both pre-coronal and pre-translid) positions are indicated in gray. MR = medial rectus muscle path, IR = inferior rectus muscle path, LR = lateral rectus muscle pat, SR = superior rectus muscle path.

### B) Path positions and displacements

Path positions were measured in primary position. Averaged x- and y-positions of the rectus muscle paths before and after decompression are summarized in Table 2.

The averaged positions before decompression of all *translid* and *coronal group* patients were not significantly ( $p > 0.15$ ) different from the average positions in normals found in the study by Clark et al. [31]. Nevertheless, the standard deviations of the averages of the *translid* and *coronal group* were larger than the standard deviations in normals. The average positions before decompression of the *translid group* patients were not significantly different from the average positions before decompression of the *coronal group* patients.

There was usually no difference ( $p > 0.1$ ) between the averaged positions of the *translid group* patients before and after decompression surgery, except for a significant ( $p < 0.00005$ ) centrifugal displacement of the inferior rectus muscle path (average displacement 2.1mm). There was also no difference ( $p > 0.1$ ) between the average positions of the *coronal group* patients before and after decompression, except for a significant ( $p < 0.00005$ ) centrifugal displacement of the medial rectus muscle path (average displacement 2.5mm). See Table 2, and Figure 4.

### C) Paths and motility

Correlation coefficients of muscle path displacements with changes in maximum duction and diplopia were determined in the *translid group* (Table 3) and *coronal group* (Table 4) patients. Table 3 shows the correlation coefficients of vertical muscle path displacements with motility changes for the *translid group* patients. There was a significant ( $p < 0.007$ ) positive correlation ( $r = 0.9$ , 95% confidence interval (CI):  $0.74 < r < 0.98$ ) between *increase* of maximum depression and the amount of centrifugal displacement of the inferior rectus muscle path. This

	MR $\delta_y$	IR $\delta_y$	LR $\delta_y$	SR $\delta_y$
$\Delta$ Abduction	0.0	-0.1	-0.3	0.2
$\Delta$ Adduction	0.2	0.7	-0.4	0.4
$\Delta$ Elevation	-0.7	0.0	0.4	0.6
$\Delta$ Depression	0.1	0.9	-0.5	0.6
Horizontal diplopia	0.1	0.1	0.3	-0.2
Vertical diplopia	0.4	0.9	-0.6	0.4

Table 3. Correlation between centrifugal, i.e. from the orbital center outward, vertical muscle path displacement  $\delta_y$  (mm) to increase in maximum duction  $\Delta$  ( $^\circ$ ) and to change in diplopia in the *translid* group.  $n=10$ . A positive correlation means that a centrifugal displacement is correlated to an increase in maximum duction or more diplopia. Significant correlations ( $p \leq 0.05$ ) are shown in black, others in light gray. SR = superior rectus muscle path, IR = inferior rectus muscle path, LR = lateral rectus muscle path, MR = medial rectus muscle path.

relationship is illustrated in the scatter-plot in Figure 5, with a linear regression with  $R^2 = 0.72$  also shown. There was also a significant ( $p < 0.004$ ) positive correlation ( $r = 0.9$ , 95% confidence interval (CI):  $0.79 < r < 0.98$ ) between an increase in vertical *diplopia* and the amount of centrifugal displacement of the inferior rectus muscle path. All other correlations of any displacement with any vertical or horizontal motility changes, and especially with superior rectus displacement and maximum elevation, were not significant ( $p > 0.2$ ) in the *translid* group patients.

Table 4 shows the correlation coefficients of horizontal muscle path displacements with motility changes for the *coronal* group patients. There was a significant ( $p < 0.003$ ) *negative* correlation ( $r = -0.7$ , 95% CI:  $-0.92 < r < -0.43$ ) between increase in maximum abduction and the amount of centrifugal displacement of the medial rectus muscle path.

Thus, a larger displacement correlates with a *decreased* maximum abduction. This relationship is illustrated in Figure 6, with a linear regression with  $R^2 = 0.58$  shown. There was also a significant ( $p < 0.05$ ) positive correlation ( $r = 0.6$ , 95% confidence interval (CI):  $0.14 < r < 0.82$ ) between an increase in horizontal *diplopia* and the amount of centrifugal displacement of the medial rectus muscle path. All other correlations of displacements with vertical and horizontal motility changes, and especially maximum adduction, were not significant ( $p > 0.2$ ) in the *coronal* group patients.

Table 5 shows that rectus muscle cross-sectional areas in Plane+1 did not significantly ( $p > 0.4$ ) change as a result of decompression surgery. The x- and y-coordinates of the center of the globe did not shift significantly relative to the orbital center from before to after surgery ( $p > 0.15$ ) in either groups.

	MR $\delta_x$	IR $\delta_x$	LR $\delta_x$	SR $\delta_x$
$\Delta$ Abduction	-0.7	-0.2	-0.4	0.0
$\Delta$ Adduction	0.0	-0.2	0.5	-0.4
$\Delta$ Elevation	0.3	-0.2	0.5	-0.2
$\Delta$ Depression	0.1	-0.5	0.4	-0.2
Horizontal diplopia	0.6	0.0	0.3	-0.2
Vertical diplopia	-0.2	-0.3	0.3	-0.4

Table 4. Correlation between centrifugal horizontal muscle path displacement  $\delta_x$  (mm) to increase in maximum duction  $\Delta$  ( $^\circ$ ) and to change in diplopia in the coronal group.  $n=20$ . A positive correlation means that a centrifugal displacement is correlated to an increase in maximum duction or more diplopia. Significant correlations ( $p \leq 0.05$ ) are shown in black, others in light gray. SR = superior rectus muscle path, IR = inferior rectus muscle path, LR = lateral rectus muscle path, MR = medial rectus muscle path.

	Before surgery $mm^2$	After surgery $mm^2$
MRM	32.5 $\pm$ 9.1	32.7 $\pm$ 09.1
IRM	20.3 $\pm$ 6.4	21.5 $\pm$ 07.9
LRM	18.5 $\pm$ 3.5	19.7 $\pm$ 04.2
SRM	16.8 $\pm$ 4.3	17.1 $\pm$ 04.7

Table 5. Rectus muscle cross-sectional areas before and after surgery (both *translid* and *coronal* groups). Differences are not significant ( $p > 0.5$ ). SRM = superior rectus muscle, IRM = inferior rectus muscle, LRM = lateral rectus muscle, MRM = medial rectus muscle.

#### D) Path stability as gaze varied

The average motion computed using dynamic color mapping of the rectus muscles in Plane -1 perpendicular to the orbital axis was  $0.25 \pm 0.12$  mm per gaze change of  $8^\circ$ , for all muscle paths, in both *translid* and *coronal* groups, for both horizontal and vertical gaze sequences, and both before and after surgery.

Visual inspection of the sequences showed the motion to be regular over the entire gaze trajectory, without sudden changes at the extremes of gaze.

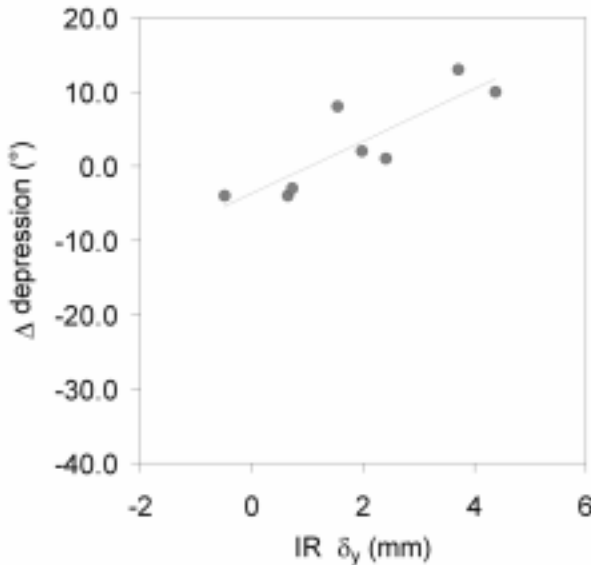


Figure 5. Scatterplot of centrifugal, i.e. from the orbital center outward, vertical displacement of the inferior rectus muscle path IR  $\delta_y$  (mm), resulting from translid decompression versus increase in maximum depression  $\Delta$  ( $^\circ$ ).  $n=10$ . The straight line is a linear regression with least squares  $R^2 = 0.72$ .

#### 4. DISCUSSION

The findings indicate that:

- ◇ anterior rectus muscle path positions in patients with Graves' orbitopathy, with similar restricted motility as the patients in this study, are the same as in normals [31].
- ◇ rectus muscle path stability (as gaze varies) in patients with Graves' orbitopathy, with similar restricted motility as the patients in this study, is the same as in normals [31].
- ◇ rectus muscle path positions are generally unchanged from before to after decompression surgery, with two exceptions. Translid surgery results in an average of 2.1mm centrifugal displacement of the inferior rectus muscle path, and coronal surgery results in an average 2.5mm centrifugal displacement of the medial rectus path.
- ◇ rectus muscle path stability (as gaze varies) is unchanged from before to after decompression surgery.

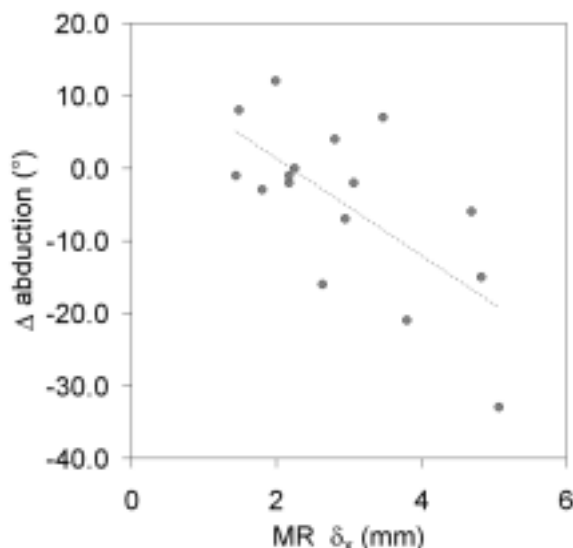


Figure 6. Scatterplot of centrifugal horizontal displacement of the medial rectus muscle path  $MR \delta_x$  (mm), as a result of coronal decompression versus increase in maximum abduction  $\Delta$  ( $^\circ$ ).  $n=20$ . The straight line is a linear regression with least squares  $R^2 = 0.50$ .

- ◆ the amount of centrifugal displacement as measured in the semi-orbitocentric coordinate system (which may lead to less accurate results than measurements in an oculocentric coordinate system, as discussed below) is related to the amount of change of two reasonably objective parameters of ocular motility disturbance: the amount of change of maximum duction and the amount of change of diplopia as a result of decompression surgery.

It can be argued that the displacements are not the effect of surgery, but of measurement errors or the fact that the muscle paths are unchanged in primary position only, and are unstable as gaze varies because of weakened coupling to the orbital walls. Indeed, our method of inferring rectus muscle paths differs from that in the literature, the voxel size in the volumes obtained by this method is larger than that used by Clark et al., and the normalization interpolation may have introduced subtle shifts. However, we have taken great care to validate our method, as mentioned in the methods section, and there were no significant differences between normals positions determined by our and by the method described by Clark et al.

The larger standard deviations compared to Clark's study are probably an effect of the larger and more variable cross-sectional muscle areas due to the

orbitopathy. (The advantage of our method is that patients need to fixate a single target for only 15 seconds, resulting in fewer motion artifacts and less MR noise). Another argument in favor of an effect of surgery is that specifically the muscles closest to the largest osteotomy, i.e., the orbital floor in translid surgery and the medial wall in coronal surgery, were found to have the largest displacements. That the displacements are due to surgery and not an effect of gaze position, caused for example by weakened coupling, is indicated by the results from the MRI-DCM motion study. These indicate that muscle paths both before and after surgery move only relatively slightly as gaze varied. If the motion is assumed to be regular over the whole trajectory, a motion of  $0.25 \pm 0.12$  mm per gaze position correspond to average displacements of  $0.75 \pm 0.36$  mm on abduction ( $24^\circ$ ),  $1.0 \pm 0.48$  mm on adduction ( $40^\circ$ ),  $0.75 \pm 0.36$  mm on elevation ( $24^\circ$ ) and  $0.75 \pm 0.36$  mm on depression ( $24^\circ$ ), which are similar to the displacements found in normals [31].

Our findings indicate that the positions of most rectus muscle paths remain unchanged by decompression surgery. Nevertheless, specific extraocular muscle paths *are* displaced in a specific, centrifugal manner, namely the inferior rectus muscle path after translid surgery and the medial rectus path after coronal surgery. This is not surprising, in view of the close relationship of the involved muscle and its bony support (the orbital floor respectively medial wall) that is removed. It is important to understand that the displacements are relative to the functional center of the orbit. For example, the path of the superior rectus muscle can obviously not be displaced upward as a result of translid surgery since the orbital roof is not removed. However, because the orbital contents are shifted downward, the functional center also shifts downward, and relative to *this* center, the path may be displaced upward in some patients.

How do these specific displacements cause ocular motility disturbances? The findings indicate that the *amount of centrifugal displacement* of a rectus muscle path is related to the amount of specific changes in maximum duction and diplopia after both translid and coronal surgery. The amount of centrifugal displacement of the inferior rectus muscle path was found to be related to an increase in maximum depression and vertical diplopia after translid surgery in each individual patient. Similarly, the amount of centrifugal displacement of the medial rectus muscle path was found to be related to a decrease in maximum abduction and horizontal diplopia after coronal surgery. Because the center of the globe did not shift significantly from before to after surgery, the centrifugal displacement of the anterior path of a muscle results in an increase in the length of its path to the globe to an even larger amount (since the muscle has to 'fold' through the pulley).

The result is an increase in the elastic component of the muscle force, causing either an increased duction in the direction of action of that muscle or a decreased duction in the direction of the antagonist of that muscle. In this regard, the pulley is part of the problem: if the pulley was not there, or more elastic, the path would not have to deviate so much.

Other explanations that have been proposed for the induction of postoperative motility disturbance after decompression surgery include posterior removal of the

ethmoid [110], amount of proptosis reduction [56], preoperative abnormal motility [56;121], activity and severity of Graves' orbitopathy and previous radiotherapy [87]. However, little evidence has been brought forward to support these explanations, and most of the studies were retrospective and based on comparisons of outcome of different surgical techniques. Size and extent of osteotomy, muscle paths and post-surgical muscle displacements were never determined. In a study of 138 patients from the same institution and operated by the same surgeon as the patients in this study, Kalmann et al. were unable to establish any relationship of age, gender, duration of orbitopathy, severity of orbitopathy, previous treatment with steroids, previous treatment with radiotherapy, amount of proptosis reduction or amount of preoperative motility disturbances, of ductions or of diplopia, to newly induced or aggravated diplopia by either coronal or translid decompression surgery [87]. Interestingly, Seiff et al., observed that not incising the anterior periorbita led to a lower incidence of postoperative diplopia [132]. This fits with the mechanism introduced in this study, since the rectus muscle pulleys that determine the muscle paths insert into the anterior periorbita. In another, retrospective, study by Goldberg et al. it was shown that balanced decompression surgery (of the lateral and medial wall) results in less postoperative diplopia than unbalanced decompression surgery (lateral wall only) [68]. The coronal decompression can be thought of as 'balanced' and the translid decompression as 'unbalanced' if the decompression of the floor is discounted. Our findings do not give evidence that the centrifugal displacement of the medial rectus muscle is less with the 'balanced' approach than with the 'unbalanced' approach. However, the osteotomy in the medial wall is much smaller in the translid than in the coronal approach, and in the coronal approach the osteotomy in the lateral wall is much smaller than that in the medial wall. One may, on the basis of our findings, be justified in expecting the centrifugal displacements of the medial and lateral rectus muscles to be of comparable size as a result of balanced decompression surgery and, possibly, a lower frequency of manifest diplopia and ocular muscle imbalances, provided that lateral-and-medial-wall decompression results in lateral and medial osteotomies of comparable size. Other theoretical explanations for duction changes, such as muscle atrophy or hypertrophy are unlikely since the findings indicate that muscle cross-sectional areas do not change as a result of surgery.

In the present study, muscle path positions have been measured in semi-orbitocentric coordinates [31]. The effect of muscle actions is determined by their topographical relation to the (center of the) globe, and an oculocentric coordinate system is expected to be more precise in modeling the effect of muscle path position on ocular motility [33]. For the present study, a semi-orbitocentric coordinate system was chosen to allow comparisons of our results to earlier muscle path studies in normals [31], and because the pulleys stabilize the muscle paths relative to the orbit, so that displacements of these paths should also be measured relative to the orbit. The two coordinate systems do not exclude each other and are, mathematically speaking, dependent.

Theoretically, a postoperative centrifugal displacement of one of the muscle paths could have been accompanied by a shift of the globe center in the same direction – something that could not be detected if only the muscle paths are measured relative to the orbital center – and in that case, the proposed mechanism could not apply. However, the center of the globe was found not to shift significantly as a result of surgery.

In contrast to what might be expected on the basis of the studies by Miller, Demer and others [32;34;95], it is not the postoperative position *per se* of any muscle path, but the surgically induced *displacement* of the path that is related to motility parameters.

It is important to emphasize the implication of the finding that the rectus muscle paths generally remain unchanged from before to after decompression surgery, even though the insertions of the pulleys on the periorbita and orbital wall have been damaged or removed altogether. The implication is that either the anterior connective tissue in the orbit is stable enough to permanently hold the muscle paths in their proper positions, without the direct coupling to the orbital wall or periorbita ever being restored, or the connective tissue is capable of holding the paths in their normal relative positions, long enough for their normal direct attachments to the orbital wall and periorbita to become reinserted, so that direct coupling is reestablished.

This study does not allow one to assert either the first or the second hypothesis, since we have been unable to reliably determine the rectus muscle paths directly after surgery. This was found to be very difficult because MRI scans obtained at this time have low quality due to the edematous orbital tissues, which interferes with the T1 signal from the fat. However, anecdotal evidence suggests that the coupling to the orbital wall may not be very important the ocular motility of these patients was evaluated quite frequently after decompression surgery with cover, duction and prism tests, and no important differences were found between the motility at two weeks and at six months after surgery (Personal communication, MELdG). In either case, the stability indicates that the anterior orbital connective tissue forms a ‘functional skeleton’ of connective tissue that is able to maintain spatial relationships between orbital structures, even without direct coupling to the bony orbit. These findings would seem confirm the observations of Koornneef and Demer et al., that the connective tissue posterior to Tenon’s capsule has sufficient stiffness to maintain spatial relationships among orbital structures [45;94], which may also explain why motility disturbances after decompression surgery do not occur more often.

In conclusion, in the patients in this study, rectus muscle paths were found to be the same in Graves’ orbitopathy as in normals. Decompression surgery was found not to influence the stability of the paths as gaze varies, and was also found not to cause displacements of the paths, except for translid surgery that was found to displace the path of the inferior rectus and coronal surgery that was found to displace the path of the medial rectus muscle to a greater or lesser degree. A

biomechanical mechanism for the motility disturbances caused by decompression surgery may be that the osteotomies cause a centrifugal displacement of the closest rectus muscle path and may so increase the elastic component of the muscle force. Further study in more extensive groups is required to confirm these findings, to see whether it is possible to predict which patients are the most susceptible to centrifugal muscle displacements and whether decompression surgical techniques can be adapted to prevent displacements in the future. Meanwhile, in order to prevent ocular motility disturbances as much as possible, it may be advisable to avoid osteotomies near the locations of the pulleys, not extending them to the orbital rim, and avoid incision of the anterior periorbita (and the posterior periorbita over the muscles).



# 9

## General discussion

The research reported in this thesis had two major aims: to find methods for objective measurement of motion in the orbit, and to determine their application to patients with orbital disorders. The findings of the individual studies are summarized, and implications for our knowledge of the normal orbit and of pathologic conditions of the orbit are discussed.

### 1. SUMMARY OF FINDINGS

#### *A) Chapter 2*

This chapter summarizes the literature on motion measurements in the orbit up to 1997 and shows how objective measurement may lead to clinical applications.

#### *B) Chapter 3*

This chapter gives a precise description of the imaging methods that were used in the remaining chapters of this thesis.

#### *C) Chapter 4*

The findings show that the Lucas and Kanade optical flow algorithm [101] is the most reliable algorithm for determining rotational and translational motion in MR image sequences. The findings also show, for this and similar applications, that Gaussian derivative computation is superior to other methods of derivative computation, such as central differences or the Sobel operator [29;71;143]. Prefiltering by diffusion filtering [124] was found not to improve motion estimations. Sirloin steak phantoms were introduced as an MR model of orbital tissue. Dynamic color mapping was found to be effective for multimodal visualization of optical flow fields, by mapping magnitude and orientation the motion vector combined with the anatomy onto a single pixel.

The findings are in contrast to those by Barron et al. [19], who found that, in real and simulated image sequences of light reflection scenes, the optical flow algorithm by Fleet et al. [59] obtained the most reliable results, while Lucas-

Kanade came in second. This performance difference may be explained by the differences between natural and medical image sequences as discussed in the Introduction, such as partial volume effects and anisotropic phase effects. Optical flow algorithms for radiological motion sequences, e.g. for ultrasound images and tagged-MR images, have been studied by other authors [47;125]. The choice of algorithm to estimate motion from cine MR image sequences has so far been ad hoc [11;165]. The choice of the derivative operator for those algorithms that use derivatives [78;101;153] has also been ad hoc [19]. Isotropic diffusion prefiltering has been shown to actually decrease performance, though it has been advocated by some authors as a means to improve the performance of gradient optical flow algorithms on MR image sequences [11;165].

The findings have established a foundation for future cine MR optical flow studies as far as the alternatives of optical flow algorithm and derivative operator are concerned. The finding that dynamic color mapping is an effective means of rendering the motion field combined with the anatomy may establish this method as an alternative to hedgehog plots [19], or spotnoise mapping [162] in specific applications.

#### *D) Chapter 5*

The findings described in this chapter show that objective measurement of three-dimensional motion from three-dimensional MR sequences by an optical flow algorithm is feasible. The findings also show that the Lucas and Kanade algorithm [101], which has the best performance on two-dimensional MR sequences, can be generalized to three dimensions. The validity of the three-dimensional motion estimates obtained by this algorithm was established for translation, rotation and simulated deformation. Scintillation rendering was found to be effective for the multimodal visualization of three-dimensional motion in conjunction with tissue anatomy.

Other approaches to three-dimensional tissue motion estimation with optical flow algorithms have been described. Song and Leahy [144] found that a three dimensional generalization of Horn and Schunk's [78] algorithm can estimate motion in three-dimensional cine CT sequences of the human heart. They constrained the motion estimates with a model of ventricle wall motion. They have shown the validity of their method employing ultrasound-gel phantoms. However, the results obtained with CT image sequences do not necessarily carry over to MR image sequences (Chapter 4). Hata et al. [75] have generalized Horn and Schunk's algorithm to three dimensions using a global motion smoothness constraint and estimated motion in three-dimensional MR difference images of brain tissue before and during neurosurgery. Their choice of this algorithm is ad hoc, and the use of the global regularity constraint for non-translational motion has been shown to be dubious [19].

Many approaches to visualize three-dimensional motion have been described [17;23;37;81;82;109;160]. All of them involve the visualization of the dynamics of fluids or gases. They were developed to show interesting (at least from a fluid

dynamics point of view) motion features such as vortices and shear. Because the -non-rigid - motion of the tissues in the orbit is largely unknown [96], visualization methods that show a rich set of features are preferable. Lower level features such as the orientation and magnitude of individual motion vectors should be visible. However, a proper visualization method should also allow emergent, i.e., less local, properties of the motion field to be appreciated. Scintillation rendering, a newly developed motion-visualization method, shows the individual motion vectors of small tissue regions in the form of scintillations, but also shows the emergent, larger scale tissue motion as textures. Scintillation rendering could merit further study for the rendering of tissue motion.

#### *E) Chapter 6*

The findings described in this chapter show that objective measurement of motion in the orbit is clinically feasible. The motion of several orbital tissues was measured and expressed in mm per degree of gaze. Objective measurement of motion may be useful for patients with circumscribed pathologies. Similarities of motion were used to differentiate space-occupying lesions. Two tumors could be shown to originate in the rectus muscles and not in the fatty tissue. A biopsy, the alternative to motion measurement, would have entailed a considerable risk to the optic nerve in these patients. It may thus be considered as a useful method of differentiating tumors, as an addition to static MR and CT imaging.

The findings show that motion of orbital tissues is reduced in patients who have undergone enucleation of the globe (in other words, in the anophthalmic socket). They also show that the optic nerve can attach itself to the scleral cover of the baseball implant. This last finding was verified by biopsy. The decreased motion in the anophthalmic socket has previously been described by Ghabrial et al. [65]. However, the study in this chapter is the first to report quantitative results. The attachment of the optic nerve is itself surprising, since promptly after enucleation, it retracts into the apex of the orbit [36]. We suspected that attachment might be related to persistent intractable pain that may occur in rare instances [67]. Nevertheless, this suspicion could not be confirmed and thus far, not much clinical significance has been ascribed to attachment (but see Chapter 7).

#### *F) Chapter 7*

The most important finding was a substrate for the persistent intractable pain that can occur in some patients after enucleation. Persistent intractable pain after enucleation was defined as pain for which no cause can be found by ophthalmic biomicroscopic examination or conventional CT or MR imaging, and which is not treatable by conservative means [67]. The motion of orbital tissues in the anophthalmic sockets of patients who suffer from persistent intractable pain was found to be less than in patients without pain. The optic nerve is almost always attached to the scleral cover of the implant (in patients with and without pain). One or more microscopic amputation neuromas were found in 80% of biopsies of tissue in the vicinity of the implant-optic nerve junction.

Amputation neuromas had been implied by the objective motion measurements, but could not have been diagnosed using current non-invasive methods. In three out of the four patients in which microscopic neuromas had been found, excision led to the resolution of pain. It has been known for quite some time that friction and pressure increase the likelihood of painful amputation neuroma [30;108;158]. Persistent pain in the anophthalmic socket is thought to be relatively rare, and only six cases have been described in the literature [67;112;133]. Only two cases of optic nerve amputation neuroma have been described in the literature [112]. Consequently, Chapter 6 is the most comprehensive study of this syndrome to date, describing ten new patients with persistent and intractable pain and four patients with microscopic amputation neuromas.

The findings suggest a causal relationship between decreased motion, (microscopic) amputation neuroma and persistent intractable pain. This may have implications for enucleation techniques and management of patients with persistent pain after enucleation. It is not unlikely that these findings can explain other cases of intractable pain, since microscopic amputation neuromas in the orbit are not detectable by conventional means, and can only be found indirectly through decreased motion findings. A more extensive prospective study is required to determine whether removal of amputation neuroma will indeed lead to a decrease of pain.

### G) Chapter 8

The findings described in this chapter are not easily grasped at first reading. Concisely, they were the following:

- ◆ anterior rectus muscle path positions in patients with Graves' orbitopathy are the same as in normals;
- ◆ rectus muscle path stability (as gaze varies) in patients with Graves' orbitopathy is the same as in normals;
- ◆ rectus muscle path positions are generally unchanged from before to after decompression surgery, with two exceptions. Translid surgery results in an average of 2.1mm centrifugal displacement of the inferior rectus muscle path, and coronal surgery results in an average 2.5mm centrifugal displacement of the medial rectus path.
- ◆ the amount of centrifugal displacement is related to ocular motility disturbance: the amount of change of maximum duction and the amount of change of diplopia as a result of decompression surgery.

Koornneef [92-94] was the first to show the elaborate fibrous connective tissue system in the orbit, and the connections of the epimysium (sheath) of the rectus muscles to this tissue. He proposed that this extensive network of connective tissue, known as *orbital septa*, limits the motion of the rectus muscles, compartmentalizes the orbit and supports the neurovascular structures [93]. His work was the foundation on which Miller, and later Miller, Demer and coworkers, have erected the rectus muscle *pulley* concept, as the primary function of the

orbital septa [31-34;41-46;113-116;116;117]. Their research, in turn, has shown that specific parts of the anterior connective tissue (the pulleys) coordinate the paths and functional insertions of the rectus muscles. The function of the pulley for the rectus muscles is comparable to that of the trochlea for the superior oblique muscle. These findings have led Dutton to posit the three components of the orbital connective tissue: Tenon's capsule, the anterior orbital suspensory system and the posterior orbital suspensory system [53]. The findings described in this thesis indicate that the anterior orbital suspensory system is not only instrumental in stabilizing the muscle paths relative to the orbital walls [100], but also in stabilizing the muscles with respect to each other and the globe if no attachments to the orbital wall are present.

In other words, it preserves the relationships among the orbital tissues without being attached to another rigid structure (the orbital wall), rather than just functioning as a suspensory system held in place by the bony orbital wall. The pulleys and related tissues must have substantial strength to maintain the position of the muscles after desinsertion from the orbit, as in decompression surgery, and to remain in positions that are amenable to re-insertion during healing [J.L. Miller, personal communication]. The anterior suspensory system apparently functions as a moderately rigid skeleton in its own right.

Koornneef proposed that the orbital septa are important in the pathogenesis and management of Graves' orbitopathy [118]. The findings in Chapter 8 clearly support this notion, but with a twist. Local removal of the orbital wall by osteotomy during decompression surgery may create a centrifugal displacement of the rectus muscle closest to the osteotomy. This displacement was found to be strongly related to postoperative diplopia and postoperative motility disturbances and is a potential biomechanical explanation for the diplopia that may be the result of decompression surgery in some, but not all, patients [49;56;70;87;88;105;110;121;122;130;132;151]. The centrifugal displacement results in an increase in the elastic component of the muscle force similar to stretching [116]. Nevertheless, the more effectively the pulley constrains displacement of the anterior part of the muscle (actually the tendon), the more severe this stretching effect becomes. Thus, the ocular motility disturbances may be explained as an "unexpected" effect of the existence of the pulleys and the connective tissue system: after all, if they had not been present, the ocular motility disturbances would have been less severe.

The results of strabismus surgery for ocular motility disturbances after translid decompression are less good than that for strabismus surgery after coronal decompression [87;130]. The findings described in this thesis indicate that the mechanism for motility disturbances is different for translid (increased depression) compared to coronal (decreased abduction) decompression. Though yet unexplained, these different mechanisms are in line with the different effects of strabismus surgery cited above. Why surgery causes diplopia or other motility disturbances by this mechanism in certain patients but not in others is not yet clear. However, unpublished data suggest that the preoperative volume of the rectus

muscle that is displaced may have predictive value for the development of diplopia and ocular motility disturbances.

The finding subjects warrant further study, so that it may one day be possible to predict and prevent the development of motility disturbances.

## 2. GENERAL DISCUSSION

Usually, the discovery of a new imaging modality leads to a large number of publications that describe how known conditions look using the new modality. Such findings are interesting in themselves, especially if the new modality is cheaper, faster and better than older modalities.

It is even more interesting, however, if the use of a new imaging modality leads to new viewpoints on anatomy or pathology.

A brief digression on the nature of scientific research is appropriate here. The present work is based on two disciplines: orbitology, a branch of ophthalmology, itself a branch of clinical medicine, and imaging science, a branch of computer science. These disciplines are different in their research methods, and even their concept of what constitutes rigorous scientific research is, broadly put, different. In computer science, the most rigorous evidence is a *formal proof*, while in clinical medicine it is a *randomized clinical trial*. This thesis does not give a formal proof of the general correctness of objective motion measurement, nor does it offer the results of a randomized clinical trial as clinical evidence of the benefit of objective motion measurement in the orbit. Accordingly, the most rigorous litmus tests of scientific research have not (yet) been met in either field.

Nevertheless, though there are only a few applications where objective motion measurement has been shown to add value, the present work demonstrates unequivocally that it can lead to new insights. It has cleared the way for the discovery of amputation neuromas in the anophthalmic socket and allowed some orbital tumors to be located more precisely. In addition, the stability of the rectus muscle paths in relation to orbital surgery was described, and a mechanism was found for diplopia that may result from decompression surgery, based on the pulley concept. Further exploration of the clinical use and the limitations of objective measurement of motion in the orbit seem to be worthwhile. Specifically, preventing the centrifugal displacements of the inferior respectively medial rectus muscles after decompression surgery can be determined in future, prospective, studies. In addition, there are some data to support the notion that the pre-operative state of the rectus muscles, especially the muscle volume, may predict the postoperative development of motility disturbances (unpublished data). Though the validation of this technique has not been feasible, the implantation of gold beads in the orbit may lead to validation studies in the near future [J.L. Miller, personal communication].

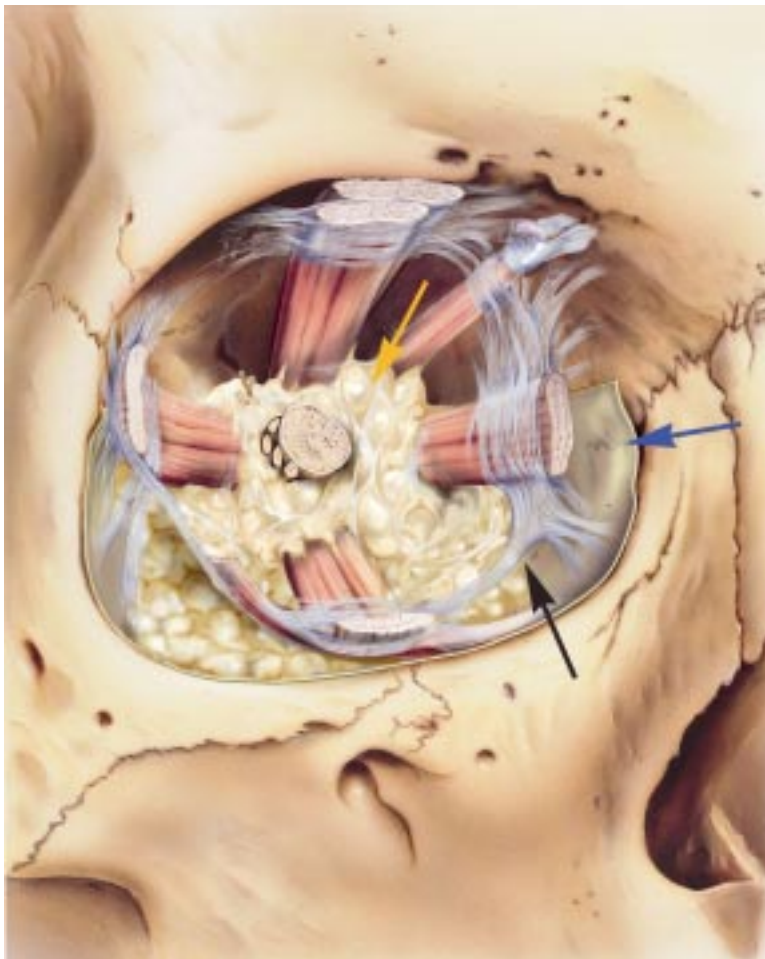


Figure 1. Anatomy of the right orbit, showing the pulleys, the relationships between pulleys, periorbital and the orbital walls, and illustrating some implications of the research in this thesis.

The orbit has been opened, and the globe and Tenon's capsule have been removed. In the superior part of the orbit, the extraconal fat and the periorbital have been removed additionally. The pulleys (*faintly bluish fibers*) insert on the orbital walls *via* the periorbital (*blue arrow*), but are stable because of their interconnections (*black arrow*) even when the pulley insertions are removed from the wall. See Chapter 8. The intraconal fat (*yellow arrow*) has fluid-like behavior, see Chapter 5, even though it is part of the same connective tissue network as the pulleys.

That applications of the 2-D and 3-D tissue motion measurement techniques developed for the present work are not limited to ophthalmology is shown in

cardiology. They are being applied to real-time cardiac wall dyskinesia measurement in collaboration with Prof. Dr. E. Korsten (Technical University of Eindhoven), and objective measurement of tissue motion may find applications in other medical disciplines in the future.

Besides these clinical applications, the findings described in this study, and especially those in Chapter 8, also have implications for the physiology and anatomy of the orbital tissues. The present work made me appreciate the orbital tissues ever more as the *organ of gaze*. See Figure 1. This notion was reinforced by my recent findings of the almost fluid-like three-dimensional motion of the fat within the muscle cone [9]. This finding may indicate that there is a great variety in the role of connective tissue in the orbit: an anterior component that is so rigid as to function as a skeleton, and a posterior component that is so elastic as to behave as a fluid.

An organ is commonly understood to be an anatomical structure that consists of the maximal set of organ parts so connected to one another that they constitute a self-contained unit of macroscopic anatomy, distinct both morphologically and functionally from other such units [1]. It had already been shown by Koornneef and earlier researchers that the orbital tissues have a self-contained macroscopic anatomy which is distinct morphologically from other tissues [94]. The orbital fatty tissue is known to be functionally different from other fatty tissues in the body [38], one of the reasons why Graves' orbitopathy strikes where it does. The findings in Chapter 8 suggest that if even a single structure in the orbital tissues is displaced by only a few millimeters, gaze may be disturbed and ocular motility disturbances develop. All of these findings together suggest that the orbital tissues represent a self-contained unit that allows the eye to gaze, and which does not need the bony orbital walls to function properly.

In short, the orbital tissues can be thought of as the organ of gaze.

# Bibliography

- [1] Anonymous, "Merriam-Webster's collegiate dictionary," available: [www.m-w.com](http://www.m-w.com). 2001.
- [2] Abràmoff, M. D. and Mourits, M. Ph., "Do apical orbital septa play a role in causing strabismus?", *Proc. Annual Meeting American Society Ophthalmic Plastic Reconstructive Surgery*, New Orleans, LA, 1998.
- [3] Abràmoff, M. D., Niessen, W. J., and Viergever, M. A., "Objective quantification of the motion of soft tissues: an application to orbital soft tissue motion", *IEEE Trans Med Imag*, vol. 19, no. 10, pp. 986-995, 2000.
- [4] Abràmoff, M. D., Stuijzfand, E. P., Mali, W. P. T. M., and Mourits, M. Ph., "Rapid kinematic video MR shows reattachment of optic nerve after enucleation [ARVO abstract]", *Invest Ophthalm Vis Sci*, vol. 38, no. 4, pp. 120, 1997.
- [5] Abràmoff, M. D., Stuijzfand, E. P., Mali, W. P. T. M., Mourits, M. Ph., and Zonneveld, F. W., "Reattachments after orbital surgery shown by kinematic MR imaging", *Radiology [RSNA supplement]*, vol. 205 pp. 270-271, 1997.
- [6] Abràmoff, M. D., Stuijzfand, E. P., Ramos, L. M. P., and Mourits, M. Ph., "Quantitative dynamic MRI and orbital fractures [ESOPRS abstract]", *Proc. Conference European Society Plastic Reconstructive Surgery*, Utrecht, pp. 52, 1996.
- [7] Abràmoff, M. D., Van Gils, A. D., Jansen, G. H., and Mourits, M. Ph., "MRI dynamic color mapping: a new quantitative technique for imaging soft tissue motion in the orbit", *Invest Ophthalm Vis Sci*, vol. 41, no. 10, pp. 3256-3260, 2000.
- [8] Abràmoff, M. D., Viergever, M. A., and Mourits, M. Ph., "Recti muscle pulleys and decompression surgery for Graves' orbitopathy [ARVO abstract]", *Invest Ophthalm Vis Sci*, vol. 41, no. 4, pp. 738, 2000.
- [9] Abràmoff, M. D., Völker-Dieben, H. J., Viergever, M. A., and Mourits, M. Ph., "Three-dimensional motion of intraorbital fatty tissue measured with 3-D MRI dynamic color mapping [ARVO abstract]", *Invest Ophthalm Vis Sci*, vol. 42, no. 4, pp. 936, 2001.
- [10] Albert, D. M. and Jakobiec, F. A., *Principles and practice of ophthalmology*, 2nd ed. Philadelphia, PA: Saunders, 2000.
- [11] Amartur, S. C. and Vesselle, H. J., "A new approach to study cardiac motion: the optical flow of cine MR images", *Magn Res Med*, vol. 29, no. 1, pp. 59-67, 1993.
- [12] Armitage, P. and Berry, G., *Statistical methods in medical research*, third ed. Cambridge, MA: Blackwell Science, Inc, 1994.
- [13] Bailey, C. C., Kabala J., Laitt, R., Weston, M., Goddard, P., Hoh, H. B., Potts, M. J., and Harrad, R. A., "Cine magnetic resonance imaging of eye movements", *Eye*, vol. 7 pp. 691-693, 1993.
- [14] Bailey, C. C., Kabala, J., Laitt, R., Goddard, P., Hoh, H. B., Potts, M. J., and Harrad, R. A., "Magnetic resonance imaging in thyroid eye disease", *Eye*, vol. 10 pp. 617-619, 1996.

- [15] Bakker, C. J., Hartkamp, M. J., and Mali, W. P., "Measuring blood flow by nontriggered 2D phase-contrast MR angiography", *Magn Reson Imaging*, vol. 14, no. 6, pp. 609-614, 1996.
- [16] Balla, G. and Depero, F. *Ricostruzione Futurista dell' Universo*. Milan, 1915.
- [17] Banks, D. C., "Illumination in diverse codimensions", *Computer Graphics (Proc SIGGRAPH 1994)*, vol. 28, no. 4, pp. 327-334, 1994.
- [18] Baraldi, P., Sarti, A., Lamberti, C., Prandini, A., and Sgallari, F., "Evaluation of differential optical flow techniques on synthesized echo images", *IEEE Transactions on Biomedical Engineering*, vol. 43, no. 3, pp. 259-272, 1996.
- [19] Barron, J. L., Fleet, D. J., and Beauchemin, S. S., "Performance of optical flow techniques", *Intern J Comput Vis*, vol. 12, no. 1, pp. 43-77, 1994.
- [20] Beauchemin, S. S. and Barron, J. L., "The computation of optical flow", *ACM Computing Surveys*, vol. 27, no. 3, pp. 433-467, 1995.
- [21] Bloom, J. N., Cadera, W., Heiberg, E., and Karlik, S., "A magnetic resonance imaging study of horizontal rectus muscle palsies", *J Pediatr Ophthalmol Strabismus*, vol. 30, no. 5, pp. 296-300, 1993.
- [22] Bloom, J. N., Graviss, E. R., and Mardelli, P. G., "A magnetic resonance imaging study of the upshoot-downshoot phenomenon of Duane's retraction syndrome", *Am J Ophthalmol*, vol. 111, no. 5, pp. 548-554, 1991.
- [23] Brill, M., Hagen, H., Rodrian, H. C., Djatschin, W., and Klimenko, S. V., "Streamball techniques for flow visualization," *IEEE Visualization 94* Washington, DC: IEEE Computer Society Press, pp. 70-76, 1994.
- [24] Burt, P. J. and Adelson, E. H., "The Laplacian Pyramid as a Compact Image Code", *IEEE Trans on Communications*, vol. 31 pp. 532-540, 1983.
- [25] Cabral, B. and Leedom, L., "Imaging vector fields using line integral convolution", *Computer Graphics (Proc SIGGRAPH 1993)*, pp. 263-270, 1993.
- [26] Cadera, W., Karlik, S. J., Viirre, E., and Bloom, J. N., "Ocular pursuit movement assesment by magnetic resonance imaging", *J Pediatr Ophthalmol Strabismus*, vol. 31, no. 4, pp. 265-266, 1994.
- [27] Cadera, W., Viirre, E., and Karlik, S. J., "Cine magnetic resonance imaging of ocular motility", *J Pediatr Ophthalm Strabismus*, vol. 29, no. 2, pp. 120-122, 1992.
- [28] Castelow, D. A., Murray, D. W., Scott, G. L., and Buxton, B. F., "Matching Canny edgels to compute the principal components of optic flow", *Proc. 3rd Alvey Vision Conference*, pp. 193-200, 1987.
- [29] Castleman, K. R., *Digital Image Processing*, Upper Saddle River, NJ: Prentice Hall, 1996.
- [30] Cieslak, A. K. and Stout, A. P., "Traumatic and amputation neuromas", *Arch Surgery*, vol. 53 pp. 646-651, 1946.
- [31] Clark, R. A., Miller, J. M., and Demer, J. L., "Location and stability of rectus muscle pulleys. Muscle paths as a function of gaze", *Invest Ophthalm Vis Sci*, vol. 38, no. 1, pp. 227-240, 1997.
- [32] Clark, R. A., Miller, J. M., and Demer, J. L., "Displacement of the medial rectus pulley in superior oblique palsy", *Invest Ophthalm Vis Sci*, vol. 39, no. 1, pp. 207-212, 1998.
- [33] Clark, R. A., Miller, J. M., and Demer, J. L., "Three-dimensional location of human rectus pulleys by path inflections in secondary gaze positions", *Invest Ophthalm Vis Sci*, vol. 41, no. 12, pp. 3787-3797, 2000.

- [34] Clark, R. A., Miller, J. M., Rosenbaum, A. L., and Demer, J. L., "Heterotopic muscle pulleys or oblique muscle dysfunction?", *JAAPOS*, vol. 2, no. 1, pp. 17-25, 1998.
- [35] Clarke, L., Velthuisen RP, Camacho M.A., Heine J.J., Vaidyanathan M., Hall L.O., Thatcher R.W., and Silbiger M.L., "MRI segmentation: methods and applications", *Magnetic Resonance Imaging*, vol. 13, no. 3, pp. 343-368, 1995.
- [36] Collin, J. R. O., *A Manual of Systematic Eyelid Surgery*, 2 ed. Edinburgh: Churchill Livingstone, pp. 155, 1989.
- [37] Crawfis, R. A. "New techniques for the scientific visualization of three-dimensional multivariate and vector fields", ResearchIndex, available: <http://citeseer.nj.nec.com/crawfis95new.html>, 1995.
- [38] Crisp, M. S., Lane, C., Halliwell, M., Wynford-Thomas, D., and Ludgate, M., "Thyrotropin receptor transcripts in human adipose tissue", *J Clin.Endocrinol.Metab.*, vol. 82, no. 6, pp. 2003-2005, 1997.
- [39] DeAngelis, G. C., Ohzawa, I., and Freeman, R. D., "Receptive-field dynamics in the central visual pathway", *Trends In Neurosciences*, vol. 18, no. 10, pp. 451-458, 1995.
- [40] Del Piano, M., Montino, F., and Occhipinti, P., "Exophthalmus in Graves' disease: luxation of the eyeball at endoscopy", *Endoscopy*, vol. 23, no. 6, pp. 359, 1991.
- [41] Demer, J. L. and Miller, J. E., "Orbital imaging in strabismus surgery," in Rosenbaum, A. L. and Santiago, A. P. (eds.) *Clinical strabismus management* Philadelphia, PA: W.B. Saunders Company, pp. 84-98, 1999.
- [42] Demer, J. L. and Miller, J. M., "Magnetic resonance imaging of the functional anatomy of the superior oblique muscle", *Invest Ophthalm Vis Sci*, vol. 36, no. 5, pp. 906-913, 1995.
- [43] Demer, J. L., Miller, J. M., Koo, E. Y., and Rosenbaum, A. L., "Quantitative magnetic resonance imaging morphometry of extraocular muscles: a new diagnostic tool in paralytic strabismus", *J Pediatr Ophthalmol Strabismus*, vol. 31, no. 3, pp. 177-188, 1994.
- [44] Demer, J. L., Miller, J. M., and Poukens, V., "Surgical implications of the rectus extraocular muscle pulleys", *J Pediatr Ophthalmol Strabismus*, vol. 33, no. 4, pp. 208-218, 1996.
- [45] Demer, J. L., Miller, J. M., Poukens, V., Vinters, H. V., and Glasgow, B. J., "Evidence for fibromuscular pulleys of the recti extraocular muscles", *Invest Ophthalm Vis Sci*, vol. 36, no. 6, pp. 1125-1136, 1995.
- [46] Demer, J. L., Poukens, V., Miller, J. M., and Micevych, P., "Innervation of extraocular pulley smooth muscle in monkeys and humans", *Invest Ophthalm Vis Sci*, vol. 38, no. 9, pp. 1774-1785, 1997.
- [47] Denney, T. S. and Prince, J. L., "A frequency domain performance analysis of Horn and Schunk's optical flow algorithm for deformable motion", *IEEE Trans Imag Process*, vol. 4, no. 9, pp. 1324-1328, 2000.
- [48] deWaard, R., Koornneef, L., and Verbeeten, B., "Motility disturbances in Graves' orbitopathy", *Doc Ophthalmol*, vol. 56 pp. 41-47, 1983.
- [49] Dixon, R. and Lesser, G. R., "The effect of anterior orbital decompression on motility in thyroid exophthalmos", *Ophthalmic Surg*, vol. 12, no. 12, pp. 905-910, 1981.
- [50] Dooley, D. and Cohen, M. F., "Automatic Illustration of 3D Geometric Models: Lines", *Computer Graphics*, vol. 24, no. 2, pp. 77-82, 1990.
- [51] Dougherty, L., Asmuth, J. C., Blom, A. S., Axel, L., and Kumar, R., "Validation of an optical flow method for tag displacement estimation", *IEEE Trans Med Imag*, vol. 18, no. 4, pp. 359-363, 1999.

- [52] Drangova, M., Zhu, Y., Bowman, B., and Pelc, N. J., "In vitro verification of myocardial motion tracking from phase-contrast velocity data", *Magn Reson Imag*, vol. 16, no. 8, pp. 863-870, 1998.
- [53] Dutton, J. J., *Clinical and surgical orbital anatomy*, Philadelphia, PA: WB Saunders Company, 1994.
- [54] Emerson, R. C., Bergen, J. R., and Adelson, E. H., "Directionally selective complex cells and the computation of motion energy in cat visual cortex", *Vis Res*, vol. 32, no. 2, pp. 203-218, 2001.
- [55] Ettl, A., Kramer, J., Daxer, A., and Koornneef, L., "High resolution magnetic resonance imaging of neurovascular orbital anatomy", *Ophthalmology*, vol. 104, no. 5, pp. 869-877, 1997.
- [56] Fatourechi, V., Bergstralh, E. J., Garrity, J. A., Bartley, G. B., Beatty, C. W., Offord, K. P., and Gorman, C. A., "Predictors of response to transantral orbital decompression in severe Graves' ophthalmopathy", *Mayo Clin Proc*, vol. 69, no. 9, pp. 841-848, 1994.
- [57] Fells, P., Kousoulides, L., Pappa, A., Munro, P., and Lawson, J., "Extraocular muscle problems in thyroid eye disease", *Eye*, vol. 8 pp. 497-505, 1994.
- [58] Fleet, D. J. and Jepson, A. D., "Hierarchical construction of orientation and velocity selective filters", *IEEE Trans Patt Anal Mach Intell*, vol. 11, no. 3, pp. 315-325, 1989.
- [59] Fleet, D. J. and Jepson, A. D., "Computation of component image velocity from local phase information", *Intern J Comput Vis*, vol. 5, no. 1, pp. 77-104, 1990.
- [60] Florack, L., Niessen, W., and Nielsen, M., "The intrinsic structure of optic flow incorporating measurement duality", *Intern J Comput Vis*, vol. 27, no. 3, pp. 263-286, 1998.
- [61] Foley, J. D., van Dam, A., Feiner, S. K., and Hughes, J. F., *Computer Graphics - principles and practice*, 2nd ed. Reading, Massachusetts: Addison Wesley, 1990.
- [62] Frangi, A. F., Niessen, W. J., and Viergever, M. A., "Three-dimensional modeling for functional analysis of cardiac images: a review", *IEEE Trans Med Imaging*, vol. 20, no. 1, pp. 2-25, 2001.
- [63] Garrity, J. A., Fatourechi, V., Bergstralh, E. J., Bartley, G. B., Beatty, C. W., DeSanto, L. W., and Gorman, C. A., "Results of transantral orbital decompression in 428 patients with severe Graves' ophthalmopathy", *Am J Ophthalmol*, vol. 116, no. 5, pp. 533-547, 1993.
- [64] Gentry, L. R., "Anatomy of the orbit", *Neuroimag Clin*, vol. 8, no. 1, pp. 171-194, 1998.
- [65] Ghabrial, R., Potts, M. J., Harrad, R. A., Hunter, J., Kabala, J., and Macey, D., "Assessment of the anophthalmic socket with dynamic cine-MRI", *Orbit*, vol. 16, no. 3, pp. 207-216, 1997.
- [66] Gibson, J. J., *The perception of the visual world*, Boston: Houghton-Mifflin, 1950.
- [67] Glatt, H. J., Googe, P. B., Powers, T., and Apple, D. J., "Anophthalmic socket pain", *Am J Ophthalmol*, vol. 116, no. 3, pp. 357-362, 1993.
- [68] Goldberg, R. A., Perry, J. D., Hortaleza, V., and Torre, V., "Strabismus after balanced medial plus lateral versus lateral wall only orbital decompression for dysthyroid orbitopathy", *Ophthal Plast Reconstr Surg*, vol. 16, no. 4, pp. 271-274, 2000.
- [69] Goldberg, R. A., Wu, J. C., Jesmanowicz, A., and Hyde, J. S., "Eyelid anatomy revisited - dynamic high-resolution MRI images of Whitnall's ligament and upper eyelid structures with the use of a surface coil", *Arch Ophthalmology*, vol. 110 pp. 1598-1600, 1992.
- [70] Goldberg, S. H., Bullock, J. D., and Guyton, D. L., "Esotropia following bilateral lateral orbital decompressions for Graves' disease", *Ophthal Plast Reconstr Surg*, vol. 6, no. 3, pp. 190-192, 1990.

- [71] Gonzales, R. C. and Woods, R. E., *Digital Image Processing*, Reading, MA: Addison-Wesley, Inc., 1992.
- [72] Gorce, J. M., Friboulet, D., and Magnin, I. E., "Estimation of three-dimensional cardiac velocity fields: assessment of a differential method and application to three-dimensional CT data", *Med Image Anal*, vol. 1, no. 3, pp. 245-261, 1997.
- [73] Graves, R. J., "Clinical lectures", *London Med Surg J*, vol. 7 pp. 513-520, 1835.
- [74] Hall, P., "Volume rendering for vector fields", *Vis Computer*, vol. 10 pp. 69-78, 1993.
- [75] Hata, N., Nabavi, A., Wells, W. M., Warfield, S. K., Kikinis, R., Black, P. M., and Jolesz, F. A., "Three-dimensional optical flow method for measurement of volumetric brain deformation from intraoperative MR images", *J Comput Assist Tomogr*, vol. 24, no. 4, pp. 531-538, 2000.
- [76] Heeger, D. J., "Optical flow using spatiotemporal filters", *Intern J Comput Vis*, vol. 1 pp. 279-302, 1988.
- [77] Hildreth, E. C., "Computations underlying the measurement of visual motion", *Artificial Intelligence*, vol. 23, no. 3, pp. 309-354, 1983.
- [78] Horn, B. K. P. and Schunk, B. G., "Determining optical flow", *Artificial Intelligence*, vol. 17 pp. 185-204, 1981.
- [79] Hubel, D. H. and Wiesel, T. N., "Receptive fields, binocular interaction, and functional architecture in the cat's visual cortex", *J Physiol*, vol. 160 pp. 106-154, 1962.
- [80] Ingels, N. B., Daughters, G. T., Stinson, E. B., and Alderman, E. L., "Evaluation of methods for quantitating left ventricular segmental wall motion in man using myocardial markers as a standard", *Circulation*, vol. 61, no. 5, pp. 966-972, 1980.
- [81] Interrante, V. and Grosch, Ch., "Strategies for effectively visualizing 3D flow with volume LIC", *Proceedings of IEEE Visualization '97*, Phoenix, AZ, pp. 421-424, 1997.
- [82] Interrante, V. and Grosch, Ch., "Visualizing 3D flow", *IEEE Computer Graphics and Applications*, vol. 18, no. 4, pp. 49-53, 1997.
- [83] Jacobson, D. H. and Gorman, C. A., "Endocrine ophthalmopathy: current ideas concerning etiology, pathogenesis and treatment", *Endocrine Reviews*, vol. 5, no. 2, pp. 200-220, 1984.
- [84] Jaeger, L., Welge-Lussen, U., Lanzl, I., and Reiser, M., "Imaging of eye movement with fast MRI", *J Comput Assist Tomogr*, vol. 21, no. 3, pp. 447-451, 1997.
- [85] Jewell, F. M., Laitt, R. D., Bailey, C. C., Wakeley, C. J., Potts, M. J., Harrad, R. J., Weston, M., Kabala, J., and Goddard, P., "Video loop MRI of ocular motility disorders", *J Comput Assist Tomogr*, vol. 19, no. 1, pp. 39-43, 1995.
- [86] Johnston, A., McOwan, P. W., and Buxton, H., "A computational model of the analysis of some first- and second-order motion patterns by simple and complex cells", *Proc.R Soc Lond B*, vol. 250 pp. 297-306, 1992.
- [87] Kalmann, R., *Graves' orbitopathy, new insights*, Utrecht, the Netherlands: Kalmann, 2001.
- [88] Kalmann, R., Mourits, M. P., van der Pol, J. P., and Koornneef, L., "Coronal approach for rehabilitative orbital decompression in Graves' ophthalmopathy", *Br J Ophthalmol*, vol. 81, no. 1, pp. 41-45, 1997.
- [89] Koenderink, J. J., "Optic flow", *Vis Res*, vol. 26, no. 1, pp. 161-180, 1986.
- [90] Koenderink, J. J., "Relief: pictorial and otherwise", *Image and Vision Computing*, vol. 13, no. 5, pp. 321-334, 1995.

- [91] Koenderink, J. J. and Doorn, A. J., "Invariant properties of the motion parallax field due to the movement of rigid bodies relative to an observer", *Optica Acta*, vol. 22, no. 9, pp. 773-791, 1975.
- [92] Koornneef, L., "New insights into human orbital connective tissue", *Arch Ophthalmol*, vol. 95 pp. 1269-1276, 1977.
- [93] Koornneef, L., *Spatial aspects of orbital musculo-fibrous tissue in man*, First ed. Amsterdam and Lisse: Swets & Zeitlinger, 1977.
- [94] Koornneef, L., "Orbital septa: anatomy and function", *Ophthalmology*, vol. 86 pp. 876-880, 1979.
- [95] Krzizok, T., Kaufmann, H., and Traupe, H., "New approach in strabismus surgery in high myopia", *Br J Ophthalmol*, vol. 81 pp. 625-630, 1997.
- [96] Lasudry, J. G. H., Lemke, B. N., Gentry, L. R., and Sires, B. S., "Multipositional high-resolution imaging of the human orbit's functional anatomy", *Orbit*, vol. 16, no. 3, pp. 159-184, 1997.
- [97] Lawton, D. T., "Processing translational motion sequences", *Computer Vision, Graphics, and Image Proc*, vol. 22 pp. 116-144, 1983.
- [98] Levoy, M., "Display of surfaces from volume data", *Computer Graphics and Applications*, vol. 8, no. 3, pp. 29-37, 1988.
- [99] Lichtenbelt, B., Crane, R., and Naqvi, S., *Introduction to Volume Rendering*, Upper Saddle River, NJ: Prentice Hall Technical Library, 1998.
- [100] Liew, S., Poole, M., Kenton-Smith, J., and Tan, S., "Orbital and globe rotation: the role of the periorbita", *J Craniomaxillofac Surg.*, vol. 27, no. 1, pp. 7-10, 1999.
- [101] Lucas, B. and Kanade, T., "An iterative image registration technique with an application to stereo vision", *Proc. DARPA Image Understanding Workshop*, Washington, DC, pp. 121-130, 1981.
- [102] Lyons, C. J. and Rootman, J., "Orbital decompression for disfiguring exophthalmos in thyroid orbitopathy", *Ophthalmology*, vol. 101, no. 2, pp. 223-230, 1994.
- [103] MacEwen, C. J., "Myopes, squints and scans", *Br J Ophthalmol*, vol. 81 pp. 617-619, 1997.
- [104] Mailloux, G. E., Langlois, F., Simard, P. Y., and Bertrand M., "Restoration of the velocity field of the heart from two-dimensional echocardiograms", *IEEE Trans Med Imag*, vol. 8, no. 2, pp. 143-153, 1999.
- [105] Mann, W. J., Kahaly, G. J., Pitz, S., Bumb, P., Muller-Forell, W., Krummenauer, F., Goerzen, N., Mewes, T., and Pfeiffer, N., "Decompression surgery for thyroid-associated orbitopathy--a ten year experience", *Exp Clin Endocrinol.Diabetes*, vol. 107 Suppl 5 pp. S212-S213, 1999.
- [106] Marr, D. and Hildreth, E. C., "Theory of edge detection", *Proc.R Soc Lond B*, vol. 207 pp. 187-217, 1980.
- [107] Marr, D. and Ullman, S., "Directional selectivity and its use in early visual processing", *Proc.R Soc Lond B*, vol. 211 pp. 150-180, 1981.
- [108] Mathews, G. J. and Osterholm, J. L., "Painful traumatic neuromas", *Surg Clin North Am*, vol. 51 pp. 1313-1324, 1972.
- [109] Max, N., Crawfis, R., and Grant, C., "Visualizing 3D velocity fields near contour surfaces," *IEEE Visualization 94* Washington, DC: IEEE Computer Society Press, pp. 248-255, 1994.
- [110] McCord, J. J., "Current trends in orbital decompression", *Ophthalmology*, vol. 92 pp. 21-33, 1985.

- [111] Mehta, A. M. and Demer, J. L., "Magnetic resonance imaging of the superior oblique muscle in superior oblique myokymia", *J Pediatr Ophthalmol Strabismus*, no. 31, pp. 378-383, 1994.
- [112] Messmer, E. P., Camara, J., Boniuk, M., and Font, R. L., "Amputation neuroma of the orbit. Report of two cases and review of the literature", *Ophthalmology*, vol. 91, no. 11, pp. 1420-1423, 1984.
- [113] Miller, J. M., "Functional anatomy of normal human rectus muscles", *Vis Res*, vol. 29 pp. 223-240, 1989.
- [114] Miller, J. M. and Demer, J. L., "Biomechanical analysis of strabismus", *Binocular Vision and Eye Muscle Surgery Quarterly*, vol. 7, no. 4, pp. 233-248, 1989.
- [115] Miller, J. M., Demer, J. L., and Rosenbaum, A. L., "Effect of transposition surgery on rectus muscle paths by magnetic resonance imaging", *Ophthalmology*, vol. 100, no. 4, pp. 475-487, 1993.
- [116] Miller, J. M. and Robins, D., "Extraocular muscle forces in alert monkey", *Vis Res*, vol. 32, no. 6, pp. 1099-1113, 1992.
- [117] Miller, J. M. and Shamaeva, I. "Orbit gaze mechanics simulation." Version 1.6. Distributed by: Eidactics, #404, 1450 Greenwich Street, San Francisco, California 94109, 1996.
- [118] Mourits, M. P., Koornneef, L., Wiersinga, W. M., Prummel, M. F., Berghout, A., and van der Gaag, R., "Orbital decompression for Graves' ophthalmopathy by inferomedial, by inferomedial plus lateral, and by coronal approach", *Ophthalmology*, vol. 97, no. 5, pp. 636-641, 1990.
- [119] Mourits, M. P., Prummel, M. F., Wiersinga, W. M., and Koornneef, L., "Measuring eye movements in Graves' ophthalmopathy", *Ophthalmology*, vol. 101, no. 8, pp. 1341-1346, 1994.
- [120] Niessen, W. J., Duncan, J. S., Nielsen, M., Florack, L. M. J., ter Haar Romeny, B. M., and Vierger, M. A., "A multiscale approach to image sequence analysis", *Comput Vis Imag Understand*, vol. 65, no. 2, pp. 259-268, 1997.
- [121] Nunery, W. R., Nunery, C. W., Martin, R. T., Truong, T. V., and Osborn, D. R., "The risk of diplopia following orbital floor and medial wall decompression in subtypes of ophthalmic Graves' disease", *Ophthal Plast Reconstr Surg*, vol. 13, no. 3, pp. 153-160, 1997.
- [122] Paridaens, D., Hans, K., van Buitenen, S., and Mourits, M. P., "The incidence of diplopia following coronal and translid orbital decompression in Graves' orbitopathy", *Eye*, vol. 12 ( Pt 5) pp. 800-805, 1998.
- [123] Pelc, N. J., Herfkens, R. J., Shimakawa, A., and Enzmann, D. R., "Phase contrast cine magnetic resonance imaging", *Magn Reson.Q*, vol. 7, no. 4, pp. 229-254, 1991.
- [124] Perona, P. and Malik, J., "Scale space and edge detection using anisotropic diffusion", *IEEE Trans Pattern Anal Mach Intell*, vol. 12, no. 7, pp. 629-631, 1990.
- [125] Prince, J. L., Gupta, S. N., and Osman, N. F., "Bandpass optical flow for tagged MRI", *Med Phys*, vol. 27, no. 1, pp. 108-118, 2000.
- [126] Quaia, C. and Optican, L. M., "Commutative saccadic generator is sufficient to control a 3-D ocular plant with pulleys", *J Neurophysiol*, vol. 79, no. 6, pp. 3197-3215, 1998.
- [127] Raphan, T., "Modeling control of eye orientation in three dimensions. I. Role of muscle pulleys in determining saccadic trajectory", *J Neurophysiol*, vol. 79, no. 5, pp. 2653-2667, 1998.
- [128] Rootman, J., *Diseases of the Orbit: a Multidisciplinary Approach*, Philadelphia, PA: JB Lippincott, 1988.
- [129] Rootman, J., Stewart, B., and Goldberg, R. A., *Orbital Surgery - A Conceptual Approach*, Philadelphia, PA: Lippincott-Raven, 1995.

- [130] Ruttum, M. S., "Effect of prior orbital decompression on outcome of strabismus surgery in patients with thyroid ophthalmopathy", *J AAPOS*, vol. 4, no. 2, pp. 102-105, 2000.
- [131] Scheiber, C., Speeg-Schatz, C., and Chambron, J., "Technique for MRI of ocular motility", *J Comput Assist Tomogr*, vol. 21, no. 3, pp. 442-446, 1997.
- [132] Seiff, S. R., Tovilla, J. L., Carter, S. R., and Choo, P. H., "Modified orbital decompression for dysthyroid orbitopathy", *Ophthal Plast Reconstr Surg*, vol. 16, no. 1, pp. 62-66, 2000.
- [133] Shah-Desai, S. D., Tyers, A. G., and Manners, R. M., "Painful blind eye: efficacy of enucleation and evisceration in resolving ocular pain", *Br J Ophthalmol*, vol. 84, no. 4, pp. 437-438, 2000.
- [134] Sheehan, F. T., Zajac, F. E., and Drace, J. E., "Using cine phase contrast magnetic resonance imaging to non-invasively study in vivo knee dynamics", *J Biomech.*, vol. 31, no. 1, pp. 21-26, 1998.
- [135] Shin, G. C. and Rosenbaum, A. L., "High resolution, dynamic magnetic resonance imaging in complicated strabismus", *J Pediatr Ophthalmol Strabismus*, vol. 33 pp. 282-290, 1996.
- [136] Shorr, N. and Stuart, R. S., "Pathogenesis of Graves' ophthalmopathy", *New Engl J Medicine*, vol. 329, no. 20, pp. 1468-1475, 1993.
- [137] Shorr, N. and Stuart, R. S., "The four stages of surgical rehabilitation of the patient with dysthyroid ophthalmopathy", *Ophthalmology*, vol. 93, no. 4, pp. 477-483, 1986.
- [138] Simoncelli, E. P., Adelson, E. H., and Heeger, D. J., "Probability distributions of optical flow", Maui, Hawaii, pp. 310-315, 1991.
- [139] Simonsz, H. J., Harting, F., DeWaal, B. J., and Verbeeten, B. M. W. J., "Sideways displacement and curve path of recti eye-muscles", *Arch Ophthalmol*, vol. 103 pp. 124-128, 1985.
- [140] Singh, A., "An estimation-theoretic framework for image-flow computation", Proc. 3rd Intern Conf Comput Vis, Osaka, pp. 168-177, 1990.
- [141] Smiddy, W. E., Michels, R. G., and Kumar, A. J., "Magnetic resonance imaging of retrobulbar changes in optic nerve position with eye movement", *Am J Ophthalmology*, vol. 107, no. 1, pp. 82-83, 1989.
- [142] Smit, T. J., Koornneef, L., Groet, E., Zonneveld, F. W., and Otto, A. J., "Prosthesis motility with and without intraorbital implants in the anophthalmic socket", *Br.J.Ophthalmol.*, vol. 75, no. 11, pp. 667-670, 1991.
- [143] Sobel, I. "An isotropic 3x3x3 volume gradient operator", Available: [flash.math.fsu.edu/~erlebach/courses/sciviz/papers/volumetric\\_papers/PAPERS/SOBEL/SOBELE3D.HTM](http://flash.math.fsu.edu/~erlebach/courses/sciviz/papers/volumetric_papers/PAPERS/SOBEL/SOBELE3D.HTM), 1996.
- [144] Song, S. M. and Leahy, R. M., "Computation of 3-D velocity fields from 3-D cine CT images of a human heart", *IEEE Trans Med Imag*, vol. 10, no. 3, pp. 295-306, 1991.
- [145] Stuijzfand, E. P., Abràmoff, M. D., Mali, W. P. T. M., and Mourits, M. Ph., "Rapid quantitative Dynamic Video MR of the orbit [ARVO abstract]", *Inv Ophthalm Vis Sci*, vol. 38, no. 4, pp. 123, 1997.
- [146] Stuijzfand, E. P., Abràmoff, M. D., Zuijderveld, K. J., Ramos, L. M. P., Weickert, J., Mourits, M. Ph., Zonneveld, F. W., and Mali, W. P. T. M. "Fast cinematic magnetic resonance imaging of the eye and orbit", *Electr J Radiol Soc N Amer*, available: [http://ej.rsna.org/EJ\\_0\\_96/0032-97.fin/ej0032-97.html](http://ej.rsna.org/EJ_0_96/0032-97.fin/ej0032-97.html). 1997.
- [147] Sutula, F. C. and Weiter, J. J., "Orbital socket pain after injury", *Am J Ophthalmol*, vol. 90, no. 5, pp. 692-696, 1980.

- [148] Thévenaz, P., Ruttimann, U. E., and Unser, M., "A pyramid approach to subpixel registration based on intensity", *IEEE Transactions on Image Processing*, vol. 7, no. 1, pp. 27-41, 1998.
- [149] Thompson, B. and Barnard S.T., "Lower level estimation and interpretation of visual motion", *Computer*, vol. 14 pp. 20-28, 1981.
- [150] Totsuka, N. K. R., "Kinematic magnetic resonance imaging of orbital blow-out fracture with restricted ocular movement", *Orbit*, vol. 16, no. 2, pp. 75-83, 1997.
- [151] Trokel, St. L. C. W. C., "Orbital decompression: effect on motility and globe position", *Ophthalmology*, vol. 86 pp. 2064-2070, 1979.
- [152] Ullman, S., "Analysis of visual motion by biological and computer systems", *IEEE Transactions on Computer*, vol. 14, no. 8, pp. 57-69, 1981.
- [153] Uras, S., Giroso, F., Verri, A., and Torre, V., "A computational approach to motion perception", *Biol Cybern*, vol. 60 pp. 79-87, 1988.
- [154] van den Elsen, P. A., Maintz, J. B. A., Pol, E. J. D., and Viergever, M. A., "Medical Image Matching -- a Review with Classification", *IEEE Engineering in Medicine and Biology*, vol. 12, no. 1, pp. 26-39, 1993.
- [155] van Rijn, L. J. and van den Berg, A. V., "Binocular eye orientation during fixations: Listing's law extended to include eye vergence", *Vision Res.*, vol. 33, no. 5-6, pp. 691-708, 1993.
- [156] von Noorden, G. K., *Binocular vision and ocular motility. Theory and management of strabismus*, 5th ed. St Louis, MO: Mosby-Yearbook, 1996.
- [157] Wall, J. R. H. J., *Graves' ophthalmopathy*, Boston: Blackwell Scientific Publications, 1990.
- [158] Wall, P. D. and Gutnick, M., "Ongoing activity in peripheral nerves: the physiology and pharmacology of impulses originating from a neuroma", *Exp Neurology*, vol. 43 pp. 580-593, 1974.
- [159] Waterman, H., Leatherbarrow, B., Slater, R., Waterman, C., and Hillier, V., "The hydroxyapatite orbital implant: post-operative pain", *Eye*, vol. 12 ( Pt 6) pp. 996-1000, 1998.
- [160] Wijk, J. J. v., Hin, A. J. S., de Leeuw, W. C., and Post, F. H., "Three ways to show 3D fluid flow", *IEEE Computer Graphics and Applications*, vol. 14, no. 5, pp. 33-39, 1994.
- [161] Wijk, J. J. v., "Spot noise - texture synthesis for data visualization. ", *Computer Graphics (Proc SIGGRAPH 1991)*, vol. 25, no. 4, pp. 309-318, 1991.
- [162] Wijk, J. J. v., "Beyond the arrow plot - new methods for flow visualization", *ElectronicsCooling*, vol. 5, no. 1, pp. 30-34, 2000.
- [163] Yarbus, A. L., "Eye movements during perception of complex objects," *Eye movements and vision*, NY: Plenum Press, pp. 171-196,1967.
- [164] Zerhouni, E. A., Parish, D. M., Rogers, W. J., Yang, A., and Shapiro, E. P., "Human heart: tagging with MR imaging--a method for noninvasive assessment of myocardial motion", *Radiology*, vol. 169, no. 1, pp. 59-63, 1988.
- [165] Zientara, G. P., Saiviroonporn, P., Morrison, P. R., Fried, M. P., Hushek, S. G., Kikinis, R., and Jolesz, F. A., "MRI monitoring of laser ablation using optical flow", *J Magn Resonance Imag*, vol. 8, no. 6, pp. 1306-1318, 1998..

## Samenvatting

Het onderzoek dat in dit proefschrift beschreven wordt had twee belangrijke doelstellingen: het bepalen van een manier om objectief de beweging van weefsels in de oogkas te meten, en het bepalen van het klinische nut van dergelijke metingen. Dit betekende dat een aantal vragen op het gebied van de beeldverwerking alsook op het gebied van de oogheelkunde diende te worden beantwoord.

De resultaten van de studie laten zien dat objectieve meting van de twee- en driedimensionale beweging in de oogkas mogelijk is. De beweging in de oogkas kan twee- en driedimensionaal worden afgebeeld door middel van snelle Magnetic Resonance Imaging (MRI). De beweging in MRI beelden kan objectief worden berekend door middel van optische stroom (optical flow) methoden. Eerste orde locale gradient optische stroom berekeningen verdienen hierbij de voorkeur voor het berekenen van de beweging. Verder is een aantal technieken ontwikkeld om de twee- en driedimensionale beweging te visualiseren. Het gebruik van kleuren blijkt effectief te kunnen zijn bij het afbeelden van beweging, met name in de driedimensionale ruimte.

Uit een tweetal studies bij patiënten is gebleken dat objectieve meting van de beweging in de oogkas van nut kan zijn bij bepaalde ziektebeelden. Op basis van bewegingsmetingen is een verklaring gevonden voor onophoudelijke pijn die soms ontstaat na verwijdering van de oogbol en waarvoor tot op heden nog geen oorzaak bekend was. Daarnaast zijn bewegingsmetingen van nut gebleken bij het diagnostiseren van bepaalde oogkstumoren.

Tevens is aangetoond dat de plaats in de oogkas van de oogspieren en de spierglijders (*pulleys*) meestal hetzelfde is bij lijdende aan de oogkasziekte van Graves' en bij gezonde proefpersonen. Ook na heelkundige verruiming van de oogkas voor deze ziekte verplaatsen de meeste spieren en hun glijders zich niet. Er is een mogelijke verklaring gevonden voor het dubbelzien dat soms na oogkasverruiming optreedt: door de oogkasverruiming verplaatsen bepaalde oogspierglijders wel, waardoor de bijbehorende oogspier wordt uitgerekt en dubbelzien ontstaat. Vooral deze laatste vondsten hebben geleid tot een idee dat centraal staat in dit proefschrift, namelijk dat de weefsels in de oogkas een orgaan vormen, het blik-orgaan.

## Opbouw

*Hoofdstuk 1*, de introductie, beschrijft de motivatie voor dit onderzoek. *Hoofdstuk 2* is een overzicht van de literatuur tot 1997 betreffende de stand van wetenschap van de functionele anatomie van de oogkas. *Hoofdstuk 3* beschrijft de magnetische resonantie (MR) afbeeldingstechnieken die voor dit onderzoek zijn ontwikkeld en gebruikt, en hoe deze voor patiënten zo comfortabel mogelijk zijn gemaakt. *Hoofdstuk 4* beschrijft een onderzoek naar de beste optische stroom rekenmethode voor het bepalen van de beweging in bewegende beelden van de oogkas, laat de betrouwbaarheid van deze methode zien bij bewegings-simulaties, bij simulaties met bewegend weefsel en bij beweging in de oogkas, en beschrijft een nieuwe manier om de beweging zo begrijpelijk mogelijk te visualiseren.

*Hoofdstuk 5* beschrijft een veralgemenisering van de berekening van optische stroom in drie dimensies, en laat de betrouwbaarheid zien bij bewegings-simulaties, bij simulaties met bewegend weefsel en bij de beweging in de oogkas.

*Hoofdstuk 6* beschrijft metingen met de in de voorgaande *Hoofdstukken* ontwikkelde techniek bij zes gezonde vrijwilligers. De klinische bruikbaarheid is aangetoond bij twee patiënten met een gezwel in de oogkas door de plaats van dit gezwel te bepalen, en ook bij twee patiënten na eerdere verwijdering van het oog, waarbij is aangetoond dat de oogzenuw weer vastgroeit na verwijdering van het oog. Dit laatste is bevestigd middels microscopie en pathologisch-anatomisch onderzoek. *Hoofdstuk 7* toont voor het eerst aan dat de pijn na verwijdering van een oogbol bij patiënten met een acryl-bal implantaat veroorzaakt wordt door microscopisch kleine zenuwgezwellen. Deze ontdekking is mogelijk gemaakt door de beweging bij deze patiënten te meten en te vergelijken met patiënten zonder pijn. *Hoofdstuk 8* toont voor het eerst aan dat de spierglijders in staat zijn ook zonder benige omhulling de spieren op hun plaats te houden. Daarnaast geven de bevindingen aan dat het dubbelzien na oogkasverruiming voor de ziekte van Graves veroorzaakt wordt door het oprekken van bepaalde oogspieren.



# Acknowledgment

I am deeply indebted to everyone who has assisted me with my research.

In particular, I want to thank all patients who volunteered for the MR studies and occasionally spent hours in the MR scanner, fully aware that the results might be of no benefit to them;

and furthermore, all of you who helped me come through this ordeal: Dr. Maarten Mourits, my *co-promotor* who, without any hesitation on his part, supported me from the beginning right to the end; the immense trust his patients place in him is amply illustrated by the fact that the simple mention of his name often sufficed for a reluctant patient to gladly volunteer; Professor Dr. Max Viergever, my *promotor*: I can't help wondering what kind of impression I must have made on you when, as a resident always rushing about in his white coat, I approached you with some wild ideas about motion visualization: you never failed to take my ideas seriously, for which I am grateful; Professor Dr. J.S. Stilma, my other *promotor*, for taking the gamble that I might turn out to be a good ophthalmologist after all; Dr. Tjoen An Liem, who showed me the back-alleys of the UMC when this research was performed in secret and also showed me how to drink cognac and smoke cigars like a real ophthalmologist (I hope we will soon have the opportunity to show we really are capable of singing "Strangers in the Night" in the same key); Professor Dr. Hennie Völcker-Dieben and Professor Dr. Bettine Polak, the staff, residents, nursing and administrative staff of the Department of Ophthalmology of the VUmc, who generously allowed me the incredible opportunity to finish this research on Department time, even when I had broken my leg last year and you had to cover for me; Hennie: I hope that Real Soon Now you will be able to say *chapeau!* for something I did for the VUmc (maybe a functioning website?) and Dr. Maria Suttorp, confidante, co-founder, roommate and colleague: I trust you blindly no matter whether we are giving a presentation together in front of 12 venture capitalists, or treating a patient with a mysterious uveitis; Professor Dr. W.P.T.M. Mali, who generously helped me get that vital first round of financing from his department; Dr. Ad van Gils, who never tired of working out yet another FFE protocol: you were right, AMS is more terrible than it seemed; the (former) staff, (former) residents and (former) nursing staff of the Department of Ophthalmology of the UMC; Dr.(sic) Rachel Kalmann, *pseudonimf* and soul mate in more ways than she is aware of: now it is your turn to catch up with me, in matters of מילה מילה; Dr. Ton Smit, friend and cofounder, who always made me see the bright side of writing a thesis, practicing ophthalmology, founding a company,

and life in general; Mieke de Graaf, Denise van der Linden and the other orthoptists of the UMC for organizing the Department of Ophthalmology Social Club every week; Mieke, I hope that you are pleased with the way I put some of your ideas into Chapter 8; and Denise, let's just say I miss you, here in Amsterdam; Dr. Wiros Niessen, Dr. Koen Vincken and Dr. Josien Pluim and all the others at the Image Science Institute for making me part of the team and allowing me to impersonate a *real* image scientist; Wiros, the optic (sic) flow expert and postdoc with the most attractive PhD students: I never got around to thanking you properly for the presentation you gave at that symposium I organized a year ago: good luck with the Operation Theatre of the Future project; Koen, thank you for getting the javamensch site working again, again and again: `i_still_dont_know.what_went_wrong_with_those_filenames`; Josien: thank you for cheering me up during a very difficult period last year, and for impressing upon me the importance of a careful layout of the cover; Marco Nyenhuis, Greet Bouwman and all the other NT operators of the UMC, for allowing this weird ophthalmologist into your cherished scanners, even when he arrived with steaks still dripping with blood; Wayne Rasband at the National Institutes of Health in Bethesda, MD, for making ImageJ a reality and convincing me, an old C-hack from way back from 1981 (true Kernighan-and-Ritchie C!) of the power of Java; Tony Collins of the University of Cambridge, UK, Rene Hessling of the University of Osnabrück, Chris Rorden of the University of Nottingham, Seth Robia, of the University of Wisconsin, all graduate students following course CS356 at the University of California (Davis), and all the other 3500 plus users of VolumeJ and FlowJ, for their enthusiastic support and their patience with me when old bugs that had been 'removed' unexpectedly turned up again several versions later: good luck to those of you who are still struggling with your PhD' s; Dr. Erik Korten, soon professor at the University of Eindhoven: congratulations!; everyone at Medical Art Service, Munich, Germany, especially Lara Laghetto; Dr. Joel Miller from Smith-Kettlewell Institute, San Francisco: thank you for many things, including your inspiring ideas on Chapter 8; Anet Norel, I hope you will soon get around to finish your research; Eelco Stuijtzand, because we started this together: I talked things over with Mickey in a different context; Phil Nanzetta from Signature Book Printing; Gerard de Graaf, Frank Smolders and the other photographers of the Departments of Ophthalmology of the UMC and the VUmc, for their help and for offering me their offices as a safe haven in times of need; Gerard: good luck with your research; Anja Hanson, who copy-edited this thesis in between an amazing amount of birthday parties for her daughter; and my two *paranimfen* Simone Pront and Amandus Lundqvist; Simone, thank you for always being there, my apologies for being first; Amand, I hope to have shown you that IT *may* have a future in medicine. Finally, my gratitude goes to my father and mother, without whose love I would not be.

I would like to use this opportunity to pay homage to the memory of the late Professor Dr. Leo Koornneef (1946-2001). This thesis is but a small stone on the ground-breaking foundation he laid for the study of the anatomy and function of the orbital connective tissue.

## Curriculum vitae

Michael David Abramoff was born March 7, 1963 in Rotterdam, the son of an American father (served in the US Army 101st Airborne Division during the Korean War) and a Dutch mother (schoolteacher). After finishing the *Gymnasium Erasmianum* in Rotterdam and a stellar career at McDonald's restaurants, he founded his first software company at the age of 18. He graduated from Amsterdam University (*UvA*) in Medicine in 1988 and in Biomedical Computer Science in 1989. His graduate thesis was awarded the 1989 Best Young Researcher - *Peter Reichertz Prize* - of the European Federation for Medical Informatics. After winning a two-year Japanese Science and Technology Agency fellowship, he joined the Neural Networks laboratory of the RIKEN in Tokyo, Japan, as a research fellow.

After a short stint with Sony Ltd. in Tokyo, from 1991-1993, he worked for Prodix in Paris, France, as head of the research and development department.

He returned to the Netherlands, and obtained his Medical Doctorate from the *UvA* in 1994. In 1999 he was certified for Ophthalmology by the Netherlands Specialists Registration Committee, after receiving his training at the Department of Ophthalmology of the University Medical Center (*UMC*) in Utrecht. Since then, he has been on the staff of the Department of Ophthalmology of the *Vrije Universiteit* Medical Centre in Amsterdam, and presently also holds a research position at the Image Sciences Institute of the *UMC*.

He is *mohel* for the Jewish Community of Amsterdam (Liberal), has published two plays, one of which was staged, and is holder of US patent 6,572,957. Most recently, a business plan of his won the New Venture 2001 Competition, organized by McKinsey&Company.

He is married to Dewi Moehadjir, a psychiatrist. They have two sons, Yair and Nathan.

## Publications

Peer-reviewed journal articles, book chapters and full papers in proceedings:

- ◆ M.D. Abràmoff, R. Kalmann, M.E.L. deGraaf, J.S. Stilma, M.Ph. Mourits. “Rectus extraocular muscle paths before and after decompression surgery for Graves’ orbitopathy: relationship to motility disturbances”. *Invest Ophthalm Vis Sci*. [in press].
- ◆ M.D. Abràmoff, M.A. Viergever. “Computation and visualization of three-dimensional soft tissue motion in the orbit”. *IEEE Trans Med Imag* [accepted conditionally].
- ◆ M.D. Abràmoff, L.P.M. Ramos, G.H. Jansen, and M.Ph. Mourits. “Patients with persistent pain after enucleation studied by MRI Dynamic Color Mapping and histopathology”. *Invest Ophthalm Vis Sci*. 42(9):[in press], 2001.<sup>1</sup>
- ◆ M.D. Abràmoff, W.J. Niessen, and M.A. Viergever. “Objective quantification of the motion of soft tissues: an application to orbital soft tissue motion”. *IEEE Trans Med Imag*. 19 (10):986-995, 2000.<sup>1</sup>
- ◆ M.D. Abràmoff, A.D. Van Gils, G.H. Jansen, and M.Ph. Mourits. “MRI dynamic color mapping: a new quantitative technique for imaging soft tissue motion in the orbit”. *Invest Ophthalm Vis Sci*. 41:3256-3260, 2000.<sup>1</sup>
- ◆ E.P. Stuijzand, M.D. Abràmoff, K.J. Zuiderveld, L.M.P. Ramos, J. Weickert, M.Ph. Mourits, F.W. Zonneveld, and W.P.T.M. Mali. “Fast cinematic magnetic resonance imaging of the eye and orbit”. *Electr J Radiol Soc N Amer*. 1, 1997. Available at [http://ej.rsna.org/EJ\\_0\\_96/0032-97.fin/ej0032-97.html](http://ej.rsna.org/EJ_0_96/0032-97.fin/ej0032-97.html)
- ◆ M.D. Braamhof<sup>2</sup>. “Spatiotemporally correlating neurons”. *IEICE [Japan] Neurocomputing issue*. 90 (95):161-164, 1991.
- ◆ R. Kalmann, M.E.L. deGraaf, M.D. Abràmoff, J.S. Stilma, T. Berendschot, M.Ph. Mourits. “What causes diplopia after translid and coronal orbital decompression for Graves’ orbitopathy?”. *Submitted*.

---

<sup>1</sup> Reprinted with permission

<sup>2</sup> My surname was Braamhof between 1980 - 1990.

## Book chapters

- ◆ M.D. Abràmoff. Functional anatomy of the orbit: imaging aspects. In: *Course book, "7th Rotterdam international skull base day"*, edited by I.M.J. Mathijssen, Rotterdam, Netherlands: Skull Base Society, 1999, p. 35-47.
- ◆ M.D. Abràmoff and J. Korf. "Beeldverwerkende technieken bij schizofrenie en de pathogenese van de psychose". In: *Leerboek schizofrenie*, edited by J. A. Den Boer and R. J. Van Den Bosch, Utrecht: Tijdstroom, 1996, p. 174-197.
- ◆ M.D. Braamhof. "Spatiotemporal correlation in the cerebellum". In: *Artificial neural networks*, edited by T. Kohonen, K. Makisara, O. Simula, and J. Kangas, Amsterdam:Elsevier Science Publishers, 1991, p. 1739-1742.
- ◆ M.D. Braamhof, A.T.C. Coolen, G. Wieneke, and P. Janssen. "Can neural networks explain dysfluent speech?". In: *Speech motor control and stuttering. Proceedings of the 2nd international conference on speech motor control and stuttering.*, edited by H. F. M Peters, W. Hulstijn, and C. D. Starkweather, Amsterdam: Elsevier Science Publishers - Excerpta Medica, 1991, p. 181-188.
- ◆ M.D. Braamhof. "Stotterende neurale netwerken: bestaan zij?". In: *Readings in Medical Informatics*, edited by G.J.E. DeMoor, Gent-Belgium: VMBI-MIM, 1989, p. 349-358.
- ◆ M.D. Braamhof and J. Donnison-Speyer. "High resolution image processing in Medical Image Student System (MISS)", in: *Technology and Education*, edited by G. McKye and D. Treeman, New York, NY: Wiley, 1989.

## Full papers in proceedings

- ◆ M.D. Braamhof. "Spatiotemporal correlation and the cerebellum". Seattle, WA: Proceedings of the IEEE - INNS International joint conference on neural networks. II:609-612, 1991.

PRODUCTION NOTES

*Typeset by the author in the Times Roman, Arial and Web Hebrew AD fonts.  
Images formatted in CMYK using Adobe Photoshop 5.1 and Adobe Acrobat 4.0.  
Layout by the author using Microsoft Word 2000.  
Output in Portable Document Format (PDF) and transfer to plate for 4-color printing.  
Printed on 70lb matte coated white paper by Signature Book Printing: [www.signature-book.com](http://www.signature-book.com).*